Subcycle terahertz nanoscopy of ultrafast interlayer dynamics in van der Waals heterostructures

Tunneling is one of the most fundamental manifestations of quantum mechanics determining elementary physical processes, chemical reaction pathways and shaping life as we know it. Moreover, it is crucial for modern data storage and electronics, and is essential for highly efficient solar technology.

In this work, we introduce a novel, non-invasive concept to resolve electron tunneling on the relevant length- and timescales that even works on insulating samples. The central idea is to monitor the evolution of the local polarizability of electron-hole pairs during the tunneling process with evanescent terahertz nearfields, which are detected with subcycle temporal resolution.

In a proof of concept, we resolve the ultrafast interlayer dynamics in van der Waals heterobilayers utilizing our new technique of subcycle contact-free nanoscopy to access the full life cycle of photo-induced spatially separated interlayer electron-hole pairs. Our approach builds on the drastic change of the polarizability of the electron-hole pairs during interlayer tunneling as explained by ab initio density functional theory calculations. We confirm the temporal dynamics using a complementary terahertz emission experiment that is directly linked to the ultrafast charge separation. Moreover, we reveal pronounced variations of the local formation and annihilation of interlayer excitons on deeply subwavelength, nanometer lengthscales. Such contact-free nanoscopy of tunneling-induced dynamics should be universally applicable to conducting and non-conducting samples and reveal how ultrafast transport processes shape functionalities in a wide range of condensed matter systems.
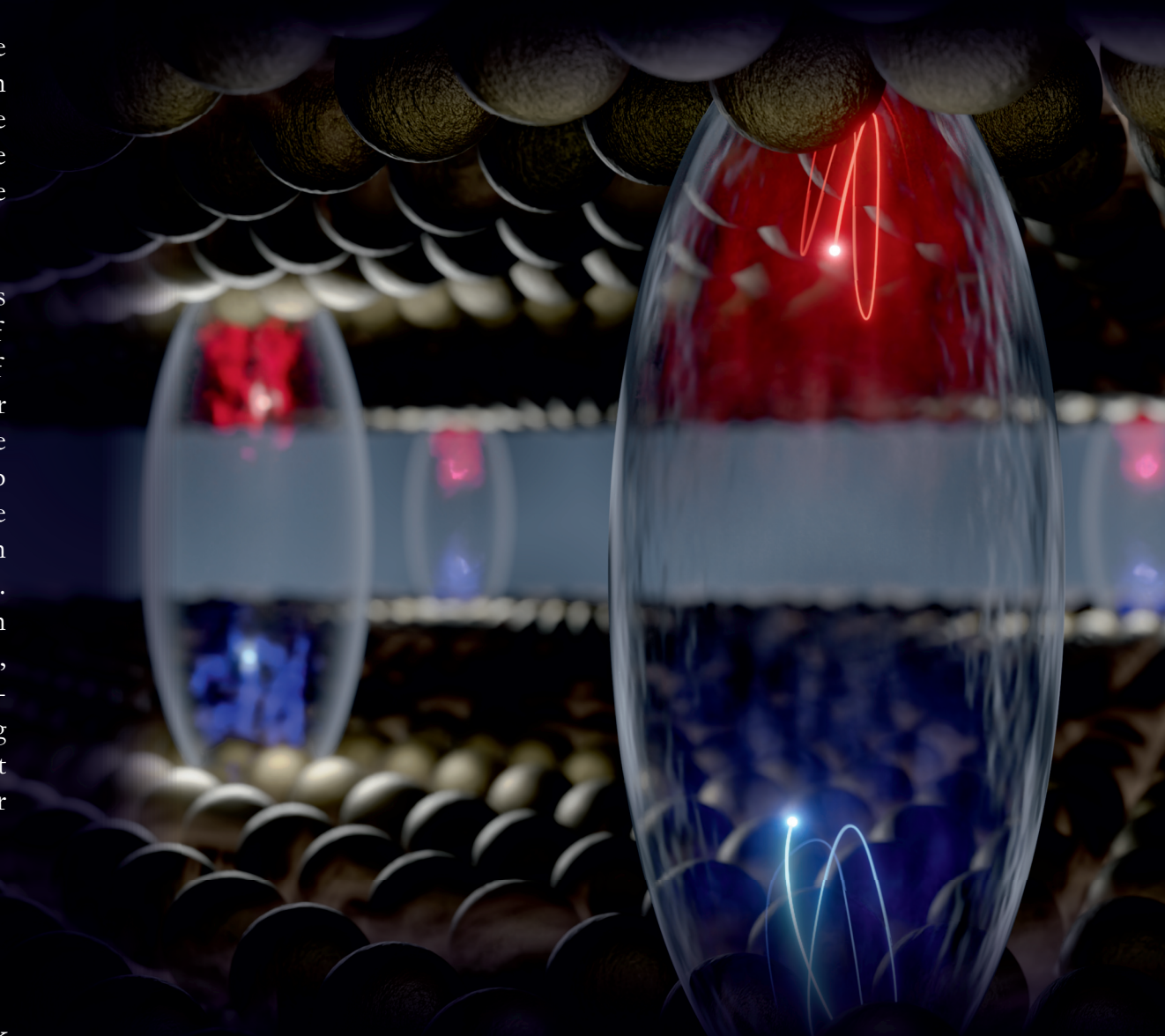
Universität Regensburg
Institut für Experimentelle und Angewandte Physik
Lehrstuhl Prof. Dr. Rupert Huber

Markus Plankl

Subcycle terahertz nanoscopy
of ultrafast interlayer dynamics
in van der Waals heterostructures

Das Promotionsgesuch wurde eingereicht am: 18.01.2021.

Die Arbeit wurde angeleitet von: Prof. Dr. Rupert Huber.

Datum des Promotionskolloquiums: 16.09.2021

Prüfungsausschuss: Vorsitzender: Prof. Dr. Jaroslav Fabian
                   1. Gutachter: Prof. Dr. Rupert Huber
                   2. Gutachter: Prof. Dr. Jörg Wunderlich
                   weiterer Prüfer: Prof. Dr. Christian Schüller

Contents

Chapter 1

Introduction

The quantum nature of the world around us manifests in many nonclassical and
therefore unintuitive phenomena including particle wave dualism, quantum entan-
glement or the uncertainty principle. The implications of quantum mechanics chal-
lenged some of the most famous physicists of all time [Bac09] and have been found
to be crucial for fundamental properties and processes in nature [Gri18], biological
mechanisms [Sch92, Abb08] and countless prospects of modern technology [Ngô14].
In particular, tunneling is one of the most fundamental manifestations of quan-
tum mechanics and is a central process determining chemical reaction pathways
[Bel80, Ley12, Sch17] and shaping life as we know it [Bro17, Mar18]. First pro-
posed in the 1920s describing the ground state of molecules [Hun27] and the ra-
dioactive α-decay [Gam28], the fundamental process of tunneling is still investi-
gated [Ram20, Jia21], is utilized in modern data storage [Kah67] and electronics
[Esa73, Sea13], and is essential for highly efficient solar technology [Phi14]. Us-

ing tunneling as the probing mechanism in scanning tunneling microscopy achieved surface imaging with atomic resolution [Bin82, Bin83] and just recently, light-wave driven scanning tunneling microscopy revolutionized ultrafast nanoscience by accessing the motion of a single molecule in space and time [Coc16, Pel20]. Therefore, as an omnipresent process ranging from fundamental atomic dynamics to complex biological systems as well as the use in modern applications and measurement techniques, tunneling has to be well understood to reveal the biological mechanisms in nature, refine current technology and harvest its full potential in future applications.

In the last decades, two-dimensional van der Waals materials have become one of the most intriguing topics in condensed matter physics featuring extraordinary physical properties due to quantum confinement and provide an exciting playground to explore exotic quantum phenomena [Li21, Zhe21, Ken21]. After single layers of graphite, called graphene, were first fabricated [Nov04], the field of two-dimensional crystals was born and now includes insulating, semiconducting, conducting and even superconducting material sheets [Nov16, Uge16]. Thereby, a whole class of semiconducting materials, transition metal dichalcogenides (TMDCs), were rediscovered featuring dramatically different material properties in their two-dimensional limit. Remarkably, in contrast to graphene, TMDC monolayers exhibit a finite and direct bandgap foreshadowing their potential for modern semiconductor technology [Ahm17]. In addition, due to the confinement into two dimensions and reduced screening, they exhibit uniquely strong Coulomb correlations between electrons and holes binding into a hydrogen-like state, called exciton, which forms on ultrafast timescales after photoexcitation [Poe15] and is even stable at room temperature [Che14b]. In combination with their strong interaction with light despite their atomic-scale thickness [Wur17] this makes them a promising candidate for future applications at the interface between electronic and optical signals. Moreover, the strong spin-orbit coupling in these material sheets leads to spin dependent splitting of valence and conduction band. Thereby, it allows for fully spin-polarized bands in the monolayer limit supporting the promising next generation of integrated circuitry and memory technology by utilizing spintronics [Žut04, Gmi15, Jun16, Wun17, Hir20] and paving the way for the novel field of valleytronics [Ple16, Sch16a, Ple17, Mak18].

The already rich physics of two-dimensional materials and the potential for future applications is only the tip of the iceberg, since the van der Waals nature can not only be used to isolate single atomically thin sheets, but also to stack them in ways nature never intended to. Due to their van der Waals bond, conventional processing limitations, like crystal lattice matching, do not apply [Liu19] allowing for countless novel artificial material combinations, so called heterostructures, with unique physical properties. Despite being only van der Waals bound, the interlayer interaction shapes the physical properties of the heterostructure depending on the monolayer material [Nov16] and the relative angle of the stacked sheets [Zol19a, Mer19, Mer20]. New exotic phenomena emerge, such as superconductivity and highly correlated states in magic-angle graphene [Cao18a, Cao18b, Che19a] and Mott transitions in TMDC bilayers [Reg20, Tan20].

One of the fascinating interactions between the sheets is ultrafast interlayer tunneling, where electrons and holes overcome the van der Waals gap. Thereby, leading to charge separation on atomic lengthscales, a prerequisite for nanoscale magnetoresistive devices [Kle18, Son18] as well as atomically thin optoelectronic signal processing [Che14a, Lee14, Mas16, Lor20] and solar technology [Fur14]. Moreover, ultrafast interlayer tunneling is at the heart of interlayer exciton formation [Hon14, Pen16, Nag17, Ma19, Mer19, Zim21], which are bound electron-hole pairs that are spatially separated and reside in adjacent monolayers. In contrast to their intralayer counterpart, where electron and hole are located in the same layer, interlayer excitons feature at least one order of magnitude longer lifetimes [Riv15, Wan21] providing a framework for future high-temperature Bose-Einstein condensation phenomena [Su08, Fog14] and complex optoelectronic computing units [Ma16, Unu18, Jau19]. Understanding this interlayer interaction on the relevant length- and timescales is crucial to design novel atomic-scale devices to optimize current processing circuitry and take the step towards light-driven electronics as well as tackle the energy challenge generating clean energy with new solar technologies.

A valuable tool to investigate the fundamental electronic properties and dynamics of such materials, especially focusing on the behavior of excitons, is time-resolved optical spectroscopy. In particular, the terahertz (THz = 10^{12} Hz, $0.1 - 10$ THz or 3 mm $- 30$ µm) and mid-infrared ($10 - 100$ THz or $30 - 3$ µm) spectral ranges include

internal excitonic transitions and span fascinating low-energy excitations including crystal lattice vibrations (phonons) [Gun00], collective oscillations of charge carriers (plasmons) [Hub01] or spin-waves (magnons) describing the collective motion of magnetic moments [Pas13, Qin15, Bai16, Sch19]. In particular, using field-resolved detection to record the electromagnetic waveform in the time domain allows for direct access to the full complex dielectric function of the sample system. In combination with ultrafast photoexcitation, the ultrafast formation and recombination of intralayer excitons in TMDC monolayers have been observed [Poe15, Ste17b, Ste18] and the ultrafast phase transition from intralayer to interlayer excitons in TMDC heterostructures mediated by interlayer tunneling has been resolved [Mer19]. However, accessing low-energy excitations on their respective energy scale leads to large probing wavelengths, which are fundamentally limited by diffraction [Abb73] and unable to spatially resolve local differences in modern nanoscale electronic and optoelectronic devices.

Near-field microscopy has become a well-established technique to overcome the diffraction limit and achieve nanoscale spatial resolution independently of the probing wavelength [Poh84, Dür86, Bet86, Kno99, Kno00, Hil00]. Here, the probe light is focused onto a sharp metallic tip and the evanescent electric field is used to probe the local properties of the sample system with spatial resolution largely determined by the radius of curvature at the apex. Near-field microscopy provides a versatile platform for spectroscopy spanning from visible to microwave radiation [Che19b]. In particular, it has been used to resolve phase transitions [Qaz07, Liu13b, Hub16, McL17, Pos18] and magnetic domain switching [Pfi18, Jan20], and can even access ultrafast dynamics [Wag14, Eis14, Hub17]. In two-dimensional materials, it has been employed to resolve the linear and nonlinear optical response of van der Waals systems [Bao15, Par18, Zha18a] and visualize moiré superlattices [Sun18, Jia19, Sun20]. Nevertheless, spatiotemporal access to the interlayer dynamics of van der Waals heterostructures has been elusive.

While light-wave driven scanning tunneling microscopy provides suitable temporal and spatial resolution to investigate such van der Waals devices, the technique requires electrically conducting samples and the external electric current in the scanning tunneling microscope junction may perturb intrinsic tunneling processes of the

heterostructure. In this work, we introduce a complementary, non-invasive concept to resolve electron tunneling on the relevant length- and timescales that even works on insulators. The central idea is to monitor the evolution of the local polarizability of electron-hole pairs during the interlayer tunneling with evanescent terahertz near-fields, which we detect with subcycle temporal resolution [Pla21]. Such contact-free nanoscopy of tunneling-induced dynamics should be universally applicable to conducting and non-conducting samples and reveal how ultrafast transport processes shape functionalities in a wide range of condensed matter systems.

Therefore, we pioneer a novel combination of ultrafast nanoscopy with a high-power, ultrastable thin-disk oscillator operating at high repetition rates to implement a new THz nanoscopy experiment with subcycle temporal resolution. The new experiment is capable of accessing the local optical conductivity, resolving the THz emission signatures and monitoring the ultrafast evolution of the local polarizability after photoexcitation using visible pump/terahertz probe time-domain spectroscopy. In a proof of concept, we resolve the ultrafast interlayer dynamics in van der Waals heterobilayers utilizing the new concept of subcycle contact-free nanoscopy to access the full life cycle of photo-induced spatially separated interlayer electron-hole pairs. Our approach builds on the drastic change of the polarizability of the electron-hole pairs during interlayer tunneling as explained by *ab initio* density functional theory calculations performed by Dr. Paulo Faria Junior, Dr. Martin Gmitra and Prof. Dr. Jaroslav Fabian. We confirm the temporal dynamics using a terahertz emission experiment that is directly linked to the ultrafast charge separation. Moreover, we reveal pronounced variations of the local formation and annihilation of interlayer excitons on deeply subwavelength, nanometer lengthscales.

In the last part of this thesis, we explore new high-power mid-infrared sources with dramatically increased average-power to extend the spectral range of future nanoscopy studies, where we can resonantly probe phonons and plasmons and access internal excitonic transitions. Furthermore, the substantially increased signal-to-noise ratio should allow for practical field-resolved ultrafast mid-infrared nanoscopy with simultaneous temporal resolution of 10 fs and spatial resolution of 10 nm, while driving nonlinear phenomena. Therefore, we collaborate with Prof. Dr. Oleg Pronin from the Helmut-Schmidt-Universität in Hamburg and Dr. Francesco Tani from the

Max Planck Institute for the Science of Light in Erlangen to implement state-of-the-art high-average power broadening schemes for mid-infrared generation, resulting in ultrashort few-cycle mid-infrared waveforms with peak fields that should even reach into the strong-field limit.

This work is structured as follows: **Chapter 2** focuses on the extraordinary electronic and optical properties of TMDC materials in their monolayer limit and the great potential and versatility of van der Waals heterostructures. In **Chapter 3**, the basic concept and theoretical modeling of near-field microscopy is introduced followed by an overview of the new nanoscopy experiment including the high-power thin-disk laser system, THz generation and field-resolved detection. The fabrication of TMDC heterostructures and their pre-characterization as well as the THz emission experiment is discussed in **Chapter 4**. Using THz emission nanoscopy, we identify ultrafast interlayer tunneling in our sample system and by numerically modeling the tip-sample interaction, we retrieve the ultrafast interlayer current. In **Chapter 5**, we focus on the new concept of subcycle contact-free nanoscopy to access the interlayer dynamics, in particular the formation of spatially separated electron-hole pairs mediated by interlayer tunneling and their long lived recombination dynamics. We discuss the substantial change in electron-hole pair polarizability using density functional theory and confirm the new technique using THz emission nanoscopy, which is directly linked to the interlayer tunneling current. Investigating a representative region of the heterostructure with this new near-field concept reveals substantial differences in formation and recombination dynamics on the nanoscale. Additionally, we show first results of modified recombination dynamics depending on the photo-induced carrier density, possibly modifying the band alignment of the heterostructure. Looking towards prospective experiments, we present exploratory steps towards high-power sources for ultrafast field-resolved mid-infrared nanoscopy even reaching the strong-field limit in **Chapter 6**. Finally, the experimental findings are concluded and an outlook towards future experiments is given in **Chapter 7**.

Chapter 2

Transition metal dichalcogenides as versatile platform for future atomically thin applications

With the discovery of graphene [Nov04] and its fascinating mechanical, optical and electronic properties when reducing graphite to an atomically thin sheet, scientists started searching for other materials featuring a similar transformation – the field of two-dimensional materials was born.

Naturally, graphene is the first and most known member of the family of two-dimensional crystals, so called van der Waals materials, but many others followed soon including insulators (e. g. hBN), semiconductors (e. g. $MoSe_2$) or metals (e. g. $NbSe_2$) [Nov16], that can even exhibit superconducting behavior [Uge16, Wan17]. The class of transition metal dichalcogenides (TMDCs) was found to host many van der Waals materials that were already long and well known in their bulk form [Dic23, Wil69]. Like in graphene, their physical properties exhibit a drastic change when reduced to their monolayer limit with a thickness of only a few atoms. In particular, semiconducting TMDCs feature an indirect bandgap that transforms into a direct one in the monolayer case [Leb09], providing a versatile platform for future nanoscale optoelectronic applications [Tha20]. Moreover, these materials feature strongly bound excitons with up to hundreds of meV in binding energy dominating their optical properties even at room temperature [Che14b].

Furthermore, the layered nature of van der Waals materials allows not only to reduce them to an atomically thin monolayer, but provides the means for engineering novel artificial materials with no practical constraints like crystal lattice matching or processing compatibilities [Liu19]. The variety of TMDC materials in combination with other van der Waals systems allows for virtually endless combinations only bound by van der Waals forces, so called heterostructures, which still feature interlayer interaction and exhibit fascinating behavior ranging from correlated phenomena [Cao18a, Reg20, Tan20] and superconducting phases [Cao18b, Che19a, Lu19a] to promising atomically thin magnetic [Son18, Kle18], electronic [Yu13, Wan19] and optoelectronic [Fur14, Che14a, Lee14, Mas16, Lor20] devices.

In the following, an overview of the many fascinating properties of TMDC materials is given, covering the most relevant characteristics for this work, including the crystal structure, electronic and optical properties, and their unique, strongly bound excitons. Furthermore, the concept of combining van der Waals materials to two-dimensional heterostructures is introduced.

2.1. Crystal structure

Generally, TMDCs form in the chemical structure of MX_2, whereby M is a transition metal from subgroup IV, V or VI of the periodic table, for example molybdenum (Mo), tungsten (W) or niobium (Nb), and X is a chalcogen, for instance sulfur (S), selenium (Se) and tellurium (Te). TMDCs in their bulk form like molybdenum disulfide (MoS_2) were already studied as early as 1923 [Dic23] and include insulators, semiconductors, semimetals and metals [Wil69]. Since the crystallographic properties vary for the different subgroups, we focus on the semiconducting materials that are investigated in this work, namely molybdenum diselenide ($MoSe_2$), tungsten diselenide (WSe_2) and tungsten disulfide (WS_2). They are all layered undistorted semiconductors that feature a trigonal prismatic crystal structure. The transition metal in the center is surrounded by six covalently bound chalcogen atoms at each corner (Figure 2.1a). The length and angles of the covalent bonds vary depending on the exact material combination. As an example, in MoS_2 the distance between the chalcogen atoms is $d_1 = 3.16\,\text{Å}$. A spacing of $d_2 = 2.41\,\text{Å}$ is found between the
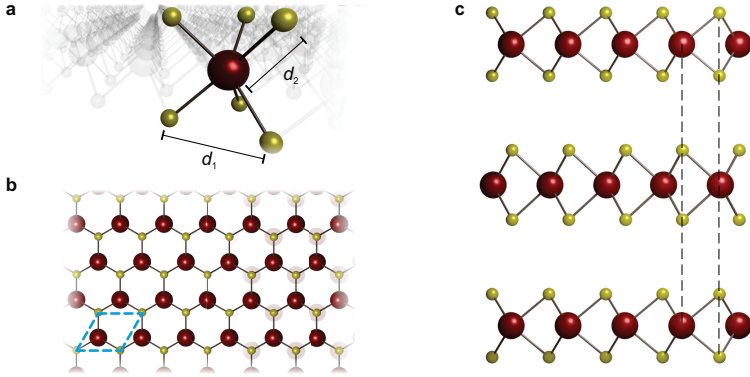
Figure 2.1 | Crystal structure of layered transition metal dichalcogenides (TMDCs). a, Trigonal prismatic shape of the crystal structure depicting the transition metal in red and the chalcogen atoms in yellow. **b,** Top view of **a** displaying the hexagonal structure of one layer. The unit cell (blue dashed frame) consists of one prismatic cell with a transition metal (red) and one without. On the right part of the image, the transition metals of the next layer are indicated by the faint red circles below the chalcogen atoms. **c,** Side view of **a** showing the most common 2H stacking order for layered TMDCs. Adjacent layers are rotated by 60° and the chalcogen atoms are located directly on top of the transition metals and vice versa.

sulfur atoms and the center molybdenum resulting in a layer thickness of about 6.1 Å [Wil69]. Each layer forms a hexagonal lattice structure (Figure 2.1b), similar to the honeycomb structure of graphene. The unit cell is marked with the blue dashed frame consisting of one prismatic cell with a centered transition metal (red) and one prismatic cell without one. In the bulk crystal, these layers are stacked on top of one another. The natural stacking for the materials used in this thesis shows the most common 2H stacking, where every other layer is rotated by 60° and the chalcogen atoms are located on top of the transition metal atoms of the next layer (vertical dashed lines, Figure 2.1c). The individual layers are bound by the weak van der Waals force, which allows for mechanical exfoliation, where the crystal is reduced to only one single layer. Due to the broken inversion symmetry for one monolayer, these exhibit nonlinear phenomena, e. g. allowing for second harmonic generation to

determine the orientation of the crystal axis [Kun18]. Moreover, reducing TMDCs to only one layer leads to critical changes in their electronic and optical properties.

2.2. Band structure and electronic properties

Since the optical properties of semiconductors are strongly tied to the energetic configuration in momentum space, understanding the electronic band structure of the material system is crucial. In particular, the transition from an indirect to a direct bandgap in TMDC monolayers generated a strong scientific interest in the last decade [Wan18].

The Brillouin zones of the TMDCs investigated in this work feature a hexagonal shape due to the crystal structure, whereby the Γ point in the center and K point on the edge are the most important positions (Figure 2.2a, top). The band structure between Γ, M and K (orange line) is shown in Figure 2.2b for different crystal thicknesses of WSe_2. As early as 1972, first calculations were performed for the bulk crystals, finding the valence band maximum at the Γ point and the conduction band minimum between Γ and K, classifying the materials as indirect semiconductors [Bro72, Mat73]. Only after atomically thin carbon films, i.e. graphene, with their unprecedented physical properties were experimentally accessible [Nov04], TMDCs were investigated for a similar behavior. First band structure calculations for multilayer and monolayer TMDCs were performed [Leb09], showing a transition of the indirect bandgap to a direct one in the monolayer limit (purple arrows in Figure 2.2b). These findings were quickly confirmed theoretically [Kuc11, Kum12] and experimentally [Mak10, Spl10, Zha13] reporting a drastic increase in photoluminescence for the monolayer identifying the direct bandgap, which makes them the ideal building block for future atomically thin optoelectronic technology [Tha20].

Qualitatively, this transition towards a direct bandgap is caused by the reduced overlap of electronic orbitals in the monolayer case. For example in MoS_2, the band states at the K point are mostly composed of strongly localized d-orbitals at the molybdenum atoms. These have minimal interlayer coupling since they are located in the center of the unit cell. In contrast, at the Γ point the d-orbitals of molybdenum and the p_z-orbitals of the sulfur atoms are mostly contributing to the
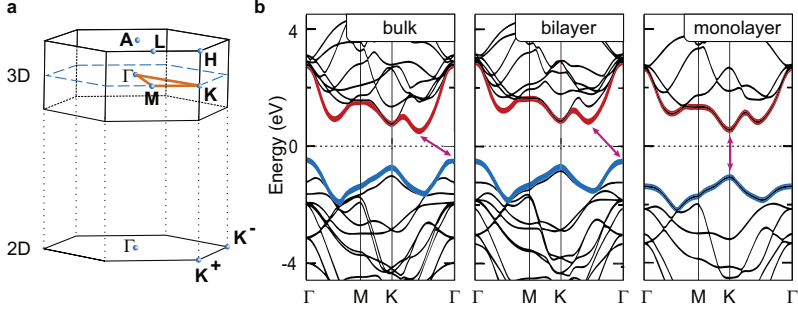
Figure 2.2 | Brillouin zone and band structure of WSe₂. a, Hexagonal Brillouin zone of the bulk crystal featuring the most important symmetry points (top). The Brillouin zone in the two-dimensional limit exhibits the inequivalent K^+ and K^- points (bottom). **b,** Band structures of WSe₂ bulk, bilayer and monolayer are shown. The conduction (red) and valence band (blue) change for decreasing crystal thicknesses until the direct bandgap emerges (purple arrows). The band structures are reproduced from [Kum12].

band energy. The p_z-orbitals are highly sensitive to their surrounding and hence also to adjacent layers. When the crystal thickness is reduced, the indirect bandgap energy increases more strongly than the gap at the K point, leading to the formation of a direct bandgap [Spl10, Kuc11].

Furthermore, TMDCs feature strong spin-orbit interaction due to their heavy elements, causing spin splitting of conduction and valence band. Due to the additionally broken inversion symmetry in the monolayer (Figure 2.2a, bottom), new optical selection rules arise between completely spin polarized bands at K^+ and K^- [Xia12, Xu14] and pave the way for new fields such as spintronics [Žut04, Gmi15, Jun16, Wun17, Hir20] and valleytronics [Ple16, Sch16a, Ple17, Lan18, Mak18].

11

2.3. Excitons in two dimensions

Besides the emerging direct bandgap in the monolayer, the confinement into two dimensions has a profound influence on the behavior of photo-induced electron-hole pairs. For typical semiconductors, we only expect absorption for radiation with photon energies larger then the bandgap energy E_{gap}. Only then, electrons can be excited from the valence to the conduction band. Experimentally, however, absorption is even observed for photon energies smaller than the bandgap. This is caused by excitons: bound states of the photoexcited electrons in the conduction band and the remaining holes in the valence band due to Coulomb correlations. Since a positive charge is attributed to the hole, electron and hole are attracting each other and form a bond (Figure 2.3a). The binding energy of the exciton thereby reduces the bandgap for absorption of the semiconductor to $E_{\mathrm{gap}} - E_{\mathrm{ex}}$ (Figure 2.3b, c, top) [Hun09, Rud18].

Generally, there are two limiting cases to describe excitons: strongly bound Frenkel excitons [Fre31] and weakly bound Wannier-Mott excitons [Wan37]. Strongly bound Frenkel excitons mostly occur in molecules and ion crystals with binding energies up to 1 eV and small electron-hole separation on the order of the lattice constant. Generally, the electron-hole pair is located on the same lattice site and can move through the crystal by tunneling to neighboring lattice atoms. Wannier-Mott excitons are typically found in inorganic semiconductors and exhibit an electron-hole distance of multiple lattice constants in their ground state and typical binding energies below 10 meV, due to the strong dielectric screening. They are not bound to the lattice sites, allowing for quasi-free movement in the crystal and their energy levels can be described with a modified hydrogen model [Hun09, Rud18].

Thus, Wannier-Mott excitons are found in conventional semiconductors, but are mostly neglected at room temperature since they are not stable or observable due to their low binding energy, for example in GaAs ~ 4 meV [Nam76]. In contrast, TMDC monolayers exhibit exceptionally high binding energies which reach hundreds of meV [Che12, MS13, Qiu13, Che14b, Ye14, He14, Uge14, Poe15, Sti16, Tru16], caused by the unique properties of the two-dimensional material sheet and dominating the electronic and optical properties even at room temperature, which will be explained
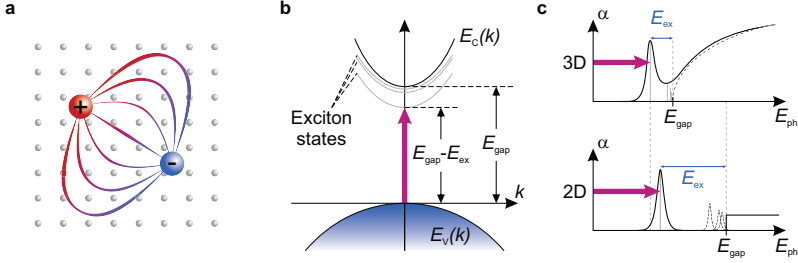
Figure 2.3 | Electronic and optical properties of excitons. a, Schematic representation of a bound electron-hole pair, so called exciton, within a crystal lattice. In this case, a Wannier-Mott-type exciton is depicted displaying electron-hole separation of multiple unit cells. **b,** Simplified band structure of a direct semiconductor with bandgap energy E_{gap} between the valence band ($E_V(k)$) maximum and the conduction band ($E_C(k)$) minimum. The bound state of the electron-hole pair reduces the optical bandgap energy (purple arrow), leads to the emergence of exciton states below the conduction band (gray lines) and modifies the optical bandgap $E_{gap} - E_{ex}$. **c,** Simplified absorption spectra of a semiconductor in three dimensions (top), showing a peak in the absorption α at the optical bandgap energy (purple arrow) and hydrogen-like exciton states with energies below the bandgap (gray lines). For energies higher than E_{gap}, the dispersion relation of the material sets in (dashed line). In the two-dimensional limit (bottom) the bandgap and binding energy are increased. The dashed lines indicate higher hydrogen-like exciton states clearly separated from the free-particle bandgap [Che14b, Wan18].

in detail in the next paragraph. The experimental techniques used to determine the binding energies include, among others, linear reflectance [Che14b] and magneto reflectance measurements [Sti16]. Direct access to the energy states is achieved by probing the $1s$-$2p$-transition of the exciton [Poe15]. These findings were also confirmed by various theoretical calculations [Che12, MS13, Qiu13, Tru16].

When the TMDC crystal is reduced to the monolayer, there are three main contributions, increasing the binding energy drastically. By confining the exciton into a two-dimensional plane, the binding energy is increased up to a factor of 4 (Figure 2.3c, bottom) [Kli07, Che14b]. In addition, the effective masses of electron and hole at the K-point are quite large ($\sim 0.5\,m_0$) and directly contribute to the binding energy [Liu13a, Kor14, Wan18]. At last, the strongly reduced screening
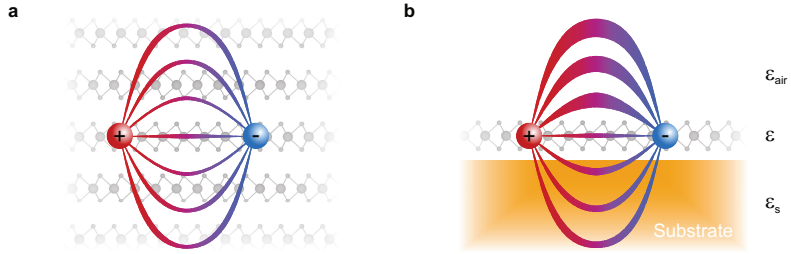
Figure 2.4 | Exciton screening effects in three and two dimensions. a, Excitons in a bulk TMDC. The dielectric environment screens the Coulomb interaction. **b,** TMDC monolayer on a substrate. While the monolayer (ϵ) and substrate (ϵ_s) significantly screen the Coulomb interaction, vacuum or air (ϵ_air) have almost no effect on the interaction between electron and hole, leading to the strong increase in exciton binding energies for TMDC monolayers which is indicated by the field lines with increased thickness.

of the Coulomb interaction between electron and hole increases the binding energy additionally. Since the monolayer is freestanding or deposited on a substrate, strong screening effects like in the bulk crystal are avoided (Figure 2.4a). The high dielectric permittivity of TMDCs ($\epsilon \sim 10$) only acts within the atomically thin monolayer, while most field lines experience substrate, air or vacuum, which have significantly smaller dielectric constants and lead to a strongly reduced screening of the Coulomb interaction in comparison to the bulk TMDC (Figure 2.4b). Despite the high binding energy, the exciton wavefunctions were found to extend over several lattice constants [Sti16, Sti18a], the effective mass approximation is applicable and a hydrogen-like behavior is observed. Therefore, the excitons in TMDC monolayers can be adequately described by the Wannier-Mott picture [Wan18].

In summary, similar to graphene, as an atomically thin metal, TMDC monolayers can be used as a complementary two-dimensional semiconductor in the future. Their strong interaction with light, particularly absorption [Li14, LS13] and emission [Spl10, Mak10] as well as their large exciton binding energy and ultrafast dynamics [Poe15, Moo16, Ste17b, Ste18, Mer19] make them promising ingredients for future information technology. Moreover, in contrast to graphene, these semiconducting monolayers exhibit a finite, direct bandgap making them ideally suited for prospective electronic and optoelectronic applications [Fio14, Jar14, Xia14].

2.4. Van der Waals heterostructures

In addition to the already rich physics of these two-dimensional sheets, the nature of van der Waals bound, layered crystals allows one to engineer novel artificial materials. In contrast to conventional semiconductors, van der Waals heterostructures can be fabricated irrespective of limited lattice matching and processing compatibilities [Liu19]. Building blocks range from insulating hexagonal boron nitride (hBN) over semiconducting materials, like phosphorene and TMDC monolayers, all the way to fully metallic graphene (Figure 2.5a) that can be combined to achieve the desired material properties [Nov16, Lia19]. The newest additions include superconducting $NbSe_2$ [Uge16, Wan17] and two-dimensional ferromagnets [Hua17, Gon17]. Complex nanoscale devices can be constructed and due to angle dependent interaction of the constituent layers (Figure 2.5b), an additional degree of freedom emerges that allows for tailoring the resulting physical properties [Ni15, Cao18a, Cao18b, Lu19a, Lia19, Che19a, Reg20, Tan20, Mer20].

In the last decade, scientist and engineers around the globe explored the vast amount of possibilities and already achieved promising and wide-ranging breakthroughs from fundamental science to modern applications. Structures made of graphene, with fine control of the stacking angle show Mott insulating [Cao18a] and superconducting [Cao18b, Che19a] behavior in so called magic-angle graphene bilayers and trilayers depending on the carrier density [Lu19a], while the twist angle in TMDCs provides a tuning knob for the internal Coulomb correlations [Mer20]. Moiré superlattices have been visualized [Ni15] and used to access correlated phenomena like Mott insulating states [Reg20, Tan20]. Significant magnetic and spin-filtering effects were found, allowing for future atomically thin magnetic information storage and spintronic devices [Son18, Kle18]. Additionally, field-effect transistors consisting of only a few atomic layers were designed, tackling the modern challenge of producing electronics with higher and higher densities of logical elements to achieve more powerful future computing devices [Yu13, Wan19]. Few-layer monochromatic emitters [Lor20] and ultrafast photodetectors [Mas16] lay the foundations for nanoscale interfaces to connect electronic and optical signal processing in prospective optoelectronic applications. Furthermore, the global energy challenge of generating more renewable energy can be met with atomically thin solar cells [Fur14] and p-n-junctions [Che14a, Lee14], proposing a new and versatile material for future solar technology.

15
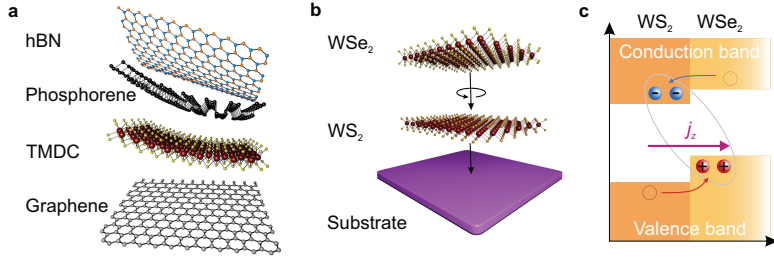
Figure 2.5 | Van der Waals heterostructures. a, Overview of the crystal structure of several van der Waals materials from different material classes, that can be used to produce heterostructures. **b,** TMDC heterobilayer showing the additional degree of freedom by rotating one of the layers during the fabrication process. **c,** Type-II band alignment for a WSe_2/WS_2 heterostructure. Due to the staggered band alignment, electrons move into the WS_2 and holes transfer in the WSe_2 layer, but still interact to form interlayer excitons (gray ellipse).

Most of the phenomena found and applications developed are based on the interlayer interaction between the constituents of the heterostructures. Specifically, interlayer carrier tunneling [Hon14, Pen16, Ma19] is crucial for light harvesting and emitting devices and is at the heart of interlayer exciton formation [Riv15, Ceb14, Nag17, Mer19, Wan21, Zim21]. In contrast to the excitons discussed before (see Section 2.3.), where the bound electron-hole pair is located in the same layer resulting in so called intralayer excitons, interlayer excitons consist of spatially separated electrons and holes, that reside in adjacent van der Waals layers leading to profoundly different behavior.

In TMDC heterostructures with type-II band alignment, for example WSe_2/WS_2, photogenerated electrons and holes form intralayer excitons, but will quickly separate into the energetically more favorable layers. The staggered band alignment of valence and conduction band (Figure 2.5c) leads to interlayer tunneling of the photoinduced charge carriers (arrows) into the adjacent layer. However, these spatially separated electron-hole pairs still interact and form interlayer excitons. This phase transition from intralayer to interlayer electron-hole pairs happens on the order of hundreds of femtoseconds [Hon14, Mer19, Ma19, Wan21]. Due to the spatial sepa-

ration, their wavefunction overlap is strongly reduced leading to extended lifetimes up to nanoseconds, at least one order of magnitude longer than their intralayer counterpart [Riv15], while still maintaining a large binding energy of $\sim$126 meV [Mer19]. These long lifetimes also make interlayer excitons an ideal candidate to observe exciton condensation [Jau19] or superfluidity [Su08, Fog14, Li17], as well as making valleytronics [Sch16a, Riv16, Bar17, Jin18] possible at room temperature. The strong interaction with light and long lifetimes in combination with electronic control of the interlayer excitons makes them a promising platform for future optoelectronic information technology [Ma16, Unu18, Jau19], potentially bridging the gap between optical data transmission and electronic processing systems.

To fully profit from interlayer excitons and the interlayer charge transfer, a fundamental understanding of these processes on the relevant length and timescales is necessary. The interlayer charge transfer has been investigated by transient absorption and two-color pump-probe spectroscopy to find ultrafast tunneling times of 50 fs [Hon14] and 200 fs [Wan21], respectively. By monitoring the $1s$-$2p$-resonance of the interlayer exciton, the intralayer to interlayer transition (Figure 2.6a, c) was directly observed, finding a transformation of the exciton population within 200 fs, that can be strongly influenced by the twist angle [Mer19]. Focusing on the motion of the charge carriers, THz emission has been used to investigate the interlayer tunneling. Due to the ultrafast nature of the interlayer current, the acceleration of charge carriers leads to the emission of electromagnetic radiation in the THz spectral range (Figure 2.6b). The emitted field is thereby directly proportional to the derivative of the current allowing for direct access to the tunneling dynamics finding transfer times below 100 fs [Ma19].

However, most optical techniques cannot couple efficiently to the out-of-plane dynamics of the interlayer tunneling and due to diffraction, the spatial resolution is strongly limited. Meanwhile, the bandgap and exciton binding energies of TMDC monolayers were found to be extremely sensitive to the dielectric environment [Ste18]. Even local fluctuations including nanoscale height variations, roughness and impurities of the substrate as well as background doping and adsorbates on top of the monolayer influence their electronic and optical properties significantly [Raj19]. In addition, stacking similar monolayers on top of each other can cause the emergence
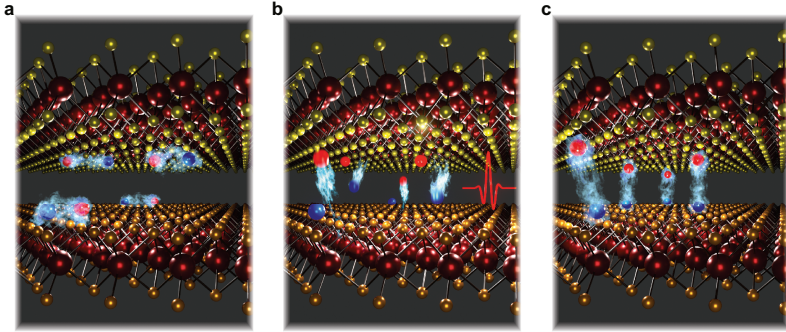
Figure 2.6 | Simplified representation of intralayer and interlayer excitons and the interlayer charge transfer. a, Directly after photoexcitation, electrons and holes interact within the monolayers to form intralayer excitons. **b,** The interlayer tunneling and emission of an electromagnetic wave in the THz spectral range is shown. **c,** After spatial separation, electron and hole still interact and form interlayer excitons. For clarity the carriers are shown in between the layers.

of moiré superlattices, large scale interference patterns, that can reach up to tens of nanometers and should strongly influence the local physical properties and electronic dynamics of the heterostructure [Sey19, Tan20, Reg20].

To provide further insights into the vast variety of new physics of these materials, a tool is needed to observe interlayer tunneling and interlayer exciton dynamics on the relevant nanoscale length and ultrafast timescales without altering or perturbing these interlayer dynamics. Therefore, we combine visible pump/THz probe time-domain spectroscopy with near-field microscopy to obtain unprecedented insights into the nanoscale interlayer dynamics in van der Waals heterostructures by THz emission nanoscopy and subcycle contact-free polarization nanoscopy.

Chapter 3

Field-resolved ultrafast terahertz nanoscopy

Already during the time of the ancient Greeks, philosophers tried to understand light and optical principles including magnification of objects behind spherical glass or globes of water. Over a millennium later, the first modern application of optics occurred in the form of eyeglasses to ease everyday life [Cro04]. With the first microscopes consisting of multiple lenses in 1600, finally, studying nature with far better resolution than the human eye was possible. Within the next century, the resolution was improved drastically by refining lens quality and overcoming spherical and chromatic aberrations allowing microscopy to resolve micron-sized objects and structures [Cro04].

However, soon after, optical microscopy found its limits due to the physical nature of light. As summarized by Ernst Abbé in 1873, diffraction phenomena obscure the details of objects on the order of the wavelength of the light used, known as the diffraction limit [Abb73]. For typical optical microscopes, the resolution is thereby fundamentally restricted to several hundred nanometers.

Since then, scientists found various ways to investigate nature with far better resolution. Using the implications of the diffraction limit, the resolution is improved by using shorter wavelengths. By replacing photons with accelerated electrons, the

foundation for modern scanning transmission electron microscopy was laid, making sub-angstrom spatial resolution possible [Kno32]. Scanning probe techniques like scanning tunneling microscopy and atomic-force microscopy (AFM) allowed for surface imaging down to atomic resolution in 1985 [Bin85]. Here, no light is required and a sharp needle is scanned across the surface using the tunneling current or force between needle and sample to retrieve the topography.

Nonetheless, characterizing materials in a specific wavelength range (energy scale) is crucial. In particular, THz time-domain spectroscopy has proven a valuable tool to investigate electrical and optical properties of a plethora of novel material systems. Characteristic electrical properties like doping density, charge carrier mobility and ultrafast dynamics can be investigated in a non-invasive and contact-free manner [Hub01, Ulb11, Dhi17]. However, the spatial resolution of THz spectroscopy is strongly impacted by the diffraction limit due to the employed long wavelength. Therefore, an approach is needed to not only bypass the diffraction limit with alternative measurement techniques, but to overcome the constraints set by diffraction to perform spectroscopy experiments with sub-wavelength spatial resolution.

As early as 1928, first theories have been proposed, using near-field properties of light propagating through a sub-wavelength aperture, to achieve spatial resolutions better than 100 nm [Syn28]. With the advances in scanning probe techniques in the 1970s and 1980s, further improvements in near-field microscopy have been possible [Hec00]. Ash and Nichols have been the first to overcome the diffraction limit [Ash72] and shortly after, the first near-field microscope was built by Pohl *et. al.* [Poh84]. Others followed soon [Dür86, Bet86] relying on aperture-probes confining the light and reaching spatial resolutions down to 20 nm [Lah96]. However, the aperture-type near-field probes have only efficiently worked for visible and near-infrared light, whereas in the mid-infrared and far-infrared spectral region the fibers show strong attenuation and the metalized waveguides feature a severe cut off [Lah96].

A new concept was proposed using a metalized AFM tip, which scatters the radiation within nanometers of the sample surface. This new technique, called scattering-type scanning near-field optical microscopy (s-SNOM) was rapidly developed in the last decades [Kno99, Kno00, Hil00] and is now able to cover the spectral range from visible to microwave wavelengths with spatial resolutions reaching below 10 nm

[Che19b]. In particular, in the mid-infrared spectrum, ultrafast studies in novel materials were performed [Wag14, Hub17] and even field-resolved experiments with a spatial resolution of 10 nm and simultaneously a subcycle temporal resolution of 10 fs were achieved [Eis14].

In the following, the concept of s-SNOM is discussed and several theoretical descriptions for the tip-sample interaction are introduced including analytical and numerical modeling. Moreover, a novel experimental setup is presented, combining THz time-domain spectroscopy with near-field microscopy allowing for ultrafast subcycle THz near-field spectroscopy to provide an unprecedented perspective on the interlayer dynamics of TMDC heterostructures.

3.1. Concept of scattering-type scanning near-field optical microscopy

Near-field microscopy employs the near-field properties of light to overcome the diffraction limit. Electromagnetic radiation is focused onto an oscillating AFM tip (Figure 3.1a) and couples to the metallic probe leading to a strong field confinement and enhancement at the tip apex. The evanescent fields interact with the sample and lead to the emission of radiation encoding the nanoscale optical properties which are detected in the far field. Due to its evanescent nature, the tip-sample interaction, nonlinearly depends on the tip-sample distance (Figure 3.1b, left). The tapping amplitude (TA) leads to a drastic modulation in the scattered near-field intensity, transforming the sinusoidal mechanical motion into bursts of near-field intensity at the minimum tip-sample separation (Figure 3.1b, bottom right). The recorded far-field signal is still dominated by reflections off the sample surface and cantilever providing no enhanced spatial resolution. Only when demodulating the measured signal at harmonics n of the tip oscillation frequency using a lock-in amplifier, the radiation originating only from the volume just below the tip (E_n) is extracted. As a result, s-SNOM allows for spatial resolution far better than the diffraction limit, depending only on the radius of curvature of the tip and independent of the wavelength of the probe radiation [Hil00, Hil02, vdV02, Ras03, Qaz07, Che19b].
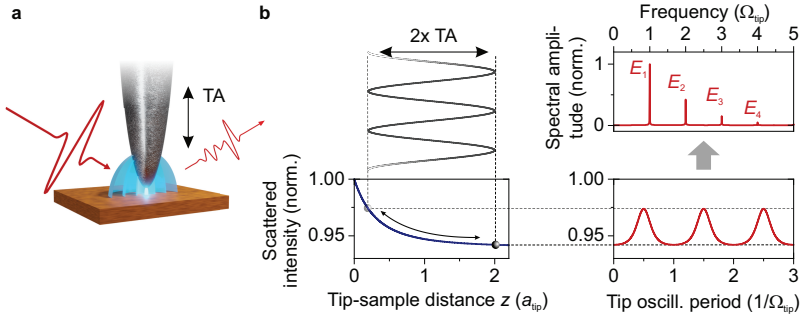
Figure 3.1 | Basic principle of scattering-type scanning near-field optical microscopy (s-SNOM). a, Sketch of tip-sample system showing an incoming electromagnetic wave (red, left) coupling to the tip and sample. The interaction (blue) leads to the emission of a scattered near-field signal (red, right) encoding the local sample properties. The tip is oscillating at a frequency Ω_{tip} and an oscillation amplitude indicated by TA. **b,** Origin of additional harmonic components in the near-field signal used for background suppression. The scattered intensity (bottom left) nonlinearly depends on the tip-sample distance z calculated with the point-dipole model for simplicity. Note that z is given in units of the tip radius a_{tip}. The sinusoidal motion of the tip leads to short burst of intensity (bottom right) at times of minimal tip-sample separation. Using the Fourier transform, the the modulated spectral components are analyzed (top right) featuring signals E_n at harmonics of the original tip oscillation frequency Ω_{tip} that are used to separate the signal from the nanoscopic volume below the tip and far-field contributions.

Understanding the scattering process is crucial for data interpretation and improvements of near-field experiments. Sample properties and dynamics are encoded in the near-field signal, nonetheless they are nontrivial to extract [Che19b]. While reflective optical spectroscopy is well understood, the influences of the probe geometry on the light-matter interaction of tip and sample are more complex [Sid17, Mas17], hence coupling strength, spectral response and field confinement can vary drastically depending on the employed wavelength and tip shape. In addition, due to the strong interaction, tip and sample cannot be treated as individual entities, but have to be modeled as one system [Che19b]. Thereby, due to the tip shape converging from a microscopic volume towards nanometer scale apex, analytical modeling and numeri-

cal simulations have to tackle the challenge of capturing the relevant physics, without running into calculation divergences or reaching computational limits. Nonetheless, during the last decades scientists have achieved significant advances in the predictive power and accuracy of analytical and numerical modeling of the complex tip-sample interaction. In the following, representative models are presented, highlighting key steps in increasing complexity to achieve more accurate predictions.

Point-dipole model

The point-dipole model proposed in the 1990s was the first approach to understand the near-field interaction [Zen95, Kno99, Che19b]. It treats the tip-sample system very intuitively as an interaction of two point dipoles (Figure 3.2a). The metallic probe is approximated by a polarizable sphere with radius a_{tip} and is reduced to a point dipole with distance $z + a_{\text{tip}}$ above the sample surface with z being the tip-sample separation. The sample is treated as infinite half space with dielectric function ϵ_{sample}. When radiation couples to the tip apex, an electric field is applied, polarizing the tip dipole according to $p = \alpha E$. The induced dipole influences the dielectric sample, which is described by an image dipole within the sample with a polarizability $\alpha \times \beta$ and $\beta = \frac{\epsilon_{\text{sample}}-1}{\epsilon_{\text{sample}}+1}$. The interaction of the image dipole and the tip modifies its polarizability significantly. The resulting effective polarizability:

$$\alpha_{\text{eff}} = \frac{\alpha}{1 - \frac{\alpha\beta}{16\pi(a_{\text{tip}}+z)^3}} \tag{3.1}$$

contains the original polarizability $\alpha = 4\pi a_{\text{tip}}^3 \frac{\epsilon_{\text{tip}}-1}{\epsilon_{\text{tip}}+2}$, the tip-sample distance z, the tip radius a_{tip} and the dielectric constant of the sample within β.

The scattered signal E_{scat} is proportional to the induced dipole p_{eff}. Therefore, it is proportional to the effective polarizability α_{eff} and electric field at the tip apex E_0 ($E_{\text{scat}} \propto p_{\text{eff}} = \alpha_{\text{eff}} E_0$). The Fresnel reflections need to be accounted for to determine the field E_0 at the tip apex as well as the scattered electric field E_{scat}, as indicated in Figure 3.2a. Using the Fresnel reflection coefficient r_{p} for p-polarized light we find:

$$E_{\text{scat}} \propto (1 + r_{\text{p}})^2 \alpha_{\text{eff}} E_{\text{in}} . \tag{3.2}$$

The point-dipole model was modified and extended to improve its accuracy for specific experiments, amongst others for anisotropic [Sch05] and layered structures [Aiz08]. Additionally, more complex scattering effects have been taken into account [Por03]. However, since the model only considers vertical electric fields, the quasi-electrostatic approximation is used and field retardation is ignored, mostly qualitative agreement with experiments is found [Che19b]. Quantitative predictions of the near-field contrast, approach curves [Ste03] and spectral features [Oce04, Hub06] in the experiment were still elusive.

Finite-dipole model

The poor quantitative agreement of the point-dipole model led to new approaches with fewer approximations needed. The finite-dipole model [Cvi07] considers the tip as an isolated prolate spheroid to analytically tackle the tip-sample interaction and approximate the metallic probe more accurately. The incident electric field polarizes the spheroid and the resulting electric field is simplified to two monopoles Q_0 and $-Q_0$ at either end of the spheroid (Figure 3.2b). The lower monopole interacts with the sample, described by the mirror charge Q_0'. In turn, Q_0' acts back onto the spheroid and induces a charge density, which is adequately summarized by charges Q_{i} and -Q_{i} within the tip. Due to the larger distance of -Q_{i} to the sample surface, only weak interaction is expected and it is distributed uniformly across the spheroid to ensure charge neutrality. At last, the influence of Q_{i} on itself, mediated by the mirror charge in the sample Q_{i}', is also captured. Thereby, the resulting Q_{i} in combination with the polarized tip can be described by an effective polarizability capturing the tip-sample interaction. The exact derivation is discussed in detail in Reference [Cvi07].

Using the finite-dipole model, approach curves and spectral features on silicon carbide are well reproduced [Cvi07]. Further extensions allow for quantitative predictions of layered structures [Hau12, Moo18] and are used in inversion algorithms to accurately retrieve the full dielectric function in near-field experiments [Gov13, Moo18].
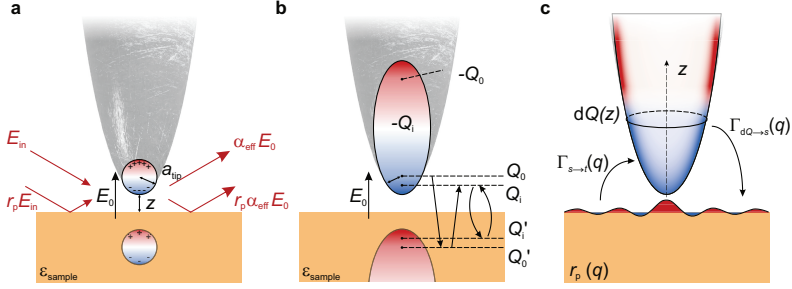
Figure 3.2 | Point-dipole model, finite-dipole model and lightning rod model side by side. a, In the point-dipole model the tip is approximated as a polarizable sphere with radius a_{tip} at the tip apex and the tip-sample distance z. The electric field induces a polarization of the tip apex, which is in turn effecting the sample, captured in an image dipole. The overall polarizability of the two dipoles is used as a measure for the expected near-field signal. **b,** The finite-dipole model simplifies the tip to an elongated spheroid to approximate the tip geometry more accurately. The incident electric field polarizes the spheroid, which is captured in the two monopoles Q_0 and $-Q_0$. The lower monopole interacts with the sample, causing a mirror charge Q_0'. The influence of Q_0' on the tip is captured in Q_i and $-Q_i$. Since Q_i is closer to the sample, it induces another mirror charge Q_i' also acting back on the tip and itself (arrows). $-Q_i$ does not interact with the surface due its larger distance and is distributed uniformly to ensure charge neutrality. **c,** In the lightning rod model, the incident radiation also causes a polarization of the tip, which is approximated by more complex probe shapes, here radial symmetric, leading to a realistic charge distribution. For all charge elements $dQ(z)$, evanescent electric fields propagate to the surface $\Gamma_{dQ \to s}(q)$ and back $\Gamma_{s \to t}(q)$. The key observable is the charge distribution in the polarized probe that is modified by the interaction.

Lightning rod model

While the theoretical advances above can already qualitatively and quantitatively describe many near-field experiments, they still feature drastic simplifications and approximations. Electrodynamic effects like field retardation and antenna resonances due to the tip geometry as well as strong coupling between tip and sample cannot be captured accurately. In addition, most approaches feature a multitude of tunable parameters making predictive modeling unreliable [McL14].

These shortcomings are addressed in the lightning rod model, allowing for exploration of the influence of probe geometry and electromagnetic effects. The exact derivation can be found in [McL14] and only a quick overview is given here (Figure 3.2c). Again, the key observable is the charge distribution in the polarized probe, which is strongly influenced by the tip-sample interaction. The incident electric field causes an instantaneously induced charge distribution within the metal probe. Depending on the probe shape, here a radially symmetric one, the charge distribution is calculated analytically and each ring-shaped charge element $dQ(z)$ interacts with the sample surface by emitting an evanescent field that propagates to the sample $(\Gamma_{dQ \to s}(q))$. The reflection $r_p(q)$ depends on the in-plane momentum q of the near fields emitted by the polarized probe. In turn, the charge distribution on the surface emits evanescent fields that influence the tip polarization $(\Gamma_{s \to t}(q))$. The resulting modified tip polarization then emits radiation into the far field.

Within the model, field retardation, the probe geometry and surface dispersion are included providing a powerful tool for quantitative predictions. Furthermore, the model can be inverted to accurately extract dielectric constants [McL14].

Numerical finite-element method simulations

The analytical solutions discussed above already deliver qualitative and semi-quantitative results, accurately reproducing key experimental findings. However, details of the nanoscale evanescent fields emerging from the probe are still elusive. To access the field distribution in the vicinity of the metal probe, microscopic electrodynamical treatment is necessary, including the propagation and confinement of the electric field within the complete tip-sample system ranging from near to far field.

Thereby, quantitative information about the field distribution of the evanescent fields in the vicinity of the tip as well as within the sample are of particular interest. Only then, we can understand and optimize the spatial resolution and surface sensitivity, and verify commonly accepted empirical knowledge like the influence of the oscillation amplitude and higher demodulation orders on the probing volume. Finite element and finite difference method simulations of the field distribution of a metallic tip have been used to understand the coupling of light to the tip-sample system [Est07, Bre08, Bab17] and optimize the probe geometry for specific wavelengths [Mas17, Sid17].

However, typically the oscillation of the tip is not included, neglecting the effects of tapping amplitude and higher order demodulation for background suppression. To uncover the full tip-sample interaction, we implement finite element method simulations capturing the full motion of the tip [Moo20]. The field distribution in the vicinity of the tip is calculated for different tip-sample distances (Figure 3.3a), showing the highly nonlinear tip-sample interaction. By considering the full oscillation cycle of the tip, the field distribution can be separated into its Fourier components and visualized (Figure 3.3b, c, d). The Fourier spatial maps of the field distribution in the vicinity of the tip apex (b) and the evanescent field penetrating into the sample surface (c) are analyzed and a strong increase in confinement is found for higher demodulation orders, a direct proof for increased spatial resolution and surface sensitivity of higher demodulation orders. In the vicinity of the tip above the surface (Figure 3.3d), the first demodulation order shows asymmetric behavior caused by the far-field background (left), whereas the second order exhibits an almost point-like emission source. It is clearly visible that details in tip geometry are tracked, like additional enhanced fields at the top corners providing access to the
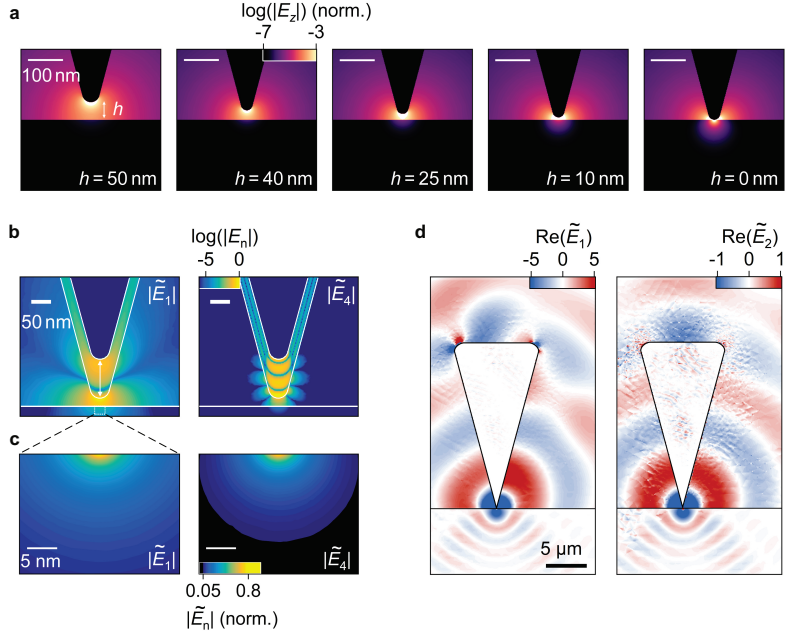
Figure 3.3 | Finite element method simulations of the tip-sample system.
a, Magnitude of the electric field $|E_z|$ confined at the tip apex for a tip height h from 50 to 0 nm. **b,** Fourier analysis of the electric field distribution in the vicinity of the probing tip with a tapping amplitude of 50 nm (white arrow). The minimal tip-sample separation is 20 nm. The solid white lines indicate the outline of the tip at the upper and lower points of inflection and the sample surface. The field confinement of the first demodulation order $|\tilde{E}_1|$ and the fourth demodulation order $|\tilde{E}_4|$ are compared. The region of interest shown in **c** is indicated by the dashed frame. **c,** Fourier analysis of the surface sensitivity comparing the field confinement of the first demodulation order $|\tilde{E}_1|$ and the fourth demodulation order $|\tilde{E}_4|$. **d,** Field distribution for a frequency $\nu = 30$ THz at a tip-sample separation of $h = 0$ nm. Note that the values close to the tip apex strongly exceed the employed color scale. The data is reproduced from [Moo20].

behavior of arbitrarily shaped tips in the future. Being able to accurately simulate the electric field distribution allows for full quantitative understanding of the tip-sample interaction, and can be used to directly extract the influence of the tip shape on the experimental results [Moo20].

Since this concept is independent of the wavelength, we use the knowledge of the tip-sample interaction and extend it to the THz spectral domain for realistic probe geometries. Therefore, these numerical simulations provide the necessary means to link the far-field observables to near-field quantities and understand the nanoscale dynamics.

3.2. Visible pump/terahertz probe nanoscopy experiment

To investigate the interlayer dynamics of TMDC heterostructures, we use s-SNOM at THz frequencies [Hub08, Moo15, Kus16, Mas17, Sti18b, Zha18a, Yao19, Che19b, Sid20] combined with field-resolved electro-optic detection [Che03, Che04, Eis14, Kla17, Piz20] to be able to record the emission signatures of the ultrafast interlayer tunneling (see Chapter 4) and to be especially sensitive to the local electron-hole pair polarizability (see Chapter 5), with a probe frequency below all relevant electronic resonances of the system.

Near-field microscopy experiments, in particular for such long wavelengths, often suffer from low signal strengths due to the nature of the small probing volume, orders of magnitude smaller the the diffraction limit. For example in the mid-infrared spectral range employing radiation centered at a wavelength $\lambda = 8.5\,\mu m$ and a demonstrated spatial resolution of $10\,nm$ [Eis14], the near-field probing volume is more than seven orders of magnitude smaller than the diffraction limited far-field counterpart with an approximated volume of $(\frac{\lambda}{2})^3$ and getting even smaller for longer wavelengths [Moo15, Kus16, Mas17]. To overcome this challenge and achieve a superior signal-to-noise ratio even on atomically thin van der Waals materials, our near-field experiment setup consists of a low-noise, high-power ytterbium-doped yttrium aluminum garnet (Yb:YAG) thin-disk oscillator in combination with a commercial fully non-dispersive s-SNOM.

The experimental setup is sketched in Figure 3.4. The Yb:YAG thin-disk oscillator provides 200-fs-long pulses at a center wavelength of $1030\,nm$ and a pulse energy of up to $3.75\,\mu J$ at a repetition rate of $24\,MHz$, corresponding to an output power of up to $90\,W$ (Section 3.2.1.). For the THz generation process (I) the pulses are focused into a gallium phosphide (GaP) crystal generating phase-stable THz pulses with $100\,\mu W$ average power (Section 3.2.2.). The radiation is collimated using a parabolic mirror and filtered by passing through a Germanium wafer under the Brewster angle. Germanium is only transmissive for wavelengths larger than $1.8\,\mu m$. The THz probe pulses, which are polarized parallel to the tip to ensure efficient coupling, are then focused onto the tip apex in the near-field microscope with the internal,
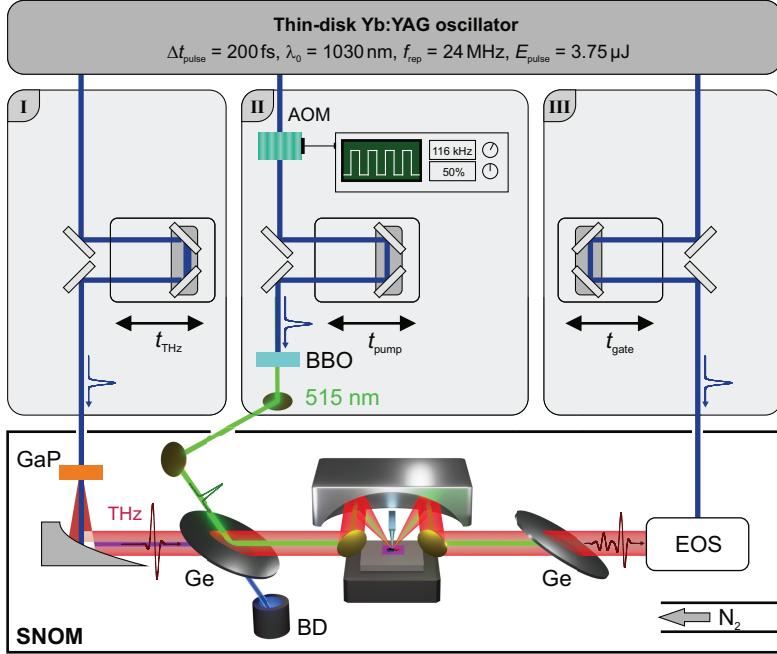
Figure 3.4 | Sketch of the implementation of the ultrafast THz nanoscopy experiment. The optical setup is based on a high-average power low-noise thin-disk oscillator. Its output (I) is directly optically rectified in a gallium phosphide (GaP) crystal to generate phase-stable THz pulses (red), which are transmitted through a germanium wafer (Ge) and focused onto the tip of the near-field microscope. The residual generation light is reflected by the germanium wafer into a beam dump (BD). In addition, a second pulse train (II) is used for photoexcitation of the sample (green). To perform differential measurements the pulses pass through an acousto-optic modulator (AOM, here for example at a modulation rate of 116 kHz and a duty cycle of 50 %). Second harmonic generation in a β-barium-borate (BBO) crystal is employed to provide an excitation wavelength of 515 nm, before being superimposed with the THz probe pulses. The scattered radiation from the tip is collimated and any residual photoexcitation is blocked using a second germanium wafer. The near-field THz waveform is detected using electro-optic sampling (EOS) in combination with a gate pulse directly from the oscillator (III). In addition, the delay times of all beam lines are adjusted using linear stages ($t_{THz}, t_{pump}, t_{gate}$). The microscope and whole beam path of the THz probe is purged with dry nitrogen (N_2).

high-numerical aperture parabolic mirror (NA = 0.46). The near-field microscope is based on an atomic-force microscope, providing motorized sample positioning in three dimensions and allowing for imaging the topography of the sample with 1 nm lateral and 0.1 nm vertical precision. After interacting with the tip-sample system the scattered radiation is collected and collimated by the same parabolic, before being routed to the electro-optic sampling setup (EOS). The whole beam path of the THz probe pulses is purged with dry nitrogen gas (N_2) to avoid water vapor absorption lines.

Photoexcitation is provided by the second arm of the setup (II), which is modulated by an acousto-optic modulator (AOM) and frequency doubled in a β-barium-borate (BBO) crystal. The AOM thereby reduces the overall thermal load on the sample by modulating the pump pulse train at frequencies up to 2 MHz with adjustable duty cycle. Moreover, using the acousto-optic modulation we perform differential measurements, comparing the recorded signal with and without the influence of the photoexcitation to directly resolve the pump-induced change of our system. The 515-nm pulses with a pulse duration of 140 fs are superimposed with the THz radiation by reflection of the backside of the germanium wafer and are also focused onto the tip, whereby the polarization is perpendicular to the tip shaft to reduce the interaction with the tip and guarantee a homogeneous photoexciation of the sample. Since scattered pump radiation can disrupt the detection, the outgoing radiation is filtered by an additional germanium wafer.

The third arm (III) directly provides gate pulses for EOS allowing for field-resolved detection accessing spectral amplitude and absolute spectral phase of the scattered THz radiation (Section 3.2.3.).

The THz probe pulses (t_{THz}), pump pulses (t_{pump}) and EOS gate pulses (t_{gate}) can be delayed in time to allow for specific types of measurements. For example in this work, we change the delay time between THz and gate pulses $t_{\mathrm{THz}} - t_{\mathrm{gate}}$ to access the time-dependent electric field and hence the spectral amplitude and absolute phase of the scattered THz waveform (Figure 3.5a). Changing the pump delay time t_{pump} relative to the THz probe pulses, while tracking the peak electric field (vertical arrow in a, $t_{\mathrm{THz}} - t_{\mathrm{gate}} = 0$ ps) is used to investigate the pump-induced dynamics (Figure 3.5b). By modifying two of the three delay times, two-dimensional
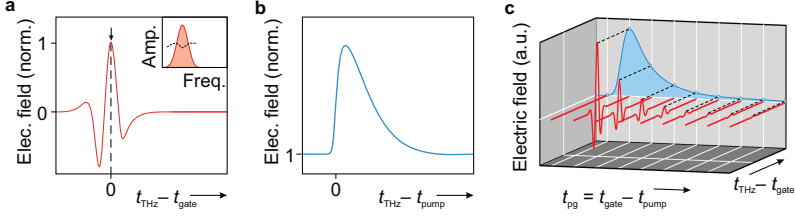
Figure 3.5 | Schematic of possible measurement modes. **a,** By changing the relative delay time between THz probe and gate pulse shifting t_{gate} the time dependent electric field and spectral amplitude (inset, red) and absolute phase (black dashed line) are retrieved. **b,** Varying the pump delay time t_{pump}, while recording the peak electric field (vertical arrow in **a**, $t_{THz} - t_{gate} = 0$ ps) allows for access to the pump-induced dynamics, e.g. free carrier generation in semiconductors leading to an increase in conductivity and scattered signal. **c,** Combining both measurement types is called two-dimensional THz time-domain spectroscopy resolving the evolution of the scattered THz waveform (red) after photoexcitation by scanning $t_{THz} - t_{gate}$ for several pump-gate delay times ($t_{pg} = t_{gate} - t_{pump}$). The schematic assumes a pump-induced change in conductivity without a resonance in the probe spectrum leading only to an overall sharp increase and exponential decay in the electric-field amplitude. Resonant behavior leads to more complex changes to the waveform, as presented for example in the References [Hub01, Hal20].

THz time-domain spectroscopy is achieved to spectrally resolve the time-dependent pump-induced change of the sample in the frequency domain. In this work, we access the time-dependent change to the waveform by setting a certain pump-gate delay time $t_{pg} = t_{gate} - t_{pump}$ and scanning the THz delay stage t_{THz} as seen in the schematic in Figure 3.5c. As a result, we record THz waveforms for different delay times after photoexcitation encoding the spectral response of the sample. Employing the Fourier transform on the individual waveforms the time-dependent pump-induced change of the spectral amplitude and absolute phase can be accessed. Two-dimensional THz time-domain spectroscopy has proven itself especially useful to investigate the ultrafast dynamics of photo-induced carriers [Hub01, Eis14] or monitor the subcycle non-adiabatic switching of deep strong coupling [Hal20].

3.2.1. Ultrafast thin-disk oscillator

Near-field microscopy is commonly understood and modeled (see Section 3.1.) as the interaction of light with an oscillating metallic tip close to a sample surface assuming continuous wave (CW) illumination, while ultrafast studies of matter are only possible using ultrashort light pulses interacting with the near-field probe for only a fraction of its mechanical oscillation. To avoid artifacts due to undersampling, ultrafast lasers with repetition rates far greater than the tip oscillation frequency are used to capture the full motion of the near-field probe. In addition, due to the nanoscopic probing volume in the near-field, a high power probe beam is needed to investigate the sample systems with superior signal-to-noise ratio. Therefore, we chose a thin-disk oscillator as the centerpiece of the experiment. It provides ultrashort near-infrared pulses at a repetition rate of 24 MHz to ensure that multiple pulses are focused onto the near-field microscope tip during one oscillation cycle ($< 500\,\text{kHz}$), while maintaining sufficient pulse energy to custom-tailor the oscillator output using nonlinear optical effects.

The main advantage of thin-disk oscillators is their very high and scalable optical intensity without damaging the active medium or experiencing undesirable thermal effects. By employing an active medium with a thickness on the order of 100 to 200 µm, directly connected to a heat sink, the thin-disk is efficiently cooled and allows for large pump powers [Mül04]. Thereby, the heat flux is perpendicular to the surface reducing unwanted thermal effects like thermal lensing or phase and polarization distortion that reduce the beam quality [Gie94]. The active medium disk acts as a mirror in the laser cavity featuring an anti-reflection coating at the front side and a highly reflective coating on the backside, which is mounted to the heat sink. To ensure sufficient absorption of the pump radiation in the crystal disk despite the low thickness, the pump light must propagate parallel to the surface guided by total internal reflection (side pumping), or pass through the thin disk multiple times (multipass pumping) [Mül04]. Additionally, the thin-disk concept can be combined with passive mode locking to achieve high powers in the femtosecond regime [Mül04, Pro11, Sar12, Sal19] providing a clean temporal and spectral shape, which is important for many applications in particular those involving frequency conversion [Aus00, Mül04]. Recent results include high power CW operation up to

10 kW from a single disk [Got12] and sources up to 350 W in the femtosecond regime [Pro11, Sar12, Sal19] allowing for high power frequency conversion to generate THz [Mey20] and mid-infrared radiation [Pup15, Zha18b, Sei18]. Thereby, the pulses are intense enough for extreme ultraviolet generation [Kel03, Süd08, Gra19] and many industrial applications [Sar19]. Thin-disk oscillators can provide ultrashort high-average power pulses at the noise level of an oscillator, without additional external amplification and are therefore ideally suited for our experiment.

Our oscillator consists of the typical elements of a laser cavity seen in Figure 3.6a: two end mirrors (EM) and an active medium (Yb:YAG disk), which is pumped by radiation from fiber-coupled laser diodes centered at a wavelength of 940 nm (purple) that passes multiple times through the disk. For pulsed operation, chirped mirrors (CM) are added to counteract dispersion caused by air or transmissive optics in the oscillator. In general, the refractive index experienced during transmission through matter is frequency dependent leading to a stretching of the near-infrared pulse and can be counteracted by a specific kind of dielectric mirrors, so called dispersive or chirped mirrors (see also Section 6.2.). To allow for Kerr-lens mode locking, a Kerr aperture (KA) is incorporated into the beam path and the beam is focused through a Kerr material (KM) using two spherical mirrors (SM1, SM2). All optics mounts and the monolithic aluminum housing are water-cooled to provide long term stability.

To generate ultrashort laser pulses, the oscillator is Kerr-lens mode locked. Kerr lens mode locking is based on the nonlinear optical Kerr effect, that describes an intensity dependent refractive index within the medium (Figure 3.6b). The concept relies on the drastic difference in the peak intensities of CW and pulsed operation mode. Within the Kerr medium the intensity dependent refractive index combined with the Gaussian mode profile leads to a lensing behavior, called self-focusing, which is much stronger for light pulses compared to CW radiation [Sal91, Pas09]. By limiting the spatial mode diameter using a metal aperture (KA), the oscillator design favors the modes with the highest intensities i.e. shortest pulses. Hence, CW as well as broadband modes with random phases are suppressed, while the gain is maximized for broadband emission with the correct constructive phase relation, providing ultrashort mode-locked laser pulses [Sal91].
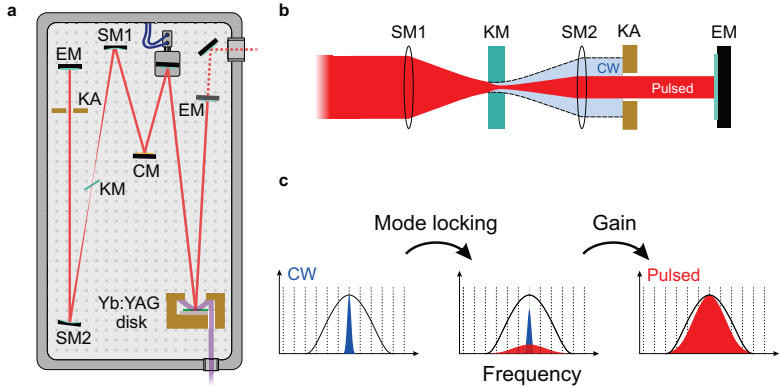
Figure 3.6 | Thin-disk oscillator. a, Simplified schematic of the oscillator setup consisting of an active medium (Yb:YAG disk) and two end mirrors (EM), forming the cavity. The active medium is pumped by radiation from fiber-coupled laser diodes centered at a wavelength of 940 nm (purple) that passes multiple times through the disk. In addition, chirped mirrors (CM) are added for dispersion control. To allow for mode locking, the beam is focused into a Kerr medium (KM) by two spherical mirrors (SM1, SM2) and a Kerr aperture (KA) is implemented. **b,** The basic concept of Kerr lens mode locking is shown. The laser radiation is focused into the Kerr medium by spherical mirrors (here represented by lenses for clarity). The CW radiation (blue) is collimated featuring the same mode size as before. The pulsed operation mode (red) is additionally focused within the Kerr medium due to the Kerr effect (self focusing) and ends up with a smaller mode size. Therefore, the cavity favors the pulsed mode by inducing losses for the CW mode by blocking larger beam diameters using the Kerr aperture. **c,** Simplified spectra of different operation modes. The vertical dashed lines represent the cavity-supported modes and the black curve the emission spectrum of the active medium. In CW operation mode, only a narrowband spectrum is emitted (blue, left). By triggering the mode locking, a broadband mode emerges (red, center). The design of the laser cavity favors the pulsed operation mode, and suppresses the residual CW (right) resulting in a stable femtosecond pulse train. For clarity, very few cavity modes are shown and a continuous spectrum is drawn.

Generally, lasing is an interplay of the allowed modes within the cavity (Figure 3.6c, left, vertical lines) and the emission spectrum of the active medium (black line). When sufficient energy is transferred to the active medium to achieve population inversion [Koe06] and the gain within the laser cavity overcomes the cavity losses, the oscillator starts to emit laser radiation at the most favorable allowed mode (left, blue) resulting in stable CW emission. To trigger the mode locking, the cavity needs to be perturbed e.g. with a movable mirror, causing many modes to be populated (center, red). Due to the higher gain of the mode-locked pulses, they are amplified with every additional pass through the cavity, eventually suppressing the CW mode completely.

Finally, the output of the laser in pulsed operation mode is 90 W at 24 MHz, delivering a high-power low-noise pulse train with 3.75 µJ in pulse energy and a pulse duration of 200 fs, ideally suited for our near-field microscopy experiments.

3.2.2. Terahertz generation

In linear optics the interaction of light with matter leads to a polarization of the medium directly proportional to the external electric field. Thereby, the propagation of light is described by the complex-valued refractive index $n(\omega)$, which is largely determined by its frequency ω and can be used to accurately predict reflection, transmission or refraction at interfaces. Although the linear-response approximation is valid in the special case of small electric field amplitudes, it must be adapted for high field strengths that can be easily reached with pulsed laser radiation, where nonlinear effects contribute significantly to the light-matter interaction, modifying the refractive index $n(\omega)$ dramatically.

The polarization $\vec{P}(t)$ of a material depends on the incident electric field $\vec{E}(t)$ and is given by:

$$\vec{P}(t) = \underbrace{\epsilon_0 \chi^{(1)} \vec{E}(t)}_{\vec{P}^{(1)}(t)} + \underbrace{\epsilon_0 \chi^{(2)} \vec{E}^2(t)}_{\vec{P}^{(2)}(t)} + \underbrace{\epsilon_0 \chi^{(3)} \vec{E}^3(t)}_{\vec{P}^{(3)}(t)} + \dots . \tag{3.3}$$

$\chi^{(i)}$ are linear and nonlinear optical susceptibilities of the material and ϵ_0 is the permittivity of free space [Boy08]. Thereby, the linear optical susceptibility $\chi^{(1)}$ is closely related to the refractive index $n(\omega) = \sqrt{1 - \chi^{(1)}(\omega)}$ and prominently used for example in ray and wave optics [Sal91]. In contrast, as a consequence of the nonlinear optical susceptibilities the light-matter interaction is not only frequency dependent, but also crucially influenced by the external electric field amplitude $\vec{E}(t)$ causing a plethora of fascinating phenomena [Boy08] that can be used to custom tailor the properties of light, for example second-harmonic generation, sum- and difference-frequency mixing and parametric amplification, as well self-phase modulation, self-focusing and four-wave mixing [Sal91, Boy08].

In this work, difference frequency generation (DFG) is employed to generate ultra-short phase-stable THz pulses. DFG is a second order nonlinear effect, captured in $\vec{P}^{(2)}(t)$. When mixing two driving fields $\vec{E}_{\mathrm{DFG}}(t) = \vec{E}_1 e^{-i\omega_1 t} + \vec{E}_2 e^{-i\omega_2 t} + \mathrm{c.c.}$, where c.c. is the complex conjugate, the second order polarizability $\vec{P}^{(2)}(t)$ leads to the generation of new frequencies:

$$\vec{P}^{(2)}(t) = \epsilon_0 \chi^{(2)} \vec{E}^2_{\text{DFG}}(t)$$

$$= \epsilon_0 \chi^{(2)} \left(\vec{E}_1 e^{-i\omega_1 t} + \vec{E}_2 e^{-i\omega_2 t} + \text{c.c.} \right)^2$$

$$= \epsilon_0 \chi^{(2)} \Big(\vec{E}_1 \vec{E}^*_1 + \vec{E}_2 \vec{E}^*_2 + \vec{E}_1 \vec{E}_1 e^{-2i\omega_1 t} + \vec{E}_2 \vec{E}_2 e^{-2i\omega_2 t} \qquad (3.4)$$

$$+ 2\vec{E}_1 \vec{E}_2 e^{-i(\omega_1 + \omega_2)t} + 2\vec{E}_1 \vec{E}^*_2 e^{-i(\omega_1 - \omega_2)t} + \text{c.c.} \Big).$$

In particular, the second harmonic $2\omega_{1/2}$, the sum frequency $\omega_1 + \omega_2$ and difference frequency $\omega_1 - \omega_2$ emerge [Boy08]. In terms of a photon energy-level diagram (Figure 3.7a), DFG can be understood as the excitation of a virtual energy level by ω_1 followed by a two-photon emission process that is stimulated by ω_2 generating radiation at frequency $\omega_3 = \omega_1 - \omega_2$ [Boy08].

To ensure efficient generation of ω_3 along the full length of the nonlinear crystal, the polarization of the nonlinear medium caused by the frequencies ω_1 and ω_2 and the generated electric field at frequency ω_3 need to be in phase leading to constructive interference [Boy08]. This is achieved when the so called phase-matching condition is met:

$$k(\omega_1) = k(\omega_2) + k(\omega_3) \qquad (3.5)$$

with $k(\omega_i) = \frac{\omega_i \, n(\omega_i)}{c}$. Alternatively, phase matching can be understood as momentum conservation in the photon picture: a photon at ω_1 is annihilated, creating a photon at ω_2 and a photon at ω_3. In isotropic normal dispersive media the refractive index $n(\omega)$ increases with higher frequencies ω leading to $n(\omega_1)$ being larger than $n(\omega_2)$ and $n(\omega_3)$. Since $\omega_1 = \omega_2 + \omega_3$ the phase-matching condition (3.5) cannot be fulfilled [Boy08]. Therefore, typical difference frequency generation schemes use more complex nonlinear crystals featuring birefringence to achieve critical phase matching or artificially constructed materials to allow for quasi-phase matching [Boy08].

For the near-field experiment, we generate the THz radiation using the broadband pulses of the thin-disk oscillator output. In the theoretical description above, the involved frequencies ω_1 and ω_2 are treated as independent beams or pulses, but can also be part of the same ultrashort laser pulse with sufficient bandwidth of several THz. Figure 3.7b sketches the mixing process in frequency space. Two frequencies ω_1 and ω_2 of the same pulse in the near infrared at a frequency of $\sim 290\,\mathrm{THz}$ generate a phase-stable THz pulse at ω_{THz} between 0 and 5 THz. This process is called intra-pulse DFG or optical rectification. A phase-stable pulse train features waveforms with the same shape of the electric field in the time domain from laser shot to laser shot. By using difference-frequency mixing in combination with only a single laser source, any phase fluctuations in the generation light are canceled during the mixing process resulting in the generation of phase-stable THz pulses.

Similar to before, phase matching needs to be considered. In this case not only for two distinct frequencies but a continuous spectrum mixing with itself [Sal91]. The phase-matching condition $k(\omega_1) = k(\omega_2) + k(\omega_{\mathrm{THz}})$ can be rewritten as the phase mismatch $\Delta k = k(\omega_1) - k(\omega_2) - k(\omega_{\mathrm{THz}})$. For the case of zero phase mismatch $\Delta k = 0$, the phase-matching condition of Equation (3.5) is fulfilled. We can further simplify:

$$\Delta k = k(\omega_1) - k(\omega_2) - k(\omega_{\mathrm{THz}}) \tag{3.6}$$
$$= k(\omega_2 + \omega_{\mathrm{THz}}) - k(\omega_2) - k(\omega_{\mathrm{THz}}) \tag{3.7}$$

using $\omega_1 = \omega_2 + \omega_{\mathrm{THz}}$. Due to the fact, that the bandwidth of the near-infrared pulse is far smaller than its center frequency, we can assume $\omega_{\mathrm{THz}} \ll \omega_1, \omega_2$, and approximate

$$k(\omega_2 + \omega_{\mathrm{THz}}) \approx k(\omega_2) + \omega_{\mathrm{THz}} \left.\frac{\mathrm{d}k}{\mathrm{d}\omega}\right|_{\omega_2} + \dots . \tag{3.8}$$

Using this Taylor series expansion, we simplify the expression (3.7) to

$$\Delta k \approx \omega_{\text{THz}} \frac{dk}{d\omega}\bigg|_{\omega_2} - k(\omega_{\text{THz}}) = \omega_{\text{THz}} \left(\frac{1}{v^{\text{group}}(\omega_2)} - \frac{n(\omega_{\text{THz}})}{c} \right) \qquad (3.9)$$

with $k(\omega_i) = \frac{\omega_i n(\omega_i)}{c}$ and the group velocity of the light pulse $v^{\text{group}}(\omega_2) = \frac{d\omega}{dk}\big|_{\omega_2}$. Finally, using $c_{\text{THz}}^{\text{phase}}(\omega_{\text{THz}}) = \frac{c}{n(\omega_{\text{THz}})}$, the phase velocity in the material at frequency ω_{THz}, we get:

$$\Delta k \approx \omega_{\text{THz}} \left(\frac{1}{v^{\text{group}}(\omega_2)} - \frac{1}{c_{\text{THz}}^{\text{phase}}(\omega_{\text{THz}})} \right). \qquad (3.10)$$

The mixing process is most efficient when the THz phase velocity $c_{\text{THz}}^{\text{phase}}(\omega_{\text{THz}})$ is equal to the group velocity $v^{\text{group}}(\omega_2)$ of the near-infrared pulse. This can be qualitatively understood as the mixing pulses propagating through the crystal as fast as the THz phase to add more and more generated light constructively.

By modeling the mixing process starting with the nonlinear wave equation, the expected generated radiation can be predicted by the following relation[1] [Hub00]:

$$\left| \tilde{E}_{\text{THz}}(L, \omega_{\text{THz}}) \right| = \left| \frac{2 d_{\text{eff}} \omega_{\text{THz}}^2}{k(\omega_{\text{THz}}) c^2} \int d\omega \left(\tilde{E}(\omega) \tilde{E}^*(\omega - \omega_{\text{THz}}) \frac{e^{i \Delta k(\omega, \omega_{\text{THz}}) L} - 1}{\Delta k(\omega, \omega_{\text{THz}})} \right) \right| \qquad (3.11)$$

describing the generated THz amplitude spectrum $|\tilde{E}_{\text{THz}}|$ at the end of the generation crystal for arbitrary complex electric field amplitudes $\tilde{E}(\omega)$ of the generation pulse. Here, ω is integrated over the whole near-infrared spectrum and L describes the crystal thickness [Hub00]. The nonlinear coefficient d_{eff} is proportional to the second-order nonlinear susceptibility $\chi^{(2)}$, which depends on the specific crystal axis and frequency of the radiation [Boy08]. Since we implement the DFG with a GaP crystal, that exhibits optimal phase matching close to normal incidence, we neglect angle dependence of d_{eff} and $\Delta k(\omega, \omega_{\text{THz}})$ as well as the frequency-dependent Fresnel reflection at the crystal facets.

More intuitively, the generated intensity spectrum $I_{\text{THz}} = \left| \tilde{E}_{\text{THz}}(L, \omega_{\text{THz}}) \right|^2$ is considered. The fraction within the integral can be reduced to [Boy08]:

---

[1]Similar forms of the equation can be found in [Boy08] and [Gal99].

$$\left|\frac{e^{i\Delta k L} - 1}{\Delta k}\right|^2 = L^2 \operatorname{sinc}^2\left(\frac{\Delta k\, L}{2}\right) \tag{3.12}$$

where sinc(x) is the sinus cardinalis. Note that the frequency dependence of $\Delta k(\omega, \omega_{\mathrm{THz}})$ was dropped for clarity. With this simplification and by representing $|\tilde{E}(\omega)|^2 \equiv I_{\mathrm{NIR}}$, the key parameters for THz generation can be identified:

$$I_{\mathrm{THz}} \propto I_{\mathrm{NIR}}^2\, d_{\mathrm{eff}}^2\, L^2\, \operatorname{sinc}^2\left(\frac{\Delta k\, L}{2}\right). \tag{3.13}$$

The generated intensity I_{THz} depends quadratically on the near-infrared intensity I_{NIR} of the generation pulse, the nonlinear coefficient d_{eff} and the thickness of the non-linear mixing crystal L [Boy08]. The phase mismatch Δk will lead to the main maximum for $\Delta k = 0$ describing constructive interference of the constituent frequencies along the whole length of the crystal.

In our experiment, we chose a GaP crystal due to its advantageous properties at the output wavelength of the thin-disk oscillator of 1030 nm: it has a sufficiently large nonlinear coefficient d_{eff} and supports a large bandwidth due to very similar group and phase velocity of the near-infrared pulses and the THz radiation, respectively [Neg11]. In addition, GaP crystals feature a very high damage threshold, ideally suited to withstand high near-infrared intensities [Xu18, Mey18] and generate THz radiation with high-average powers (compare Equation 3.13). In Figure 3.7c, the near-infrared group velocity for a frequency of 290 THz ($v_{\mathrm{NIR}}^{\mathrm{group}}$) and the frequency dependent THz phase velocity $c_{\mathrm{THz}}^{\mathrm{phase}}(\omega)$ are shown [Bar68]. Since there is very little difference up to 3 THz, good phase matching is expected. For even higher frequencies the deviation increases due to the transversal optical phonon resonance of GaP at 11 THz.

Using Equation (3.11), the generated THz spectral amplitude can be calculated for the near-infrared pulses of the thin-disk oscillator for different crystal thicknesses (Figure 3.7d). The result shows very broadband generation for thin crystals and more narrowband, but more intense, spectra for longer crystal thicknesses. Additionally, the phase matching in longer crystals results in an oscillatory behavior in the electric field amplitude for different frequencies (top right) caused by the secondary maxima of the sinc function.
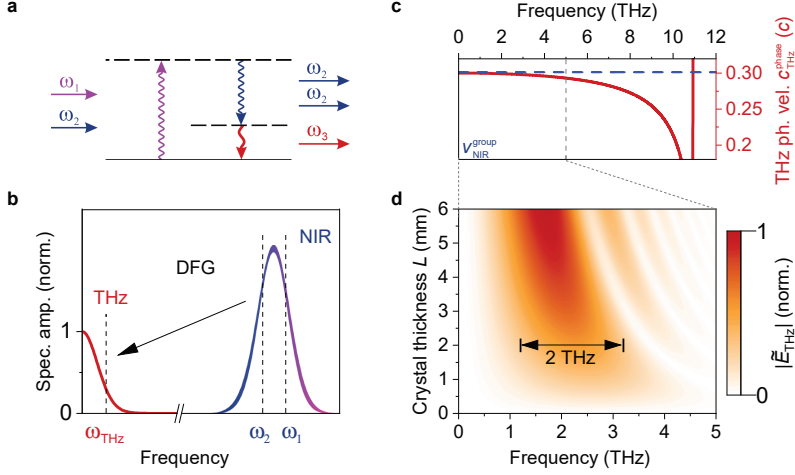
Figure 3.7 | THz generation using difference-frequency mixing. a, Energy diagram for difference-frequency generation (DFG). A virtual energy level is excited by ω_1 followed by a two-photon emission process that is stimulated by ω_2 generating radiation at frequency $\omega_3 = \omega_1 - \omega_2$. **b,** The mixed frequencies ω_1 and ω_2 are not part of separate pulses, but located at the spectral wings of a single ultrashort laser pulse and are used to generate THz radiation by intra-pulse DFG. **c,** Frequency dependent THz phase velocity $c_{\mathrm{THz}}^{\mathrm{phase}}(\omega)$ (red) and near-infrared group velocity $v_{\mathrm{NIR}}^{\mathrm{group}}$ for 290 THz (dashed blue line) in GaP [Bar68]. **d,** Two-dimensional phase-matching plot for GaP providing the calculated spectral amplitudes $|\tilde{E}_{\mathrm{THz}}|$ of the generated THz radiation for different crystal thicknesses L as a function of THz frequency. A bandwidth of 2 THz full width at half maximum (FWHM) is predicted for the 2-mm-thick crystal employed in the experiment.

To generate the THz probe pulses in the experiment, we use a 2-mm-thick GaP crystal, to achieve the optimal balance between bandwidth and field strength. We focus up to 20 W of average optical power (corresponding to a pulse energy of $\sim 0.85\,\mu\mathrm{J}$) with a beam diameter of 70 μm into the crystal. The peak intensity within the focus is $110\,\mathrm{GW/cm^2}$, which is high enough to drive the nonlinear mixing process, but still low enough to avoid unstable behavior or damage of the GaP crystal. As a result, we generate phase-stable broadband THz pulses at an average power of 100 μW that are used as the probe in the near-field experiment.

3.2.3. Field-resolved detection

The technique of electro-optic sampling (EOS), which is often described as an "oscilloscope for light", is employed to trace the oscillating electric field of the THz radiation with subcycle temporal resolution and thereby reconstruct the waveform of our THz pulses. From this information the spectral amplitude and absolute spectral phase can be retrieved.

The detection mechanism of EOS relies on the Pockels effect. External electric fields applied to an electro-optic crystal induce a birefringence depending on the electric field strength [Boy08] and thereby, encoding the properties of the applied electric field into the optical properties of the detection crystal. The induced birefringence can be monitored by its influence on the polarization state of probe light passing through the crystal. By using an ultrashort light pulse for the readout, the so called gate pulse, that is even shorter than one oscillation period of the THz radiation, the THz waveform can be considered a static external electric field applied to the crystal lattice [Mit03]. Therefore, the instantaneous THz electric field is encoded into the crystal properties and modifies the polarization of the ultrashort gate pulse.

In the experiment, THz and gate pulses are superimposed and focused into the electro-optic crystal (GaP, I, Figure 3.8a). The instantaneous electric field of the THz pulse induces a birefringence within the electro-optic crystal, which modifies the linearly polarized gate light (blue) by phase retardation and polarization rotation, resulting in elliptical polarized light [Mit03]. Alternatively, this process can be understood as sum- and difference-frequency generation of gate and THz light, resulting in frequencies close to the gate spectrum with perpendicular polarization, effectively leading to an elliptical polarized gate pulse [Gal99]. Therefore, the THz field strength is imprinted onto the polarization state of the gate pulse (II) and is analyzed using a quarter-wave plate ($\lambda/4$), a Wollaston prism and a balanced photodiode circuit. When no THz field is present, the quarter-wave plate is oriented to transform the linearly polarized gate pulse into purely circular polarized light. The Wollaston prism separates horizontal and vertical polarized radiation, leading to the same power on both photodiodes and no signal ($\Delta I = 0$) is detected by the balanced circuit. When the THz field is non-zero (blue arrows, Figure 3.8b), it leads to elliptical polarization of the gate pulse after the electro-optic crystal and deviates
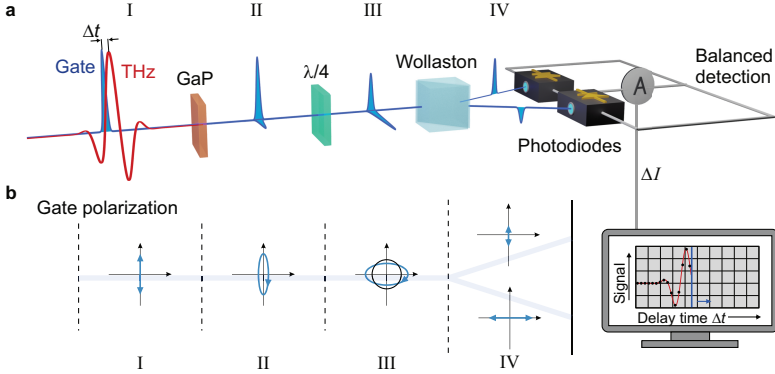
Figure 3.8 | Experimental setup of the electro-optic sampling. a, THz and gate pulse are overlapped spatially and focused into the GaP crystal (I). The instantaneous electric field of the THz pulse induces a birefringence causing a change in the gate polarization from linear to elliptical (II). After passing a quarter waveplate (III) the beam is split by a Wollaston prism to separate vertically and horizontally polarized light (IV) and detected by a photodiode circuit. For no incident electric field, the quarter wave plate is aligned so that perfectly circular polarized light is split equally by the Wollaston prism and the balanced diodes show no signal. **b,** The various polarization states after each optical component are shown. By varying the time difference Δt between THz and gate pulse, consecutive pulses can stroboscopically sample the full waveform (right).

from circular polarization after the quarter-wave plate (III). This small imbalance (IV) on the photodiodes ΔI is in first approximation linear to the THz electric field and is sensitively detected down to the shot noise limit using lock-in amplification, whereby the THz pulse train is typically modulated by an optical chopper or in the near-field experiment by the oscillation of the near-field tip. To reconstruct the THz waveform, the delay time between THz and gate pulse is scanned in order to stroboscopically sample the whole transient (Figure 3.8b, right). Thereby, the phase-stability of the THz pulses is essential, since each interaction of THz and gate pulse only captures a single point of the time-dependent THz electric field. As a result, the THz waveform is resolved with a time resolution only limited by the gate pulse duration of 200 fs.

However, while this is true in theory, real crystals in the experiment exhibit frequency dependent detection sensitivity due to the following effects.

High-pass filtering due to focusing

In the experiment, THz and gate beam are overlapped using an off-axis parabolic mirror focusing the THz radiation tightly (focal length: 25 mm), while the gate pulses are passing through the hole perpendicular to its optical axis (Figure 3.9a, inset). Considering THz frequencies at 1 and 2 THz, the drastically different wavelengths (150 and 300 µm) in combination with diffraction lead to large differences in their respective focal spot sizes (Figure 3.9a). Lower frequencies or longer wavelengths (red) lead to weaker focusing and therefore less confined, less intense electric fields that are detected by the gate pulse (blue). To estimate the difference in detection sensitivity depending on the THz frequency, which is caused by the imaging optics in the experiment, we integrate the field strength of the THz radiation within the interaction volume with the gate beam, which is set by the gate beam diameter and the crystal length of 4 mm. We assume equal field strengths and collimated
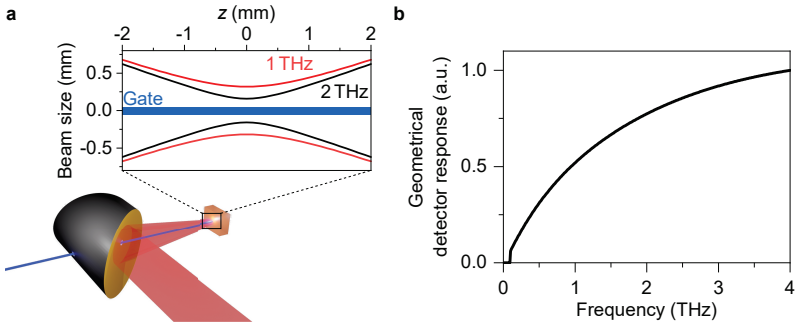
Figure 3.9 | Geometrical detector correction due to focusing. a, Spatially overlapping THz (red) and gate (blue) pulse using a parabolic mirror with a through hole. The beam sizes of focused radiation at 1 and 2 THz (red, black) and the collimated gate pulse (blue) are plotted along the optical axis. **b,** Normalized response function calculated using the spatial overlap of gate pulse and different THz frequencies in a 4-mm-long crystal.

beam diameters of 12.5 mm FWHM for all THz frequencies before the parabolic mirror, similar to the experimental geometry, and employ Gaussian beam propagation to compute the focusing. A constant beam size of 100 μm is set for the gate beam within the crystal, reflecting the weak focusing in the experiment. As a result, we find an increased detection sensitivity for higher THz frequencies leading to a high-pass filtering of the detected spectrum (Figure 3.9b), that is also observed experimentally.

Detection crystal response

Similar to the generation process, sensitive and efficient detection is only achieved, when THz and gate pulse co-propagate and the nonlinear detection mechanism stays in phase along the crystal length. Therefore, phase matching between both pulses and dispersion effects, that lead to stretching and deformation of the THz pulse in the time domain, have to be accounted for [Küb04, Kam07].

The resulting detector response function for amplitude and phase is shown in Figure 3.10a. In the experiment, we use a 3-mm and a 4-mm-thick GaP crystal. The thinner one to resolve the full spectrum of our generated THz radiation, since the detection is more broadband for shorter crystals. The longer one is employed to be extremely sensitive for the minuscule emission signals in the experiment trading bandwidth for signal strength. Both show a detection bandwidth larger than 3 THz (top), whereby the 3-mm-thick crystal features a slightly more broadband phase matching (dashed lines). Similar to the generation process, we see an additional contribution to the detected spectral phase for frequencies higher than 2 THz (bottom), due to mismatched phase and group velocity of the THz and gate pulse, respectively.

We combine the geometrical high-pass filtering and the detector crystal effects to one complete detector transfer function, which is shown in Figure 3.10b describing the frequency sensitivity and phase shift due to the detection process for the 3-mm-thick (4-mm-thick) detector crystal. The detection scheme is sensitive to frequencies from 0.1 to 3.5 THz (3.2 THz), with an increasing added phase for higher frequencies. For even higher frequencies, we observe oscillatory behavior of amplitude and phase due to the phase mismatch.
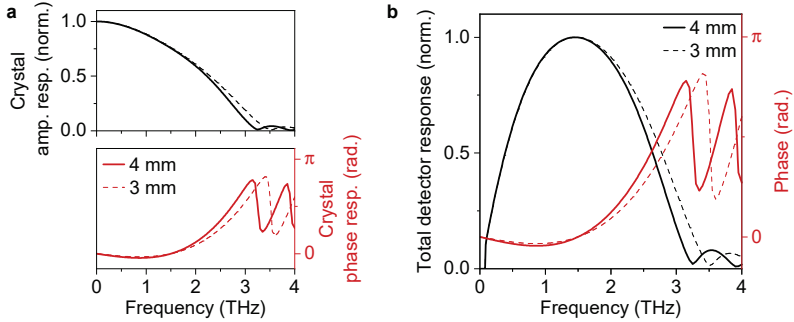
Figure 3.10 | Detector response of the electro-optic detection crystal.
a, Amplitude and phase response function calculated for a GaP crystal with a
thickness of 3 mm and 4 mm. **b,** Full detector response combining the geometri-
cal high-pass filtering and the crystal frequency response for the GaP crystals.

Corrected THz waveform

Having understood the generation and detection process, we can finally show the
real THz waveform used in our experiments, generated by intra-pulse DFG in a
2-mm-thick GaP crystal. In Figure 3.11a the field-resolved THz pulse detected with
a 3-mm-thick GaP crystal is shown (red). The transient consists of an asymmetric
single cycle, followed by a few small oscillations. The gray curve shows the corrected
waveform, which is calculated by dividing the recorded spectrum by the detector
transfer function. In addition, frequencies below 0.15 THz and higher than 3.1 THz
are filtered to avoid divergences. The corrected transient mainly differs in the first
negative half cycle and shows reduced trailing oscillations. Considering the spectral
amplitude and phase in Figure 3.11b and c, we see generated THz frequencies from
0.2 to almost 3 THz and only a slight increase in spectral phase for higher frequencies
(Figure 3.11c, red). The detector correction mainly impacts the spectral phase
leading to an almost flat phase along the whole spectrum (gray). Compared to
the predicted electric fields in Figure 3.7d, we find a reduced bandwidth of 1.6 THz
full width at half maximum and a shift towards lower frequencies, which could be
caused by the hole in the parabolic, used for superimposing THz and gate pulses,
influencing higher frequencies more strongly and leading to an additional low-pass
filtering in the detection.
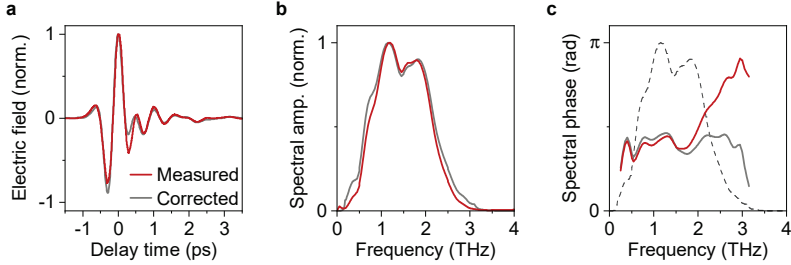
Figure 3.11 | Generated THz probe pulse for the near-field experiment.
a, Field-resolved THz waveform as detected with EOS (red). By accounting for the detector response function the actual generated waveform is reconstructed (gray). **b,** Detected (red) and corrected (gray) THz spectral amplitude. **c,** Detected (red) and corrected (gray) spectral phase. The dashed line represent the corrected spectrum (**b**) as reference.

In this chapter, we discussed the experimental foundations and the theoretical background of near-field microscopy, to precisely understand the light-matter interaction in the vicinity of the sharp metallic tip. Furthermore, a novel experimental setup has been introduced providing high repetition rate and high average power phase-stable THz probe pulses in combination with field-resolved detection of the scattered near fields. In the next chapters, we use these ideal prerequisites to investigate the interlayer dynamics of TMDC heterostructures on nanometer length- and ultrafast timescales.

THz time-domain spectroscopy and THz emission nanoscopy of transition metal dichalcogenide heterostructures

4.1. Sample fabrication and characterization

The TMDC heterostructures are produced using an all-dry viscoelastic stamping method [CG14]. First, monolayers of sufficient size have to be exfoliated, which will be combined to the heterostructure afterwards. For different materials, the steps are modified empirically to achieve better quality or larger samples, but the key steps are listed in the following:

So called Nitto tape, featuring a very low adhesive force, is brought into contact with the mm-sized bulk single crystal (see Figure 4.1, I) to peel off thin flakes of the material. The flakes can be additionally thinned down and cleaned of debris by repeatedly pushing a second piece of Nitto tape onto the surface and peeling it off. The sufficiently thinned down crystal is pushed onto a viscoelastic poly-dimethyl-siloxane (PDMS) film on a microscope slide (II). By gently lifting the tape, monolayer flakes can remain on the PDMS. Using an optical microscope, these are identified and pre-characterized. A typical area (II, bottom) contains remaining bulk material, but also shows few-layer, bilayer (BL) and monolayer (ML) regions
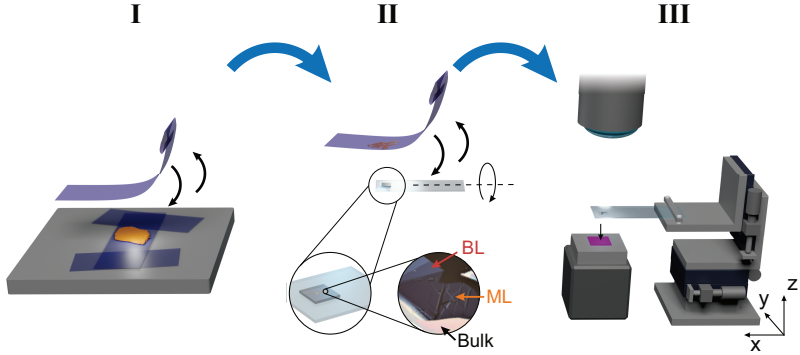
Figure 4.1 | Fabrication of the heterostructures. Thin flakes of the material are exfoliated with Nitto tape from a bulk single crystal (**I**, orange) and placed on a viscoelastic poly-dimethyl-siloxane (PDMS) film (**II**). After gently lifting the tape, single monolayers of the TMDC are left on the PDMS and are pre-characterized using an optical microscope. Thereby, monolayer (ML), bilayer (BL) and bulk regions can be distinguished by the optical contrast. Afterwards, the monolayer is stamped onto a silicon wafer covered by a 300-nm-thick thermal oxide layer using a 3D micro-positioning stage (**III**). By repeating the procedure single monolayers can be stacked to form a heterostructure.

with high optical contrast due to thin-film interference. This step is repeated until a monolayer with the intended size and quality is exfoliated. In the last step (III), the PDMS with the monolayer is aligned above the desired substrate, in our case a silicon substrate covered by a 300-nm-thick thermal oxide layer (SiO_2) and stamped onto the surface using a three-dimensional micro-positioning stage. Repeating this process, carefully aligning subsequent monolayers to the already transferred one with the micro-positioning stage, a heterostructure is produced.

The fabrication of a WSe_2 on WS_2 (WSe_2/WS_2) heterostructure is shown in Figure 4.2. Thereby, the notation will always list the layers from top to bottom, here a WSe_2 monolayer on top of a WS_2 monolayer. We start out with a WS_2 monolayer (optical microscopy image in Figure 4.1, II) and a WSe_2 monolayer (Figure 4.2a). The WSe_2 monolayer (orange) has an adjacent bilayer (blue) and bulk residues in
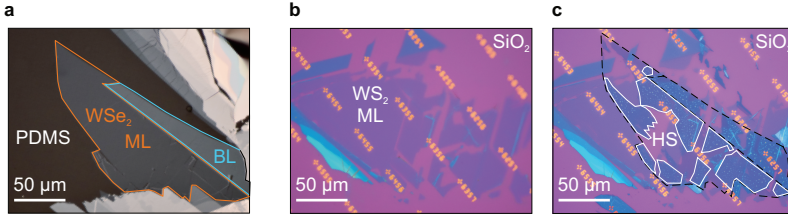
Figure 4.2 | Optical characterization of the WSe$_2$ and WS$_2$ monolayers, and the WSe$_2$/WS$_2$ heterostructure. a, Optical microscope image of exfoliated monolayer of WSe$_2$ on a PDMS film. WSe$_2$ monolayer (ML, orange) and bilayer (BL, blue) as well as bulk regions can be easily distinguished in the optical image due to thin-film interference. **b,** Optical image of the WS$_2$ flake from Figure 4.1 stamped onto the substrate (SiO$_2$). The gold markers are spaced by 50 μm and facilitate the positioning during measurements. **c,** The heterostructure produced from the WS$_2$ monolayer (**b**) and the WSe$_2$ monolayer (from **a** indicated by the dashed black line) is shown. Well contacted heterostructure regions are visible (white framed areas, HS), featuring the typical flat areas with darker color and inclusions due to clustered particles between the layers.

its vicinity (top right and bottom). Even the difference between mono- and bilayer is clearly visible, allowing for easy identification of monolayer regions in the optical image. The WS$_2$ monolayer is stamped onto the SiO$_2$ (Figure 4.2b) showing a large homogeneous area on the left and smaller regions on the right. After stamping the WSe$_2$ on top (Figure 4.2c, dashed outline), we obtain a large heterostructure area (white frame), featuring regions slightly darker than the monolayer including small bumps due to particles in between the layers. These emerge in the annealing process, where the sample is heated to 150 °C in high vacuum for two hours, to remove residue of the transfer procedure on the surface. Additionally, the contact between the layers is increased due to the fact that particles between the layers cluster together, forming small inclusions surrounded by flat and well contacted monolayers [Hon14, Yu15]. This fabrication process allows for easy production of heterostructures with tens or even hundreds of micrometers in size [Mer19]. While these large area samples are practical to perform optical measurements employing visible, near-infrared or even mid-infrared radiation, conventional THz time-domain spectroscopy requires yet larger samples and inevitably averages over large areas of the TMDC

heterostructure. Therefore, THz nanoscopy is crucial to investigate these materials in the THz spectral range. In the following, the local conductivity of representative TMDC heterostructures will be investigated.

Performing THz time-domain spectroscopy on the sample allows us to obtain its frequency dependent polarization response to light and provides access to the local conductivity of the heterostructure. We focus THz probe pulses onto the tip-sample system, depicted in Figure 4.3a. The electromagnetic interaction with the tip and sample leads to a scattered THz waveform encoding the local electronic and optical properties. An optical microscope image of the investigated area on another heterostructure is shown in Figure 4.3b. We investigate the transition from the WS_2 monolayer region (black frame, left) to the WSe_2/WS_2 heterostructure (black frame,
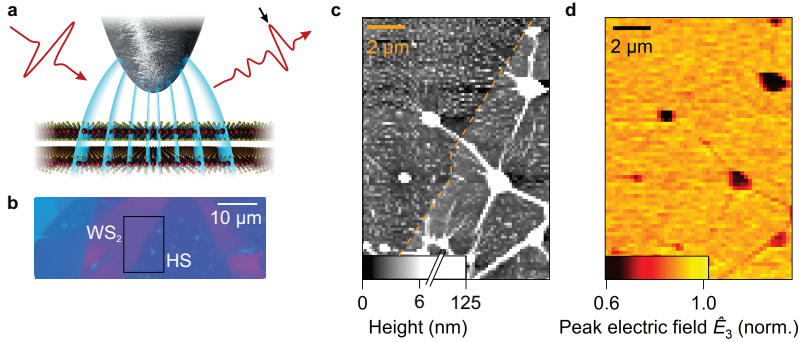
Figure 4.3 | Steady-state THz nanoscopy of a WSe_2/WS_2 heterostructure. **a,** Schematic of the experiment. A THz pulse is focused onto the tip-sample system. After the interaction, the modified THz waveform is recorded by field-resolved detection. The black arrow indicates the peak electric field that is mapped in **d**. **b,** Optical image of the investigated area. The black frame indicates the region imaged in **c** and **d**. **c,** Atomic-force microscopy (AFM) map of a region containing a monolayer (left) and the heterostructure (right) separated by a step on the order of 1 nm (dashed line). To visualize the small step compared to the height of the inclusions of $\sim 10 - 100$ nm, the color scale is oversaturated. **d,** Map of the scattered peak electric field $\hat{E}_3$ (arrow in **a**) on the same area, showing no visible difference between monolayer and heterostructure region. The inclusions and folds are prominent features with a strongly reduced signal.

right). During the near-field measurement, the height profile and scattered near-field signal are obtained simultaneously. In Figure 4.3c, the nanoscale topography of the sample is displayed. The monolayer (left) consists of a mostly flat area featuring the typical single nm-scale surface roughness and only few larger inclusions, most likely caused by particles on the substrate before stamping. The heterostructure (right) shows flat areas separated by more topographic irregularities like inclusions and folds ($\sim 10 - 100$ nm in height) originating from particles on the substrate and PDMS residue on the WS_2 monolayer stemming from the stamping process. The step edge between monolayer and heterostructure is visible in the center (dashed line). Note that in order to visualize the 1-nm-high step edge, the colorscale is over-saturated. To investigate the scattered near-field signal, the peak electric field $\hat{E}_3$ (black arrow in Figure 4.3a) of the third-harmonic of the tip oscillation frequency is plotted in a two-dimensional false-color map as a function of the position on the sample. The notation $\hat{E}_i$ refers always to the peak electric field of the full wave-form E_i. Clear correlations between the topography and the scattered electric field are observed. The folds and inclusions exhibit only weak scattering signals, while flat regions of the heterostructure and the monolayer show a much stronger scatter-ing response. The monolayer and heterostructure cannot be distinguished by their scattering efficiency indicating a very similar conductivity for our probe spectrum.

In contrast, some heterostructures show a drastically different behavior. The WSe_2/$MoSe_2$ heterostructure depicted in Figure 4.4a was fabricated in the same way, dis-playing a large overlap area in the center. When performing the near-field experi-ment in the region marked by the white frame, we find the typical surface structure in the AFM scan (Figure 4.4b). Four areas can be identified: the substrate on the top (SiO_2), the monolayer regions left (WSe_2) and right ($MoSe_2$) and the heterostruc-ture on the bottom (HS). There seem to be more topographic irregularities on the monolayers and the heterostructure compared to the other sample (Figure 4.3b), most likely originating from a less fortunate transfer process. Most importantly, when looking at the peak electric field $\hat{E}_2$ of the second order scattered near-field signal (Figure 4.4c), we observe a clear contrast between the heterostructure and monolayer or substrate regions. The scan shows a higher overall scattered signal on the heterostructure, while the monolayers and substrate exhibit only minute differ-
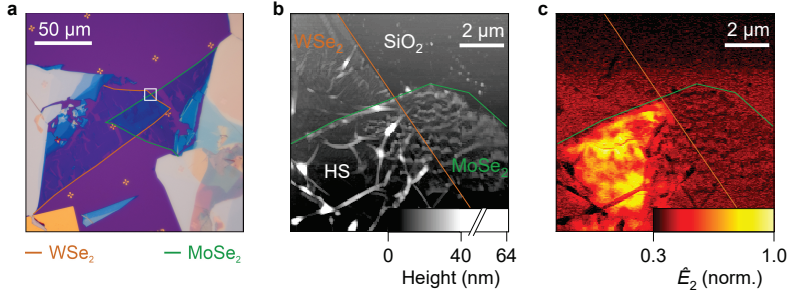
Figure 4.4 | Steady-state THz nanoscopy of a WSe$_2$/MoSe$_2$ heterostructure. a, Optical microscopy image of a WSe$_2$/MoSe$_2$ heterostructure. The orange and green lines mark the constituent monolayers. The white square shows the scan area for the AFM and near-field measurements. **b,** AFM false-color plot of an area featuring substrate (SiO$_2$), WSe$_2$ (orange) and MoSe$_2$ (green) monolayer as well as WSe$_2$/MoSe$_2$ heterostructure (HS). **c,** THz nanoscopy map showing the peak electric field $\hat{E}_2$ of the second demodulation order of the same region featuring a clear contrast between substrate or monolayers and the heterostructure most likely caused by doping during the fabrication procedure. The heterostructure features darker and brighter regions. Note that the signal on the uppermost horizontal lines of the scan increases suddenly most likely caused by the tip deforming on a surface impurity. Since the scan is recorded in horizontal lines from top to bottom, it has no effect on the data recorded on the heterostructure.

ences. This shows a completely different behavior compared to the heterostructure before, where not even the third demodulation order $\hat{E}_3$, which is more surface sensitive, could resolve any difference between monolayer and heterostructure areas. We attribute the high scattering signal of the heterostructure to local doping increasing the optical conductivity. The doping is most likely induced during the annealing process [Bau13, McD14] at the end of the fabrication procedure. While similar effects could originate from an already doped bulk crystal, this can be excluded since we observe no increased signal on the isolated monolayers. In addition, significant differences of the local conductivity are observed within the heterostructure, showing especially high doping at the folds within the investigated area. Therefore, our new experiment allows us to identify local changes in the dielectric function on nanoscale areas, six orders of magnitude smaller than diffraction limited THz spot sizes.
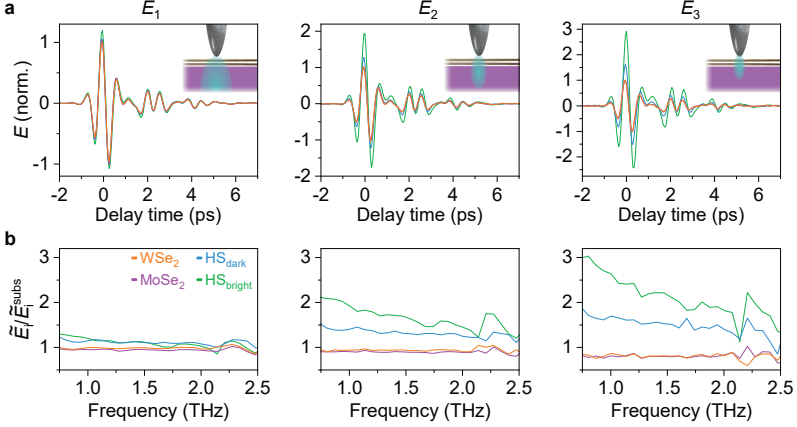
Figure 4.5 | THz time domain spectroscopy of the WSe$_2$ and MoSe$_2$ mono-layers and the WSe$_2$/MoSe$_2$ heterostructure. a, Field-resolved near-field THz waveform (E_1, E_2, E_3) taken on the monolayer and heterostructure areas for first, second and third demodulation order. The electric field strength is normalized to the peak electric field amplitude recorded on the substrate. The inset indicates the reduction of the probing volume (cyan) for higher demodulation orders, increasing in surface sensitivity and leading to larger relative contributions of the atomically thin layers to the signal compared to the substrate (purple). **b,** The differential spectra, which are obtained by dividing the recorded spectra $\tilde{E}_1, \tilde{E}_2, \tilde{E}_3$ by the spectral response of the substrate ($\tilde{E}_i^{\text{subs}}$), are shown. The frequency window is chosen to avoid low signal-to-noise ratios at the edges of our detection bandwidth. Higher demodulation orders show stronger differences due to increased near-field confinement and surface sensitivity.

Until now, mainly the peak electric field was investigated, which is a measure of the local conductivity and directly reflects the spectrally integrated response of the sample if the system exhibits no clear resonance within the probe spectrum [Ste17b]. To understand the origin of the observed contrast, we investigate the frequency dependent light-matter interaction. By recording full THz waveforms and using the Fourier transform, we obtain the spectral response of the system. To this end, we record full traces on the substrate, the WSe$_2$ and MoSe$_2$ monolayers and on different areas of the heterostructure (dark/bright). As a result, we can plot the THz

transients for the first, second and third harmonic of the tip oscillation frequency (Figure 4.5a, E_1, E_2, E_3). For all orders, we observe a THz waveform followed by a reflection at $2\,\mathrm{ps}$ and $4\,\mathrm{ps}$. From first to third demodulation order, the difference of the detected electric field strength between the monolayers and heterostructure increases, while mostly preserving the shape of the waveform. To remove the effect of the probe spectrum and the tip-sample interaction, we normalize the measured spectra using the signal recorded on the SiO_2 substrate ($\tilde{E}_i^{\mathrm{subs}}$) accessing in a first approximation the pure frequency dependent sample response. The resulting spectra (Figure 4.5b) show a broadband response, hosting no sharp features, which is expected since increased doping should manifest in an overall broadband increase in reflectivity and hence, scattering signal. Generally, lower frequencies are more enhanced on the heterostructure compared to higher frequencies. With higher demodulation order, we also find an increase of the differences in the normalized spectra between the monolayers and the heterostructure. This is explained by the stronger field confinement and increased surface sensitivity of higher demodulation orders (Figure 4.5a, inset) [Eis14, Gov14, Moo20] resulting in a larger contribution of the atomically thin sample compared to the SiO_2 substrate to the overall scattered radiation.

It has to be pointed out that the fabricated samples rarely showed similar doping effects and typically feature a uniform scattering response. In summary, steady-state measurements are a key tool to pre-characterize the samples and avoid irregular doping effects influencing the dielectric function or carrier dynamics. In this section, the sample fabrication, pre-characterization and steady-state behavior was introduced. In particular, THz nanoscopy allows us to investigate these typically rather small samples in the first place and even resolves nanoscale inhomogeneities providing a valuable tool to investigate the native properties and behavior of heterostructures in a non-averaged manner. In the following, we take the experiment a step further, not only accessing the steady-state properties, but focus on the interlayer charge transfer, and investigate the electron-hole pair tunneling dynamics using THz emission nanoscopy.

4.2. Characteristic fingerprint of the interlayer tunneling

To directly access the out-of-plane interlayer charge transfer in the WSe_2/WS_2 heterostructure focusing on the motion of the carriers between the layers, we employ laser THz emission nanoscopy (Figure 4.6a), also called LTEN [Kla17, Yao19, Piz20]. When photoexciting electron-hole pairs in a heterostructure with type-II band alignment (Figure 4.6b), electrons and holes favor to reside in different layers. Therefore, negative charges in the WSe_2 and positive charges in the WS_2 tunnel into their adjacent layer shortly after photoexcitation (Figure 4.6b, right), leading to a current pointing towards the WSe_2 monolayer. The ultrafast time-dependent out-of-plane current leads to a time-dependent dipole moment causing the emission of an electromagnetic wave [Ma19]. Using a sharp metallic tip (Figure 4.6a), we can directly couple to the out-of-plane dipole moment and facilitate the emission into the far field. By employing field-resolved detection, we record the emission transient (red waveform) and gain insight into the charge transfer process with nanoscale precision.
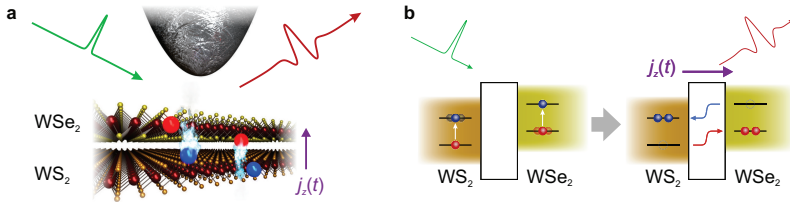
Figure 4.6 | THz emission nanoscopy. a, A schematic of the emission experiment is shown. The near-field probe is approached to the sample and electron-hole pairs are photoexcited by the pump pulse (green). The time-dependent interlayer tunneling current leads to a time-dependent dipole moment. Using a sharp metallic tip, we can directly couple to the out-of-plane dipole moment facilitating the emission process and allowing for field-resolved detection of the emitted waveform with nanoscale resolution. **b,** Type-II band alignment of the WSe_2/WS_2 heterostructure. After photoexcitation (green pulse, left), electrons energetically favor WS_2, and holes the WSe_2 layer, and tunnel accordingly. The ultrafast time-dependent out-of-plane current leads to the emission of an electromagnetic wave.

4.2.1. Recording THz emission waveforms

In the experiment, we replace the THz probe pulse by an ultrashort pump pulse with a pulse duration of 140 fs and a center wavelength of 515 nm, which is enough photon energy to overcome the bandgap in WSe$_2$ (bandgap: ~ 730 nm, ~ 1.7 eV) and WS$_2$ (bandgap: $\sim 590 - 620$ nm, $\sim 2.0 - 2.1$ eV) [Low17]. Due to the type-II band alignment, an interlayer current emerges pointing towards the WSe$_2$ monolayer (Figure 4.6a). The time-dependent out-of-plane current leads to a dipole moment that couples to the near-field probe and emits into the far field, where we use EOS employing a 4-mm-thick GaP crystal to record the emitted waveform. To put the magnitude of the signal into perspective, one should consider that the emitted waveform is generated in a volume that is given by the height of the heterostructure of roughly 1 nm and the spatial resolution of our tip, which is typically similar to its radius of curvature of 40 nm. The probing volume of 40 nm×40 nm×1 nm is therefore 12 orders of magnitude smaller than what the diffraction limit allows for THz frequencies. Hence, excellent sensitivity is required to resolve the emitted radiation.

Nevertheless, we record a clear single cycle emission waveform (Figure 4.7, blue) on a WSe$_2$/WS$_2$ heterostructure. The symbols show the measured data, and the line represents a running average over 3 data points. The polarity of the detected waveform is referenced to the emission peak field of an indium arsenide (InAs) sample, where highly mobile electrons diffuse into the bulk material faster than the holes, leading to an effective net current towards the surface, the so called photo-Dember effect [Joh02, Kla17, Ma19]. Due to the bulk nature of this effect, InAs is an ideal reference sample providing at least one order of magnitude larger signals compared to the atomically thin TMDC samples. On the WSe$_2$/WS$_2$ heterostructure, we find the same field polarity, thus the same direction of the current from WS$_2$ to WSe$_2$, exactly what the type-II band alignment predicts. No emission is found on the substrate (gray) or monolayers. To corroborate that the emission signal is exclusively caused by the interlayer charge transfer, the emission experiment is performed on a heterostructure fabricated with an inverted stacking order. We observe the emission with negative peak field polarity (red) featuring the same shape and spectral amplitude (inset). The inverted field polarity originates from an inverse current direction and unambiguously verifies the interlayer charge transfer as the origin of the emitted waveforms.
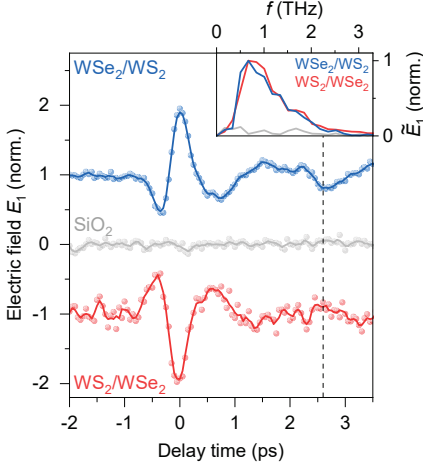
Figure 4.7 | Field-resolved THz emission nanoscopy. Recorded THz emission of a WSe_2/WS_2 heterostructure (blue symbols), the substrate (gray symbols) and an inverted, WS_2/WSe_2 heterostructure (red symbols). The colored lines represent the respective running average over 3 data points. The inset shows the spectral amplitude of the smoothed THz emission waveforms. The dashed line indicates an echo of the emission signal after 2.6 ps.

Furthermore, we can estimate the number of charge carriers that are involved in the emission process. Due to the high spatial resolution, only the peak pump fluence in the center of the photoexcitation spot is probed, which in our case is $30\,\mu J/cm^2$. Even though the typical absorption of the monolayers on SiO_2 is $\sim 6-7\,\%$ [Li14], thin-film interference with the 300-nm-thick SiO_2 layer can increase this value up to $\sim 30\,\%$ [Ans18]. Therefore, we find an upper limit of the photo-induced charge carrier density of $2.3 \times 10^{13}\,cm^{-2}$ in the monolayers. Due to the spatial resolution given by the tip radius of 40 nm and a carrier tunneling efficiency of 70 % [Ma19], we estimate that fewer than 1000 carriers per monolayer moving less than 1 nm lead to the detected emission waveform.

In order to verify the nanoscale origin of the THz emission experimentally, we go back to the region investigated in Figure 4.3. We raster scan over the monolayer-heterostructure step marked by the orange frame (Figure 4.8a), while recording the peak electric field $\hat{E}_1$ of the emission transient modulated at the tip oscillation frequency. The step edge in the center of the AFM image can be identified (Figure 4.8b). More importantly, strong contrast is observed in the emission signal (Figure 4.8c). No emitted field is expected or measured on the monolayer (left), while a uniform emission signal is detected on the heterostructure (right). A slight
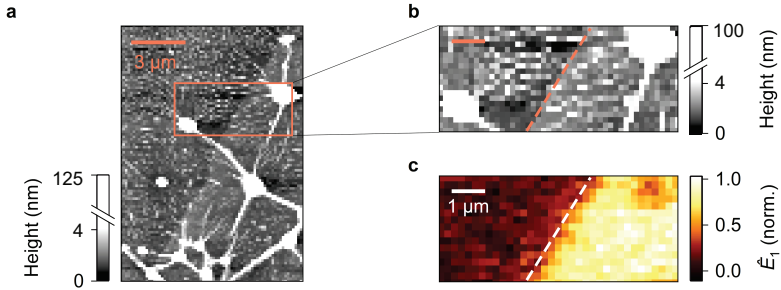
Figure 4.8 | Nanoscale origin of the THz emission. a, AFM overview scan of the region from Figure 4.3. **b,** Magnified AFM map of the step edge between monolayer (left) and heterostructure (right). **c,** Spatially resolved peak electric field $\hat{E}_1$ of the emission waveform showing a clear contrast between monolayer and heterostructure.

shift to the right is observed for the near-field emission signal compared to the step edge (dashed lines), which is attributed to the long integration time in combination with the scan direction from left to right leading to a delayed rise of the signal. Additionally, we cannot exclude artifacts at the edges of the top monolayers changing its physical integrity and the quality of the contact between the layers, hence blurring the theoretically expected step-like emission signal. We also observe a clear reduction of the signal at the inclusion on the top right corner, verifying the assumption that particles between the layers reduce the interlayer tunneling.

In summary, we are now able to record the characteristic fingerprint of the interlayer tunneling process in atomically thin heterostructures with subcycle temporal resolution and spatial precision orders of magnitude below the diffraction limit.

4.2.2. Modeling the interlayer tunneling

To deepen our understanding of the tunneling process, we model the interlayer current and emission waveform in a quantitative manner. While the experimental parameters like pump pulse and detector response are clear, the exact effect of the tip-sample interaction on the detected waveform is unknown. As summarized in

Section 3.1., the exact description of the tip-sample interaction is non-trivial and depends on the probe geometry influencing coupling strength and field confinement. Especially in the THz regime the realistic experimental setup needs to be included as detailed as possible, since the tip and cantilever dimensions are similar to the wavelength ($\sim 100 \, \mu$m), which significantly influences the light-matter interaction. Therefore, we model the emission process fully numerically [Moo21] to obtain the influence of the near-field probe, before extracting the interlayer current.

Simulation of the tip-sample interaction

In the experiment (Section 3.2.), the near-field tip is mounted to the probe holder on the AFM head (Figure 4.9a, red circle). When the microscope is approached to the sample surface, only the near-field probe, consisting of a ceramic chip, cantilever and tip, is close to the sample. Scanning electron microscopy images of the commercial near-field probes are shown in Figure 4.9b. The tip and cantilever are made of solid platinum iridium. While we find only slight differences in tip length for different probes, the tip shape features more variations (inset).

To simulate the emission process, a commercial finite element method (FEM) software (COMSOL Multiphysics) is used, allowing us to numerically solve Maxwell's equations for arbitrary geometries. A spherical simulation volume with a diameter of 1.2 mm was chosen to accommodate the long wavelengths in the THz spectral range. In addition to these macroscopic dimensions, the resolution needs to be fine enough to accurately capture the nanoscale confinement of the electric field at the tip apex, which renders these realistic simulations of THz nanoscopy computationally demanding. In contrast to the mid-infrared spectral range, where the tip is often reduced to a simple sphere representing the apex, we need to include the tip shaft and cantilever to capture possible antenna resonances that can strongly influence the interaction. Despite the challenge of including a large simulation volume while maintaining nanoscale resolution at the tip apex, we implement the full near-field probe geometry with a fine mesh with up to one million individual elements. Using scanning electron microscopy (Figure 4.9b), realistic tip, shaft and cantilever dimensions of representative probes are extracted, which are similar to the specifications of the supplier (25PtIr200B-H40 by Rocky Mountain Nanotechnology LLC, radius
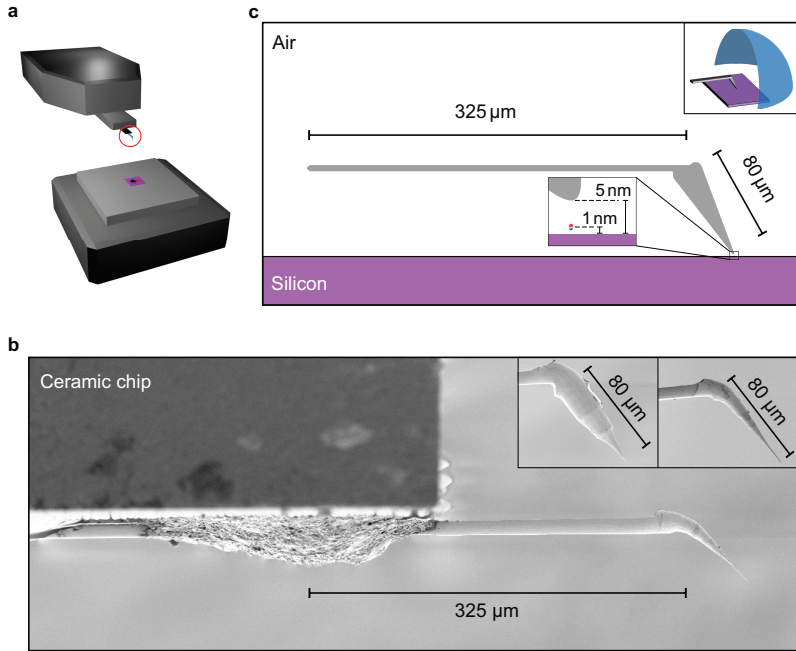
Figure 4.9 | Finite element method (FEM) simulation geometry to model the near-field interaction. a, Schematic of the near-field microscope layout consisting of an AFM-head (top) and the sample positioning table (bottom). The AFM probes are glued to the chip holder on the AFM head (red circle). **b,** Scanning electron microscopy (SEM) images of the AFM probes. A mm-scale ceramic chip (top left) holds the tip in place, allowing for quick tip replacements and ease to use. The probe is made of solid platin iridium forming a cantilever and tip at the end. The cantilever length and exact tip shape may vary (see inset). **c,** Geometry of the tip in the FEM simulations. The complicated interface of the cantilever and the ceramic chip is simplified to a cantilever with an effective length of 325 µm. The tip is modeled by a 80 µm-long tip shaft and the sample is reduced to a silicon-air interface. The emitting point-dipole is placed below the tip 1 nm above the substrate (red circle). Top inset: The emitted radiation is collected in a quarter of the full solid angle represented by the blue dome in front of the tip.

of curvature $< 40\,\text{nm}$). In particular, the tip is modeled with a conical shaft with a length of $\sim 80\,\mu\text{m}$ (Figure 4.9c) and a radius of curvature of $40\,\text{nm}$ at the apex. To simplify the complex geometry at the end of the cantilever, where it is mounted to the support chip, we employ an effective cantilever length of $325\,\mu\text{m}$. The dielectric function of the metallic tip and cantilever is implemented by a Drude model using the parameters for platinum [Rak98]. The lower half space of the simulation is set to the dielectric constant of a silicon substrate ($\epsilon_1^{\text{Si}} = 11.7$, [Zha12]), where we neglect the influence of the thin SiO_2 cover layer and the heterostructure. The upper half space is air with $\epsilon_1^{\text{air}} = 1$. Perfectly matched layers surround the simulation volume on all sides and dampen the outgoing radiation. Thereby, reflections from the boundaries, which typically lead to artifacts in the simulation results, are avoided. The tip-sample distance describing the separation of the lowest point of the tip apex and the surface is set to $5\,\text{nm}$. We implement the emission due to the interlayer tunneling by a point-dipole placed $1\,\text{nm}$ above the surface at the center of the simulation volume (Figure 4.9c, inset bottom). The field distribution in the simulation volume is calculated for frequencies up to $3\,\text{THz}$ in steps of $0.1\,\text{THz}$ emitted by the point dipole.

As a result, the complex-valued field distribution of each frequency within the simulation volume is obtained. We superimpose the calculated frequency-domain field amplitude according to the spectral weight set by the ultrafast temporal evolution of the interlayer tunneling[1] and additionally account for the detector response of the EOS (see Section 3.2.3.). In the end, a time-domain movie of the emission process is computed by systematically evolving the phase of the complex-valued electric field for each frequency component (Figure 4.10).

For the bare emission process (Figure 4.10a), we observe a clear symmetric wavefront emitting from the point-dipole after $1\,\text{ps}$. Negligible emission in the out-of-plane direction like expected from a vertically oriented dipole emitter is found. Nevertheless, strong electric fields along the dipole axis are observed in the near-field and exploited in the experiment, using the near-field tip to locally enhance the vertical electrical fields. The tip-assisted emission in Figure 4.10b shows a similar wavefront, however, the presence of the tip increases the field strength and out-coupling of the

---

[1]The tunneling time is determined in the last part of this section (Figure 4.13).
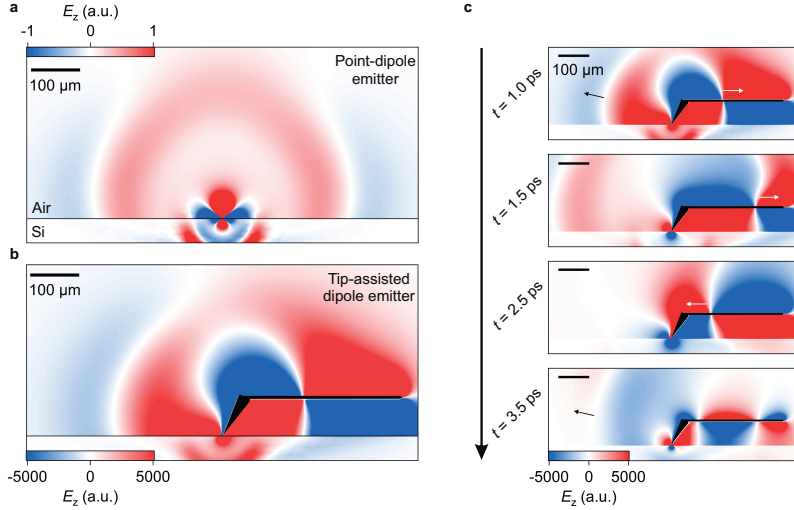
Figure 4.10 | Snapshots of the bare and tip-assisted THz emission.
a and **b,** Snapshots of the THz emitted by the point dipole after 1 ps. The field distributions obtained by the FEM simulation are superimposed and weighted by the emission spectrum obtained from the theoretical prediction. **c,** Image series of the tip assisted emission capturing the strongly modified field distribution. Additionally, a second emission wavefront can be seen after 3.5 ps (black arrow bottom) that is also observed in the experiment originating from the electromagnetic wave coupling to the tip and cantilever. The mode travels along the cantilever (white arrow), gets reflected at the end and is reemitted at the tip apex.

dipole by more than a factor of 5000. This drastic enhancement is crucial for the experiment, since without it, detection of the THz emission originating from the interlayer tunneling within the nanoscale probing volume would be virtually impossible. In addition, we observe a strong coupling of the electric field to the tip shaft and cantilever leading to a very asymmetric field distribution and a slightly delayed wavefront in the tip-assisted case. Interestingly, a second emission wavefront occurs at later times. When following the time evolution after 1 ps and focusing on the right part of the simulation, a wavefront is moving along the cantilever (Fig-

ure 4.10c, white arrow). It is reflected at the end of the cantilever and travels towards the tip shaft ($t = 2.5\,\text{ps}$). When reaching the tip apex it gets reemitted leading to an echo of the original emission at $t = 3.5\,\text{ps}$. We directly identify the echo due to the propagation along the tip shaft and cantilever as the reflection observed in the emission waveform in Figure 4.7, which is very prominent in the top waveform and also $\sim 2.6\,\text{ps}$ delayed relative to the first emission peak. By avoiding significant approximations in modeling the realistic geometry in the experiment numerically, this reflection is captured in the simulation and provides detailed understanding of the experimentally observed signatures.

The radiated far fields are calculated by employing the Stratton-Chu formalism [Str39] for the volume surrounding the dipole emitter (implemented in COMSOL Multiphysics as far-field domain option). As a result, the electric far fields E_z^{far} can be integrated over the outer spherical surface of the simulation volume. Thereby, we mimic the geometry of the parabolic mirror in the experiment by including only the radiation integrated over a spherical segment that corresponds to a quarter of the full solid angle and does not contain the cantilever or the sample (see blue region in Figure 4.9c, inset, top right). In addition, only vertically polarized electric fields are analyzed, since the EOS detection scheme is sensitive to vertical polarization only. By comparing the emitted far fields in the presence of the tip $E_z^{(\text{far,tip})}$ with the ones emitted by the bare dipole $E_z^{(\text{far,bare})}$, the entire tip scattering response is captured in a complex-valued transfer function $\Omega^{\text{transfer}} = E_z^{(\text{far,tip})}/E_z^{(\text{far,bare})}$ (Figure 4.11, red). The spectral amplitude follows a $1/f$ trend (Figure 4.11a, gray), which was observed before [Wan04]. However, it features additional structure, specifically, periodic minima of the amplitude caused by the reflection after $t = 3.5\,\text{ps}$. The phase of Ω^{transfer} (Figure 4.11b) shows slight oscillations and an overall linear slope, which corresponds to a delay of the emitted radiation when interacting with the tip compared to the bare emitter case.

Complementarily, we also perform a reference experiment to verify the theoretical transfer function. To this end, we detect the THz waveform emitted from a photoexcited InAs surface caused by the photo-Dember effect with and without a scanning probe tip, while maintaining all other experimental parameters, especially

the total beam path and focus of the pump beam. The resulting complex transfer function is shown in blue in Figure 4.11. We find good agreement in the shape of the spectral amplitude of the transfer function even matching the periodic local minima (Figure 4.11a, blue). The slight variations in periodicity are most likely caused by varying cantilever lengths in the experiment or the simplification in the simulation, where the cantilever is mounted to the ceramic chip. For low and high frequencies stronger deviations between experiment and simulation are observed, which are caused by our limited detection bandwidth. The phase of the transfer function (Figure 4.11b, blue) is similar to the simulation, but had to be modified by a linear slope, corresponding to an additional delay between tip-assisted and bare emission. This shift in time was already observed before [Kla17] and is caused most likely by the finite size of the pump spot and the bulk character of the photo-Dember effect, which is only confined to the surface in the tip-assisted case, leading to different centers of emission with and without the tip, thus a significant difference in beam path. In
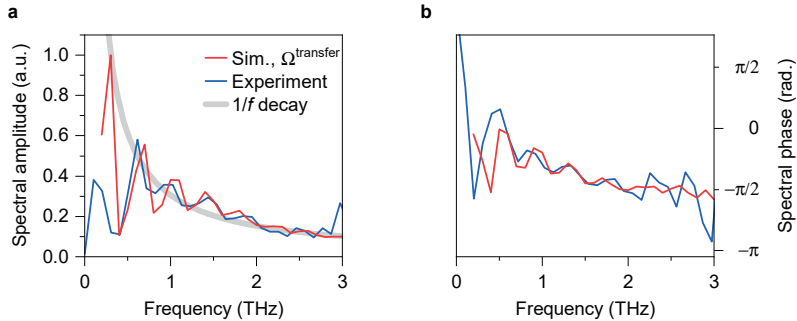
Figure 4.11 | Tip-sample interaction transfer function. a, The spectral amplitude of the transfer functions of the FEM simulation (red line) and the reference experiment on InAs (blue line) are shown. Both follow a $1/f$-behavior (gray line), but exhibit additional structure due to the echo in the simulation and the measurement. Since the probing volume of near and far field differ and the shape of the transfer function is more important than its absolute value, the transfer function recorded on InAs is scaled vertically. **b,** Spectral phase of the transfer functions showing good agreement for the main part and increasing deviations at the edges of the experimental detector bandwidth.

contrast, the emitting dipole is fixed at the surface for both cases in the simulation. Deviations between simulation and experiment are noticeable above 2.5 THz due to the reduced signal-to-noise ratio at the higher edge of our detector bandwidth. In summary, the experimental and theoretical tip transfer function reveal two dominant contributions: a $1/f$ low-pass filtering and an echo of the main emission transient leading to the periodic structure in the retrieved transfer functions.

Modeling the interlayer tunneling and emission process

With the additional knowledge about the tip-sample transfer function, it is now possible to theoretically describe the emission experiment. To do so, we adapt the three-state model from Ma *et al.* [Ma19], where two main processes are expected to determine the interlayer current: intralayer relaxation and interlayer tunneling. After the nonresonant photoexcitation at 2.4 eV, the hot electron-hole pairs most efficiently tunnel at the points of intersection of intra- and interlayer electron-hole pair dispersion relations, due to energy and momentum conservation [Mer19]. This process is accounted for by an additional term with the rate $1/\tau_{\mathrm{relax}}$ delaying the efficient tunneling into the adjacent layer at a rate of $1/\tau_{\mathrm{tunnel}}$ and lead to the time dependent out-of-plane tunnel current $j_z(t)$. The current is described by:

$$j_z(t) = \frac{1}{\tau_{\mathrm{tunnel}} - \tau_{\mathrm{relax}}} (e^{-t/\tau_{\mathrm{tunnel}}} - e^{-t/\tau_{\mathrm{relax}}}) \qquad (4.1)$$

We found the best agreement with our experiment for assuming $\tau_{\mathrm{tunnel}} \approx \tau_{\mathrm{relax}} \equiv \tau$, which can be simplified using L'Hôpital's rule to

$$j_z(t) = \frac{t}{\tau^2} e^{-t/\tau} \qquad (4.2)$$

described by only one parameter τ with a characteristic duration of $\sim 2\tau$, capturing the effects of relaxation and tunneling, since they cannot be distinguished in this experiment. To simulate the emitted waveform a few intermediate steps are necessary (Figure 4.12). First, to account for the finite pulse duration, the theoretical interlayer current is convoluted with a Gaussian function with a full width at half maximum of 140 fs (Figure 4.12a). The difference for typical tunneling times τ in
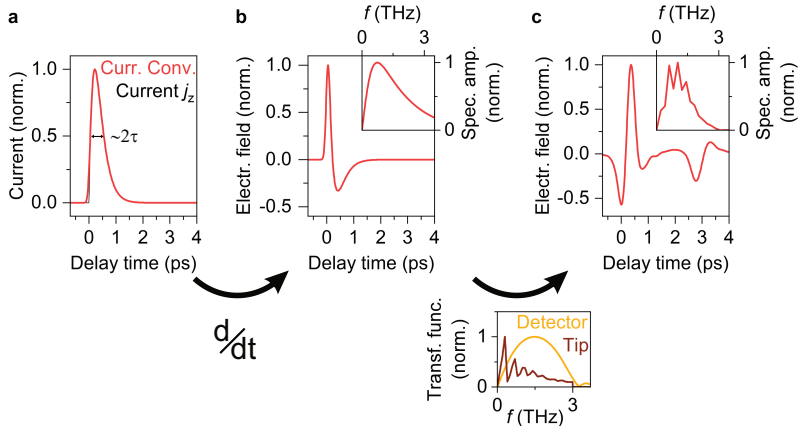
Figure 4.12 | Modeling of the emission waveform. a, Time-dependent current featuring a sharp onset due to photoexcitation and an exponential tail due to relaxation of the hot carriers and interlayer tunneling. **b,** Emitted-electric field determined by the time derivative of the current. The corresponding spectral amplitude is shown in the inset. **c,** Predicted experimentally observed waveform by taking detector and tip response function into account. The corresponding spectrum is shown in the inset. The arrows indicate the operation to obtain **b** and **c**.

our experiment is only noticeable at the otherwise infinitely fast onset of the bare current (black, 0 ps) compared to the convoluted one (red). To obtain the emitted waveform, we use Maxwell's equations. Whereas the electric near-field is proportional to the current, the emitted radiation in the far field corresponds to the time derivative of the current [Sha04] (Figure 4.12b). The complex-valued spectrum is accessed by performing the Fourier transform (inset). In the frequency domain, we account for our detector response (Detector) and the influence of the simulated tip transfer function (Tip). In the end, we compute the inverse Fourier transform of the resulting spectrum (Figure 4.12c, inset) and obtain the emitted waveform (Figure 4.12c), which depends only on the parameter τ.

Fitting our experimental results by varying τ and comparing theoretical and experimentally retrieved emission waveform (Figure 4.13), we find best agreement for
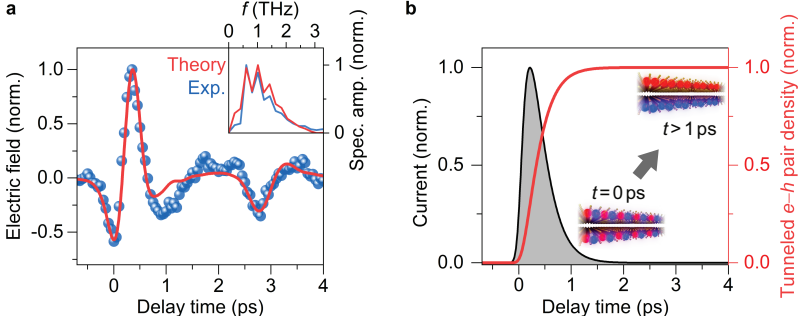
Figure 4.13 | Extracting the interlayer current from the experimental waveforms. a, Recorded waveform E_1 (blue spheres) and fit (red line) in the time and frequency domain (inset) are depicted. **b,** Corresponding current (black line) and tunneled electron-hole (e–h) pair density obtained by numerical integration (red line) are shown. The inset indicates the initial state ($t = 0$ ps) after photoexcitation and the charge separation after the interlayer tunneling ($t > 1$ ps).

$\tau = 200$ fs, which is compatible with spatially averaged results [Hon14, Mer19, Ma19, Wan21]. We plot the experimental data points (Figure 4.13a, blue spheres) and the modeled emission (red line). Overall, the theory reproduces the experiment very well, capturing the first single cycle oscillation and the reflection ~ 2.5 ps after the peak electric field. The only significant deviation is found after the main peak and could be caused by an additional reflection that is not captured in the FEM simulation, for example, originating from sharp edges at the bend between tip and shaft of the near-field probes in the experiment. Similarly, the experimental spectrum is well reproduced (Figure 4.13a, inset). The theory only overestimates the low frequency components smaller than 0.5 THz as seen in the comparison of the theoretical and the experimental transfer function.

The interlayer current is extracted (Figure 4.13b, black) and by numerical integration we obtain the tunneled electron-hole pair density depending on time after photoexcitation (red). The resulting step-like function shows that almost all carriers have separated within 1 ps after photoexcitation (inset).

71

In this section, THz emission nanoscopy has proven itself to be a valuable tool to investigate the interlayer tunneling in TMDC heterostructures on the nanoscale. The recorded characteristic fingerprint of the charge carriers tunneling between the atomically thin layers provides insight into the quality of contact between the layers as a measure of the tunneling efficiency. By understanding the influence of the tip in the vicinity of the emitting surface, even a quantitative understanding of the tunneling process is possible, extracting a characteristic tunneling time of 200 fs.

Chapter 5

Subcycle polarization nanoscopy of ultrafast interlayer dynamics

Even though THz emission nanoscopy can be used to quantitatively investigate the interlayer tunneling on the nanoscale, it is fundamentally limited by the inefficient spontaneous emission of photons due to charge carrier acceleration and insensitive to interlayer carrier dynamics after the charge separation. In the following, a novel concept is introduced, focusing on the polarizability of the photogenerated electron-hole pairs, strongly up-scaling the signal-to-noise ra-

Figure 5.1 | Intra- and interlayer electron-hole pair polarizability. Steady-state (rims) and by E_{THz} deflected carrier positions (spheres) are depicted.

tio. This approach builds on the critical change of the polarizability of electron-hole pairs during the interlayer tunneling. To probe this change, ultrafast THz pulses can be used to apply an instantaneous electric field on the sample. Electron-hole pairs confined to a single monolayer are only weakly susceptible to the electric near fields (Figure 5.1, left side), whereas the finite extension of the wavefunction of interlayer electron-hole pairs in the heterostructure drastically increases their charge deflection, hence their polarizability (right side). In turn, the polarizability is directly reflected in the strength of the scattered THz electric field, which is detected in our experiment. Therefore, the new technique allows for practical, ultrafast and contact-free nanoscopy of interlayer tunneling as well as providing access to the subsequent ultrafast interlayer carrier dynamics.

5.1. Subcycle polarization nanoscopy

To probe the polarizability, a THz probe field is needed. In the experiment, an additional THz pulse E_{THz} is focused onto the tip besides the femtosecond light pulses used to photogenerate electron-hole pairs and delayed in time by t_{pump} (Figure 5.2a). The electric fields below the tip apex interrogate the local polarizability, which is encoded into the scattered waveform E_{scat} and analyzed by EOS in the far field (see Section 3.2.3.). Thereby, increased polarizability manifests in stronger interaction between tip and sample, increasing the effective polarizability of the tip-sample system and therefore leading to a stronger scattering response. Since the detected polarization signal scales with the probe electric field, we exploit the high-power output of the Yb:YAG thin-disk laser to generate THz probe pulses with average powers of $100\,\mu\text{W}$ and observe the nanoscopic pump-probe signals with superior signal-to-noise ratio. At the same time, the THz electric fields are not strong enough to significantly influence the type-II band alignment of the heterostructure or the tunneling process.
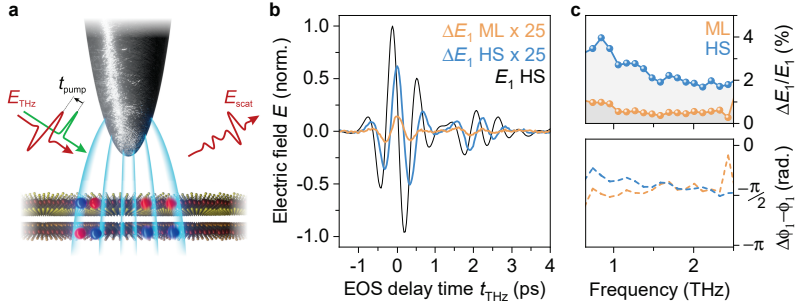
Figure 5.2 | Polarization nanoscopy. a, The pump pulse (green) photogenerates electron-hole pairs, that are probed by the electric field of the THz pulse E_{THz} (red). Electron-hole pairs within a single monolayer (left) should react significantly differently to the electric near-field (cyan), compared to spatially separated electron-hole pairs (right). This local polarizability is encoded in the scattered electric field E_{scat}. **b,** Steady-state (E_1, black) and pump-induced (ΔE_1) THz waveforms scattered off a WSe$_2$/WS$_2$ heterostructure (HS, blue, $t_{\text{pump}} = 1.25\,\text{ps}$) and a WSe$_2$ monolayer (ML, orange, $t_{\text{pump}} = 0.55\,\text{ps}$). **c,** Relative photo-induced change to amplitude $\Delta E_1/E_1$ and phase spectra $\Delta\phi_1 - \phi_1$ recorded on the heterostructure and the WSe$_2$ monolayer.

In Figure 5.2b, a typical scattered waveform E_1 (black curve) recorded on the equilibrium WSe$_2$/WS$_2$ heterostructure is displayed together with the maximum differential change ΔE_1 (blue curve) induced by the visible pump pulse. The differential signal is isolated using the additional modulation of the pump light by the AOM (see Section 3.2.), allowing for lock-in detection to suppress any background noise or power fluctuations in the probing field. In the following, these pump-induced signals are labeled with an additional Δ. The differential waveform ΔE_1 displays a phase shift of $\pi/2$ with respect to E_1, while the overall shape remains very similar. The signal ΔE_1 obtained on a WSe$_2$ monolayer shows the same behavior (orange curve). To isolate the photo-induced spectral change and remove any features of the probe spectrum or tip response, we divide the pump-induced spectrum by the steady-state spectral response. The relative photo-induced amplitude ($\Delta E_1/E_1$) of the monolayer shows an increase up to $1\,\%$, while on the heterostructure an up to $4\,\%$ higher signal is observed. Generally, pump-induced amplitude and phase ($\Delta\phi_1 - \phi_1$) of the monolayer and heterostructure exhibit no distinct signatures within our spectral range (Figure 5.2c), but a broadband overall change. No sharp features and resonances are expected, since even low-energy electronic quantum transitions such as Lyman-like $1s$-$2p$ resonances of excitons lie more than an order of magnitude above our probing frequency [Mer19]. Remarkably, the pump-induced signal from the heterostructure exceeds twice the monolayer response.

To corroborate the pure polarization response of the system and exclude any resonances emerging at later times, we also record pump-induced waveforms for different pump-probe delay times t_{pump}. Therefore, we set the delay time between pump and gate pulse $t_{\text{pg}} = t_{\text{gate}} - t_{\text{pump}}$ and use the THz delay stage t_{THz} to record the effect of the pump pulse on the whole waveform (compare to Figure 3.5c). In Figure 5.3a, the steady-state (black curve, top) and the pump induced waveform (blue curve, $t_{\text{pg}} = 1\,\text{ps}$, top) are shown. Additionally, the electric field of the waveform is color-coded in the bottom panel to show the overall trends for later pump-probe delay times. We do not observe any phase shifts or changes of the shape of the transients within 180 ps, which would be clearly visible in the two-dimensional map as shifts of the zero crossing (dashed lines in the white areas) or significant changes in the relative strength of the field crests (see inset for normalized field strength). Note that
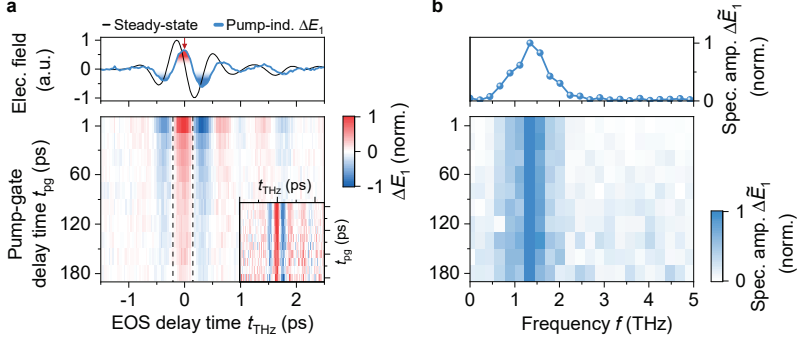
Figure 5.3 | Time evolution of the scattered THz waveform on the hetero-structure. a, Steady-state (black) and pump-induced transient (blue) recorded on the heterostructure (top panel). The lower panel shows the time dependent electric field of the pump-induced waveform for various delay times t_{pg} up to 180 ps normalized to the peak field at $t_{pg} = 1$ ps. The inset shows the same data normalized to the peak field of each row. **b,** Corresponding normalized spectra of the pump-induced signal in **a**.

even though the signal-to-noise ratio is reduced, we still record clear pump-induced features related to the electron-hole pair formation after almost 200 ps (inset and main panel). This is also reflected in the normalized pump-induced spectral amplitude, shown in Figure 5.3b. The spectral maximum is located at 1.4 THz, which typically varies slightly for different near-field tips used in the experiment. The spectrum does not change within the 180 ps, confirming the absence of any distinct electronic resonance. Hence, the broadband spectral response is the result of the nonresonant subcycle polarization of electron-hole pairs [Wan06] by the THz near fields.

In order to monitor the ultrafast photo-carrier dynamics, we trace the peak of the photo-induced waveform, $\Delta \hat{E}_1$ ($t_{THz} = 0$ ps, red arrow in Figure 5.3a), which yields the spectrally integrated response as a function of the pump delay time t_{pump} (Figure 5.4a). Interestingly, there are significant differences in the ultrafast charge carrier dynamics in monolayer and heterostructure areas. The pump-probe signal of the monolayers (orange and green curves) shows a rapid onset within the response time

of our setup as unbound electron-hole pairs are generated and intralayer excitons are expected to form [Ste17b]. Subsequently, the signal $\Delta \hat{E}_1$ decays within $\sim 2\,\mathrm{ps}$, which is consistent with spatially averaged lifetimes determined in far-field experiments [Ste17b, Mer19]. We find that while WSe$_2$ and WS$_2$ feature qualitatively the same temporal dynamics, the signal strength differs by a factor of 2.

In contrast, a profoundly different behavior is observed for the heterostructure. The magnitude of $\Delta \hat{E}_1$ is increased by up to a factor of 8, while the decay dynamics are drastically slowed down to $\sim 100\,\mathrm{ps}$, indicating the formation of long-lived interlayer excitons [Riv15, Mer19, Wan21]. A clear contrast in the lifetimes of the signal is found in the inset, showing the behavior for a longer time window. The long-lived nature of interlayer excitons is caused by the reduced spatial overlap of their
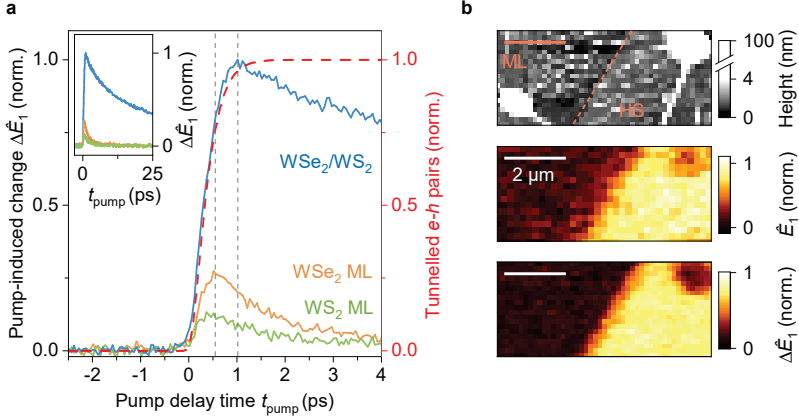
Figure 5.4 | Pump-probe dynamics of monolayers and the heterostructure. a, For both monolayers (orange, green) and the heterostructure (blue) the peak electric field $\Delta \hat{E}_1$ as function of the pump delay time t_{pump} is depicted. The density of tunneled electron-hole pairs, corresponding to the build-up of the dipole moment (red, compare to Figure 4.13b), matches the temporal evolution of the pump-probe signal on the HS. Inset: Additional data plotted for a larger range of delay times t_{pump}. **b,** Height profile (top) and emission signal $\hat{E}_1$ (center, reproduced from Figure 4.8) are compared to the spatially-resolved pump-induced signal $\Delta \hat{E}_1$ ($t_{\mathrm{pump}} = 1\,\mathrm{ps}$, bottom).

electron and hole wavefunctions. Moreover, the maximum of $\Delta\hat{E}_1$ is significantly delayed (vertical dashed lines). This characteristic delay of the maximum of the pump-probe trace perfectly matches the build-up of spatially separated electron-hole pairs after interlayer tunneling (red dashed line) extracted independently from the emission experiment in Figure 4.13b (see Section 4.2.2.). Thus, we attribute the strong increase in the pump-probe signal to the charge separation and subsequent slow recombination of highly polarizable interlayer electron-hole pairs.

The emission signal also spatially coincides with the pump-induced signal (Figure 5.4b). Comparing the newly acquired data to the emission at the step edge interface between monolayer (ML) and heterostructure (HS) shows a clear correlation of both signals. However, the acquisition time is reduced drastically by a factor of 15 for the pump-probe measurement and the signal-to-noise ratio and spatial resolution are significantly better compared to the emission signal.

Therefore, the onset of the heterostructure polarization signal directly reflects the ultrafast interlayer tunneling process, correlating in space and time with the emission experiment with significantly lower acquisition time and up to 25 times larger detected field amplitudes. Furthermore, the new technique provides access to the slow recombination of highly polarizable electron-hole pairs, which we identify as spatially separated, interlayer electron-hole pairs. In the next step, we corroborate this hypothesis by analyzing the polarizabilities of intralayer and interlayer electron-hole pairs in TMDC monolayers and heterostructures.

5.2. Polarizability of intra- and interlayer electron-hole pairs

The signal recorded on the heterostructure, especially the delayed onset and drastically slower decay dynamics, points to the formation and subsequent decay of interlayer excitons. To test this hypothesis, we investigate the polarizability of intralayer and interlayer electron-hole pairs. Careful analysis is required, since two-dimensional materials feature a strong confinement in the out-of-plane direction and hence a diminished polarizability [Tia20], while near-field nanoscopy is known to be most sensitive in this direction [Kim12]. Therefore, we quantify the sensitivity of our experiment to in-plane and out-of-plane polarization, followed by a detailed analysis of the in-plane and out-of-plane polarizability of intra- and interlayer electron-hole pairs to identify the origin of the observed signal.

5.2.1. Experimental sensitivity to in- and out-of-plane polarization

The relative sensitivity of the near-field experiment to in-plane and out-of-plane polarization can be approximated by evaluating the contributions to the scattered signal from electric fields polarized parallel ($E_\parallel$) and perpendicular ($E_\perp$) to the surface of the sample in the vicinity of the tip apex. Therefore, we adapt the FEM simulations in Section 4.2.2.. Using the same tip geometry without the point dipole emitter, p-polarized radiation with a frequency of 1.5 THz is coupled to the tip apex at an incidence angle of 60° relative to the surface normal and 45° relative to the tip-cantilever axis (Figure 5.5a), mimicking the optical setup in the experiment. A planar section of the resulting electric field distribution at the tip apex is shown in Figure 5.5b, where the logarithm of the magnitude of the electric field is represented in the color code and the arrow length, and the field polarization is reflected in the arrow direction. We identify a predominant vertical field direction below the tip apex, where field enhancement has the strongest effect. The field strength drops off exponentially when moving away from the apex and the field orientation features stronger horizontal components.
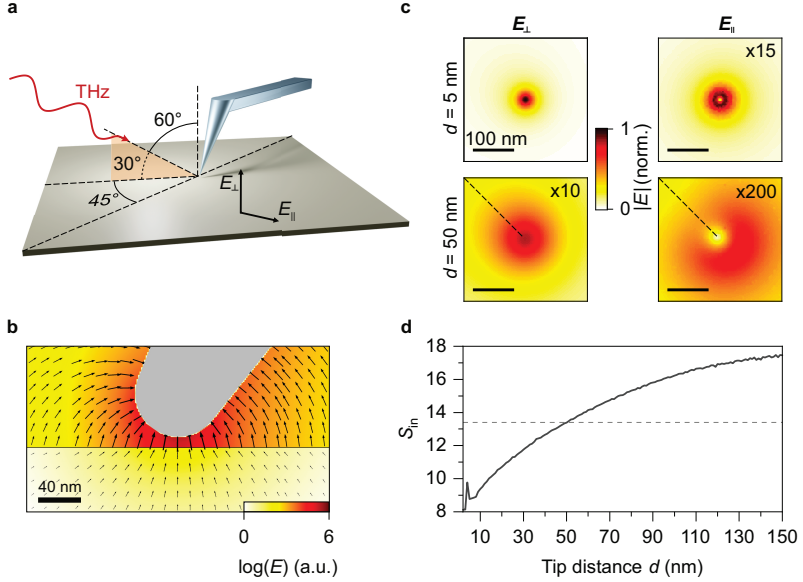
Figure 5.5 | Relative polarization sensitivity of the scattering process. a, The realistic geometry of the experiment is shown. P-polarized THz radiation is focused onto a tip under an angle of incidence of 60° relative to the surface normal and 45° from the tip-cantilever axis. The exact geometry of the tip and the cantilever is depicted in Figure 4.9. **b,** Electric-field distribution of the simulated geometry close to the tip apex, showing the color-coded field amplitude and field direction (arrow length and orientation) on a logarithmic scale for a tip-sample distance of 10 nm. **c,** Top-down view of the out-of-plane ($E_\perp$) and in-plane ($E_\parallel$) electric fields on the sample surface for a tip-sample separation of 5 nm and 50 nm, normalized to the maximum field strength of $E_\perp$ for $d = 5$ nm. The orientation of the tip shaft is marked by the dashed line. **d,** Tip-sample distance d dependent scattering sensitivity S_{in} computed from the ratio of $E_\perp/E_\parallel$ (see main text). The dashed line represents the weighted average $\bar{S}_{in}$ during a full tip oscillation with a tapping amplitude of 75 nm. For very small tip-sample distances (< 5 nm) the challenging simulation conditions (Section 4.2.2.) lead to numerical inaccuracies.

Due to the thickness of the heterostructure being only $\sim 1\,\text{nm}$ and the SiO_2 substrate producing no measurable pump-probe response, we consider only electric fields at the surface of the sample. The field strengths $1\,\text{nm}$ above the surface are depicted in Figure 5.5c for out-of-plane, i.e. vertical components $E_\perp$, and horizontal or in-plane components $E_\parallel$. For small tip-sample distances ($d = 5\,\text{nm}$) strong field confinement and large field enhancement is observed whereas $E_\perp$ shows more than one order of magnitude larger values. Note that $E_\parallel$ features no field components in the center, due to the rotational symmetry of the in-plane fields canceling to zero directly below the apex. For larger distances ($d = 50\,\text{nm}$), we find a significant reduction of $E_\perp$ and $E_\parallel$ as well as substantially weaker field confinement. In addition, a slight asymmetry occurs due to the tilted tip geometry and the tip-cantilever axis originating in the top left corner (dashed line).

To quantify the dominantly out-of-plane electric field, the mean of the ratios between $E_\perp$ and $E_\parallel$ is computed, weighted by their respective field strength $|E|$. Thus, the field orientation below the tip is obtained and hence, the relative polarization sensitivity of the incoupling process S_{in}, which determined by the coupling of propagating far fields to the evanescent near fields at the tip apex:

$$S_{\text{in}}(d) = \frac{1}{\int_A |E_{\text{i}}(d)|\,\mathrm{d}A} \int_A \frac{E_{\text{i},\perp}(d)}{E_{\text{i},\parallel}(d)}\,|E_{\text{i}}(d)|\,\mathrm{d}A \tag{5.1}$$

$$|E_{\text{i}}(d)| = \sqrt{E_{\text{i},\perp}(d)^2 + E_{\text{i},\parallel}(d)^2}\ ,$$

where A represents the sample surface containing the mesh-grid elements $E_{\text{i}}(d)$ for a given tip-sample distance d. As a result, a tip-sample distance dependent S_{in} (Figure 5.5d) that ranges from 8 to 17.5 is found. The overall ratio $E_\perp/E_\parallel$ in the experiment can be estimated by simulating a sinusoidal motion of the tip. Using a realistic tapping amplitude of $75\,\text{nm}$, we include tip-sample distances up to $150\,\text{nm}$. By calculating the weighted mean of all tip-sample distances during one oscillation cycle, the overall $E_\perp/E_\parallel$ incoupling-ratio $\bar{S}_{\text{in}}$ is determined.

In this geometry, a ratio $\bar{S}_{\text{in}} = 13.4$ (dashed line) is found. Therefore, the fields perpendicular to the sample surface dominate in-plane fields by more than one order

of magnitude. Assuming time reversal symmetry, the scattering of near fields to the far field is expected to feature the same efficiency, leading to an estimated overall experimental $E_\perp/E_\parallel$ ratio $S_\text{scat} \sim \bar{S}_\text{in}^{\,2} \sim 180$, including in- and outcoupling. Even though, the simulation only provides an approximation of the real geometry, the results should already capture the main influence of the probing tip in the vicinity of the sample surface in the experiment.

To confirm these predictions and the assumption of similar efficiencies of in- and outcoupling, we also evaluate the coupling of the near fields at the tip apex to the far field. To this end, we set up the simulation with a point dipole featuring out-of-plane ($p_\perp$) or in-plane polarization ($p_\parallel$) 1 nm above the sample surface. The tip apex is located 5 nm above the surface. Fields radiated by the dipole couple to the tip apex and are scattered to the far field for detection (compare Section 4.2.2.). Only vertically polarized light is detected in the far field to mimic the detection scheme in the experiment (Section 3.2.3.). Due to the sharp tip apex, the coupling strongly
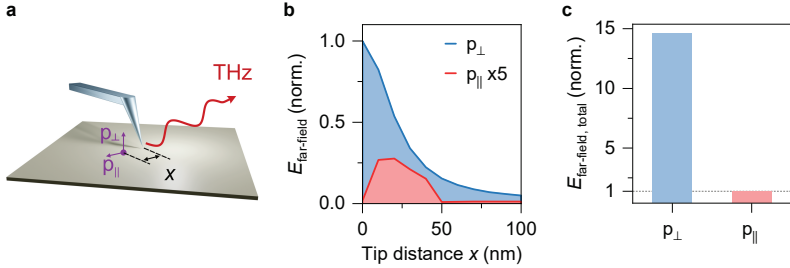
Figure 5.6 | Tip-assisted coupling of radiation to the far field. a, Geometry to simulate the outcoupling process (see also Section 4.2.2.). Point dipoles with out-of-plane ($p_\perp$) and in-plane orientation ($p_\parallel$) are placed 1 nm above the surface close to the tip apex and couple to the far field mediated by the tip. The dipoles are placed on the surface at a distance x perpendicular to the tip-cantilever axis while monitoring their scattering efficiency to the far field. The distance between tip apex and sample d was kept at 5 nm. **b,** Tip-enhanced coupling efficiency of out-of-plane (blue) and in-plane (red) dipoles for different lateral distances x. **c,** Total vertically polarized far field originating from out-of-plane ($p_\perp$) and in-plane ($p_\parallel$) oriented dipoles normalized to the in-plane value. The data was obtained by numerical integration of the graphs in **b** assuming rotational symmetry.

depends on the dipole's position below the tip. To include this in the simulation, we translate its position x along the surface perpendicular to the tip-cantilever axis (Figure 5.6a). As measure for the local outcoupling efficiency, the far-field electric field strength is shown in Figure 5.6b for each polarization $p_\perp$ and $p_\parallel$ for a range of lateral tip-dipole distances x up to $100\,\text{nm}$.

The total outcoupling efficiency $E_{\text{far-field}}$ for each polarization is determined by numerical integration of each dipole direction assuming rotational symmetry around the tip apex (Figure 5.6c). For this geometry mimicking our experimental setup, the ratio between out-of-plane and in-plane sensitivity $\bar{S}_{\text{out}} = \bar{E}_{\text{far-field},p_\perp}/\bar{E}_{\text{far-field},p_\parallel} = 14.2$. Like shown for the incoupled fields, the outcoupling process dramatically favors out-of-plane fields by more than an order of magnitude. Using the coupling to the far field, we determine an overall sensitivity $E_\perp/E_\parallel$ of the experiment in a similar manner resulting in $S_{\text{scat}} \sim S_{\text{out}}{}^2 \sim 202$, confirming very similar sensitivities of the incoupling and outcoupling process. Note that the first simulation modeling the incoupling process, was performed in greater computational detail including the three-dimensional field distribution for many tip-sample distances, and the second one mainly as verification of the assumption that the in- and outcoupling processes behave similarly.

In summary, the relative polarization sensitivity of the experiment favors out-of-plane electric fields by more than two orders of magnitude with a factor of 180 to 202. The exact value will naturally depend on the exact geometry of the tip used in the experiment and might vary for different probing frequencies, however, the simulation provides a good estimate of the experimental sensitivity to in- and out-of-plane polarizabilities.

To understand the observed differences in the monolayer and heterostructure polarization response in the near-field experiment, which mainly features out-of-plane electric fields, we investigate the out-of-plane polarizability of electron-hole pairs within van der Waals layers using density functional theory calculations.

5.2.2. Out-of-plane polarizability of intra- and interlayer electron-hole pairs

In order to determine the difference in out-of-plane polarizability of electron-hole pairs located in a monolayer or spatially separated in the heterostructure, density functional theory (DFT) calculations were performed by Dr. Paulo Faria Junior, Dr. Martin Gmitra and Prof. Dr. Jaroslav Fabian.

In general, DFT has proven to be a valuable tool to access the electronic and optical properties of atoms, molecules and solids [Sho09]. In particular, the quantum mechanical many-body problem is reduced to considerations of an overall electron density by encoding the individual potential each electron feels, including the effects of the crystal lattice, the screening of surrounding electrons and Pauli exchange interaction to an overall functional acting on the electron density [Sho09]. This leads to drastically lower computational costs and makes the simulation of systems with more than tens of electrons possible in the first place [Sho09]. Since its first steps in the 1960s, when DFT was only used by a small number of physicists and chemists, it is now a widely known technique to tackle problems in chemistry, physics, material science, chemical engineering and many other fields [Sho09]. In TMDC materials DFT has been successfully employed to compute accurate bulk band structures as early as 1972 [Bro72, Mat73] and predicted the indirect to direct bandgap transition [Leb09, Mak10, Kuc11]. Concerning van der Waals heterostructures, DFT has unraveled many fascinating phenomena in graphene [Gmi09, Gmi13, Irm15] and a variety of intriguing proximity effects in combinations of graphene and TMDCs [Gmi15, Gmi17] as well as heterostructures formed by TMDCs and ferromagnetic materials [Zol19a, Zol20]. Therefore, DFT simulations are ideally suited to calculate the electronic and optical properties of the TMDC materials investigated in this thesis, accessing the band structure and wavefunctions, while allowing one to include external electric fields to investigate the polarizability of these two-dimensional systems. The probe frequency in the experiment is chosen to remain below all relevant electronic resonances, such that the polarization of the electron-hole pairs can follow the external field quasi-instantaneously. Therefore, applying a static out-of-plane electric field and tracking the relevant quantities, allow for an excellent approximation of the out-of-plane polarizability in the experiment.
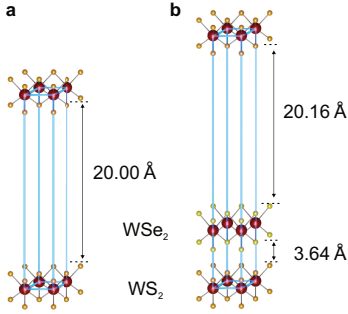
Figure 5.7 | Simulation setup for the DFT calculations. The underlying crystal lattice to simulate the band structures of the monolayers (**a**) and heterostructure (**b**) are shown. The blue rim marks the unit cell for the calculation with periodic boundary conditions. The vacuum between the layers is chosen to be 20 Å and 20.16 Å to avoid influence of the layers on themselves. The interlayer distance in the heterostructure is 3.6389 Å between the lowest and highest chalcogen atom of the top and bottom layer, respectively.

In our case, the simulations only consider the single-particle band structure and neglect the impact of excitonic effects. This assumption is justified since the binding into excitons plays a negligible role for the out-of-plane polarizability of intralayer and interlayer electron-hole pairs, as relevant quantities such as dipole strength, gauge factors and exchange valley Zeeman splitting remain nearly unaffected [Zol19b, Ted19, Far19, Zol19a, Zol20, Woź20]. Any field-induced changes to the exciton binding energy contributing to the polarizability manifest in changes of the effective masses of electron and hole in the relevant bands. In the calculation, relative variations of band curvatures are less than 10^{-3} for realistic electric field strengths of $1\,\text{V/nm}$. Hence, the energetic shifts of the bands are the dominant contribution to the electron-hole pair polarization, which are fully captured in the single-particle picture.

The heterostructure is implemented with R_{hh} stacking, where the transition metal and the chalcogen atoms of one layer are perfectly aligned with the same atom type of the other layer (Figure 5.7). The lattice mismatch in the heterostructure is accounted for by straining the WS_2 and WSe_2 layers by 1.81 % and -1.74 %, respectively. The strained lattice parameters were taken from Zollner *et al.* [Zol19b]. The optimized interlayer distance including spin-orbit coupling was found to be 3.6389 Å, consistent with recent calculations [Yua20]. A vacuum space of $\sim$20 Å was implemented to avoid the influence of the layers with themselves caused by the periodic boundary conditions (see Figure 5.7, blue unit cells). The exact computational details and simulation parameters can be found in Appendix A.
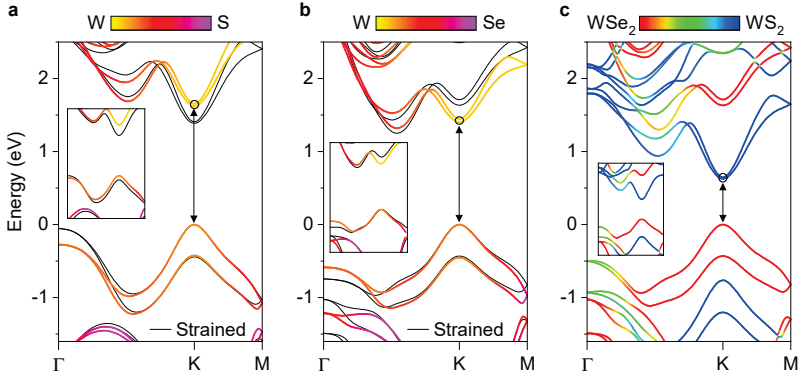
Figure 5.8 | Calculated band structures of WS$_2$ and WSe$_2$ monolayers and WSe$_2$/WS$_2$ heterostructure. **a** and **b,** Band structure for the WS$_2$ (**a**) and WSe$_2$ monolayer (**b**). The color code represents the atomic composition of the bands. The black curves show the band structures of the strained monolayers required to form the heterostructure. **c,** Band structure of the WSe$_2$/WS$_2$ heterostructure. The color code indicates the layer composition of the bands. The arrows show the energetically most favorable transitions including both conduction bands (CB+, CB-) considered for the calculations of the polarizabilities. The inset shows the band structures without spin-orbit coupling.

The resulting electronic properties of the monolayers and the heterostructure are shown in Figure 5.8. The band structure of the individual pristine monolayers (colored lines) as well as strained ones (black line), are summarized in Figure 5.8a and b. Since the strain causes visible changes in the band structures, the polarizability of the monolayers with and without strain is also analyzed. The colors represent the atomic composition of the electronic states, indicating the tungsten atom as the main contribution at the K point. The band structure for the WSe$_2$/WS$_2$ heterostructure is shown in Figure 5.8c. Here, the color code represents the layer composition of the energy bands. Particularly, the minimum of the conduction band at the K point is localized in the WS$_2$ layer while the maximum of the valence band is localized in the WSe$_2$ layer, revealing the staggered type-II band alignment of this heterostructure. The band structures without spin-orbit coupling (inset) exhibit similar behavior and show comparable atomic or layer compositions for the monolayers and

the heterostructure, respectively.

To investigate the polarizabilities of different types of electron-hole pairs, an out-of-plane electric field of $1\,\text{V/nm}$ is implemented in the DFT calculations. Considering the wavefunctions at the K point, the charge density of the relevant orbitals of the conduction and valence band

$$\rho(E_{\text{THz}} = 0) = e \times (|\Psi_{\text{VB}}|^2 - |\Psi_{\text{CB}}|^2)$$

is visualized in Figure 5.9, where Ψ_{VB} and Ψ_{CB} are the wavefunctions of the valence and conduction band at the K point, and e is the elementary charge. The photo-induced electrons contributing to the polarizability reside in the conduction band and are labeled as negative, whereas holes are located in the valence band
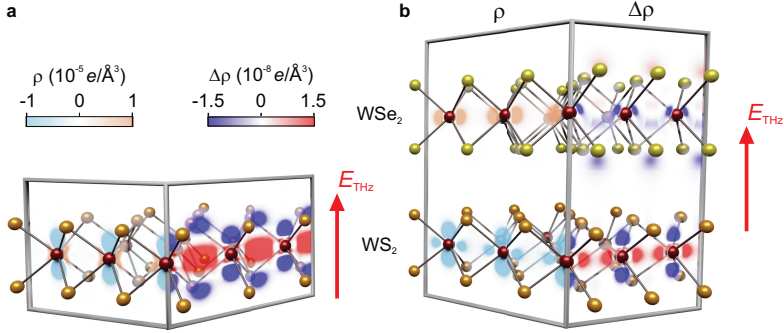
Figure 5.9 | Charge density with and without applied electric field. The left panels depict the charge density $\rho(E_{\text{THz}} = 0) = e \times (|\Psi_{\text{VB}}|^2 - |\Psi_{\text{CB}}|^2)$ of the relevant valence (VB) and conduction band (CB) at the K point of a WS_2 monolayer (**a**) and a WSe_2/WS_2 heterostructure (**b**) calculated by density functional theory in units of the elementary charge e. Photo-induced mobile holes (electrons) contributing to the polarizability are located in the valence (conduction) band and hence are labeled as positive (negative) charge density. On the right panels, the redistribution of the charge density $\Delta\rho = \rho(E_{\text{THz}} = 1\,\text{V/nm}) - \rho(E_{\text{THz}} = 0\,\text{V/nm})$ upon application of a quasi-static out-of-plane electric field E_{THz} is visualized. For clarity, the data shown do not include spin-orbit coupling.

and show a positive contribution. For the monolayer (Figure 5.9a, left), electrons and holes are in the same layer leading to overlapping wavefunctions. In contrast, the heterostructure (Figure 5.9b, left) features full charge separation reflected by the electrons in the conduction band of WS_2 (Figure 5.9b, left, bottom) and the holes in the valence band of the WSe_2 (top). The out-of-plane electric field leads to a deflection of the charge distribution. The field induced change $\Delta\rho = \rho(E_{THz} = 1\,V/nm) - \rho(E_{THz} = 0\,V/nm)$ is shown in the right panels of Figure 5.9a and b. In the monolayer (Figure 5.9a, right), the electric field shows a significant redistribution, which is almost mirror-symmetric in the out-of-plane direction, whereas the heterostructure features a clear asymmetry in the WSe_2 layer and a deflection even beyond the chalcogen atoms (Figure 5.9b, right). Therefore, spatially separated electron-hole pairs are much more susceptible to out-of-plane electric fields, specifically featuring a much higher polarizability compared to electron-hole pairs within a single monolayer.

The polarizability is quantified by considering the energy shift of the lowest energy transitions in the K valley indicated by the vertical arrows and circles in Figure 5.8. The electric-field dependence of the energies of the electron-hole pairs can be described by the Stark shift formula [Roc18, Cha19]:

$$\Delta E = -\mu E_{THz} - \frac{1}{2}\alpha_\perp (E_{THz})^2\,. \tag{5.2}$$

Here, ΔE is the energy shift, E_{THz} the applied out-of-plane electric field ranging -1.5 to 1.5 V/nm, μ is the average induced dipole moment of the transition and $\alpha_\perp$ is the out-of-plane polarizability. By fitting the field-induced energy shifts of the intra- and interlayer electron-hole pairs (see inset in Figure 5.10a), the polarizabilities are extracted. In the main panels of Figure 5.10, the results for the relevant electron-hole pairs are summarized. The colored bars represent the polarizabilities of the energetically most favorable intralayer transitions in the monolayers and interlayer transitions in the heterostructure. The monolayer and heterostructure polarizabilities for the lowest energy transition, valence band VB+ to conduction band CB− (Figure 5.10a), as well as the second lowest energy transition (Figure 5.10b), VB+ to CB+, also called A-exciton in the monolayer, are shown. The colored frames rep-
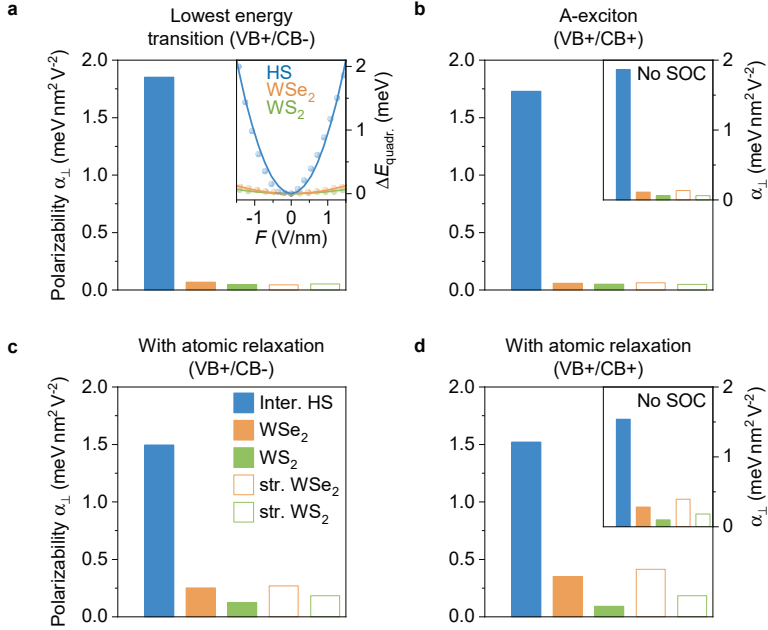
Figure 5.10 | Extracted out-of-plane polarizabilities $\alpha_\perp$ using the second order Stark shift. a, Polarizabilities of the lowest energy transitions (VB+/CB−) of WSe_2 (orange) and WS_2 monolayers (green) and the heterostructure (blue). The white filled bars represent the strained monolayers. The inset shows the quadratic energy shifts (symbols) excluding the constant offset and linear energy shift. The solid lines depict the quadratic fits. **b,** Same as in **a**, but corresponding to the A-exciton transition (VB+/CB+). Inset: Same data without spin-orbit coupling (SOC). **c** and **d,** Analogous to **a** and **b** but including atomic relaxation.

resent the polarizabilities for the strained WSe_2 and WS_2 monolayers. Comparing strained and unstrained monolayers, no significant differences are found and confirm that strain does not drastically modify the polarizabilities of the electron-hole pairs at the K point. For completeness, the polarizabilities calculated without spin-orbit coupling are plotted in the inset Figure 5.10b, which exhibit similar trends. The polarizabilities are also calculated including atomic relaxation, where the out-of-plane electric field alters the exact crystal lattice positions within the monolayers and the heterostructure. The results are shown in Figure 5.10c and d. For the lowest energy (c) and the A-exciton transition (d), a relative increase of the monolayer polarizability and a decrease of the polarizability of the heterostructure is observed, but still a strong difference between intralayer and interlayer species is found.

While the polarizabilities of the lowest energy transition including atomic relaxation in Figure 5.10c should provide the best approximation to the experiment, overall the polarizability of interlayer electron-hole pairs is always significantly larger compared to the monolayer polarizability. Even though the complex experimental setup and the coupling effects to the substrate are not accounted for, there is good agreement between the ratios of the theoretical polarizabilities and the measured peak pump-induced changes in the experiment and even the difference between WSe_2 and WS_2 monolayer is captured. The absolute values of the out-of-plane polarizabilities are calculated for an isolated monolayer or heterostructure in vacuum and will be influenced strongly by the dielectric environment and substrate material (see Appendix B).

5.2.3. In-plane polarizability of intra- and interlayer excitons

As mentioned before, the experimental sensitivity to in-plane components of the THz near field is smaller than to its out-of-plane counterpart by more than two orders of magnitude (see Section 5.2.1.). Yet, due to the strong vertical confinement, the in-plane polarizability of two-dimensional materials has been reported to exceed typical values of the out-of-plane polarizability by one to two orders of magnitude (see Appendix B), at least partially compensating for the relative insensitivity to in-plane fields.

Therefore, we estimate the in-plane polarizability $\alpha_\parallel$ of intra- and interlayer excitons by computing the two-dimensional, atom-like excitonic wavefunctions with established dielectric screening and exciton Bohr radii [Mer19]. The analytic solutions of the two-dimensional hydrogen model [Yan91] are implemented and the relevant energies and electric fields to mimic the properties of intra- and interlayer excitons are rescaled. To this end, we use the literature values for the reduced masses μ and the exciton Bohr radii a_0 obtained by solving the Wannier equation with a generalized Keldysh potential [Mer19]. Table 5.1 summarizes the parameters for our model, where m_e is the free electron mass. Based on these data, the influence of an external electric field E_{THz} on the wavefunctions of intra- and interlayer excitons can be visualized by evaluating the perturbative series [Yan91] up to the third order in E_{THz}. Due to the large binding energy of the intralayer exciton, the applied field ($E_{THz} = 0.3\,V/nm$) has almost no influence on the wavefunction (Figure 5.11a), while in the interlayer case, the wavefunction is strongly deformed by the applied electric field (Figure 5.11b), indicating a much higher polarizability of interlayer excitons.

We quantify the polarizability $\alpha_\parallel$ by computing the polarizability of the two-dimensional hydrogen atom [Yan91] in atomic units [Kre18] with the respective exciton parameters outlined above:

$$\alpha_\parallel = \frac{\mu e^2 a_0^4}{\hbar^2} \,.$$ (5.3)

Here, e is the elementary charge and $\hbar$ is the reduced Planck's constant. Spatial separation into different monolayers weakens the Coulomb attraction between electron and hole, increasing $\alpha_\parallel$ by one order of magnitude (Figure 5.11c, bars).

	Interlayer exciton WSe$_2$/WS$_2$	Intralayer exciton WSe$_2$	Intralayer exciton WS$_2$
Reduced mass μ	$0.15\,m_e$	$0.16\,m_e$	$0.154\,m_e$
Bohr radius a_0	$1.48\,\mathrm{nm}$	$0.72\,\mathrm{nm}$	$0.66\,\mathrm{nm}$

Table 5.1: Parameters used for the wavefunctions and polarizability of the two-dimensional hydrogen model [Mer19]. The reduced mass of WS$_2$ was calculated with the effective masses taken from [Kor15]. Note that the Bohr radius a_0 of WS$_2$ was obtained by rescaling a_0 of WSe$_2$ according to the ratio of the effective masses and the in-plane dielectric constants $\epsilon_{\parallel,\mathrm{WSe}_2}/\epsilon_{\parallel,\mathrm{WS}_2} = 0.88$ [Ols16].

We corroborate this prediction by directly extracting the respective in-plane polarizabilities of intralayer and interlayer excitons based on measurements of the mid-infrared dielectric function in literature [Mer19]. The experiment monitors the change of the dielectric function ϵ_{exc} due to photoexcitation of intra- and interlayer excitons within an hBN encapsulated WSe$_2$ monolayer and a WSe$_2$/WS$_2$ heterostructure. In addition, their respective intralayer and interlayer population densities n are extracted. We determine the frequency-dependent exciton polarizability by describing the Polarization $\vec{P}$ of the sample with

$$\vec{P} = n\,\alpha_{\parallel}\,\vec{E} \qquad \text{and} \qquad \vec{P} = \epsilon_0\,\chi\,\vec{E} = \epsilon_0\,(\epsilon_{\mathrm{exc}} - 1)\,\vec{E} \tag{5.4}$$

using the electric susceptibility χ. Therefore, the polarizability $\alpha_{\parallel}$ can be written as:

$$\alpha_{\parallel} = \frac{\epsilon_0}{n}\,(\epsilon_{\mathrm{exc}} - 1)\ . \tag{5.5}$$

We extrapolate their polarizability to the quasi-static limit (Figure 5.11c, red spheres) and find polarizabilities of interlayer excitons in the WSe$_2$/WS$_2$ heterostructure of $4.8{\times}10^4\,\mathrm{meVnm^2V^{-2}}$ and the encapsulated WSe$_2$ monolayer of $3.2{\times}10^3\,\mathrm{meVnm^2V^{-2}}$, in line with theoretical values (Appendix B) [Ped16, Sch16b].
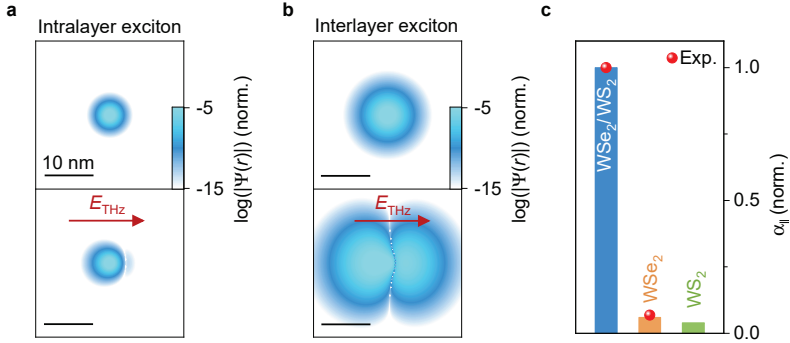
Figure 5.11 | In-plane polarizability of intra- and interlayer excitons.
a and **b,** Modulus of the wavefunction $|\Psi(r)|$ of intralayer (**a**) and interlayer (**b**) $1s$ A-
excitons for $E_{\text{THz}} = 0\,\text{V/nm}$ (top panels) and for an in-plane field $E_{\text{THz}} = 0.3\,\text{V/nm}$
(bottom panels) obtained by analytically solving the two-dimensional hydrogen
model [Yan91] with literature values [Mer19]. **c,** In-plane polarizabilities $\alpha_{\parallel}$ of the
intra- and interlayer electron-hole pairs in the monolayers and the heterostructure
calculated with the model parameters from **a** and **b**. For comparison, $\alpha_{\parallel}$ is extracted
from the dielectric function in [Mer19] and plotted (red spheres). In each case, $\alpha_{\parallel}$
is normalized to the respective $\alpha_{\parallel}$ of the WSe_2/WS_2 heterostructure.

5.2.4. Out-of-plane and in-plane polarizability in two-dimensional transition metal dichalcogenides

In summary, we find a strongly selective sensitivity of our experiment preferring out-of-plane polarization by more than two orders of magnitude (Section 5.2.1.). Investigating the out-of-plane sensitivity using DFT simulations, a substantially increased out-of-plane polarizability for interlayer electron-hole pairs is found. Additionally, in-plane polarizabilities in TMDC monolayers have been reported to exceed typical out-of-plane polarizabilities by one or two orders of magnitude (see Appendix B) at least partially compensating the selectivity in the near-field experiment and possibly contributing to the observed signal. Nevertheless, similar ratios between intralayer and interlayer electron-hole pair polarizabilities are found in the in-

Figure 5.12 | Overview of $\alpha_\perp$ (Figure 5.10c) and $\alpha_\parallel$ (Figure 5.11c).

plane direction. Thus, independent of the exact contribution of in- and out-of-plane polarization to the measured signal, a drastic increase of the polarizability of the electron-hole pairs by up to one order of magnitude is expected during the interlayer tunneling process (Figure 5.12). Moreover, the experimental findings (Figure 5.4), in particular the ratio between $\Delta \hat{E}_1$ recorded on the monolayers and the heterostructure are well reproduced by the theoretical polarizabilities in Figure 5.12. Furthermore, the experimentally observed differences between WSe$_2$ and WS$_2$ monolayers are captured in the theoretical descriptions.

Altogether, photoexcited carriers in the TMDC monolayers and heterostructure feature a substantially different behavior: In the monolayers, photogenerated carries immediately form intralayer excitons that exhibit a relatively weak polarizability, hence, signal strength and recombine within just a few picoseconds. In contrast, photoexcitation of the heterostructure generates electron-hole pairs in the constituent layers that tunnel into the adjacent monolayers on ultrafast timescales due to the type-II band alignment. Thereby, they are transformed into interlayer electron-hole pairs and their polarizability increases dramatically, which manifests in a much

stronger signal with a delayed onset in time compared to the monolayer response, due to the duration of the charge separation. Subsequently, the interlayer electron-hole pairs decay on timescales on the order of $\sim 100\,\mathrm{ps}$. Therefore, the interlayer tunneling process transforming intralayer electron-hole pairs into interlayer species and their subsequent recombination dynamics can be traced in the experiment by monitoring the dramatic change in their polarizability.

5.3. Contact-free subcycle nanovideography

5.3.1. Spatial resolution of the nanoscopy experiment

After establishing the polarizability of electron-hole pairs within the atomically thin layers as the origin of the recorded signal, near-field nanoscopy can be employed to investigate the formation and recombination dynamics with unprecedented spatial resolution and unravel previously elusive nanoscale inhomogeneities.

Therefore, we raster scan a flat area of the WSe_2/WS_2 heterostructure including nanoscale folds and inclusions. In Figure 5.13a, the height profile recorded by AFM is shown, where a very flat area is observed apart from nm-scale irregularities. In addition, a fold and an inclusion with heights of $\sim 15-20\,$nm are visible. We record the peak of the photo-induced change in the electric field $\Delta\hat{E}_1$ at a delay time of $t_{pump} = 30\,$ps (Figure 5.13b). The near-field signal reflects many of the small topographic irregularities, while a clear reduction of the signal is visible at the fold and the inclusion. Furthermore, a clear step edge in the signal strength is visible
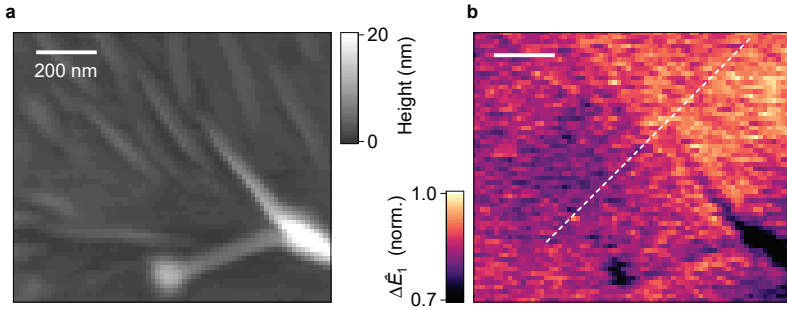
Figure 5.13 | High resolution topography and pump-induced signal map of the heterostructure. a, Topography map of a sub-micrometer area featuring a large fold with a height of $\sim 15-20\,$nm and an otherwise very flat region with few-nm inhomogeneities. **b,** False-color plot of the pump-induced signal $t_{pump} = 30\,$ps after photoexcitation featuring not only clear contrast of the topographically significant fold, but also traces of the small irregularities. In addition, we find an overall split between signal strength in the bottom left and top right region.

following the fold from bottom right to top left, revealing significant differences in the interlayer dynamics on the nanoscale. By taking a line cut marked by the white dashed line, we extract the height profile (Figure 5.14a) and signal change (Figure 5.14b, red line). The AFM scan reveals the very flat surface of the hetero-structure, only showing fluctuations smaller than 3 nm over a distance of 900 nm. At the same time, the signal strength changes rapidly by $\sim 10\%$ in the center of the scan window. We use the sharp increase in the signal to determine the spatial resolution of our new technique for typically employed commercial near-field probes featuring a radius of curvature smaller than 20 nm (25PtIr200B-H, Rocky Mountain Nanotech-nology LLC). Compared to the probes used in the emission experiment, these tips feature a sharper apex leading to an increased field confinement, but a decrease in the overall recorded signal amplitude. By fitting the photo-induced response with a step function (dashed line), we can extract the distance from 20% to 80% of the step height to define the spatial resolution [AG17]. As a result, we find 43 ± 5 nm as the spatial resolution, where the error margins are given by the 95% confidence interval of the fitting procedure. Therefore, the electric field is strongly confined to the tip apex, allowing for spatial resolution better than 50 nm even though we employ radiation with wavelengths of $100\,\mu\text{m} - 1\,\text{mm}$. Note that the signal-to-noise ratio, indicated by the error bar on the left (blue), is more than sufficient to easily observe and distinguish a 10 % change in the recorded signal amplitude.

Furthermore, retraction scans are used to better understand the near-field signal recorded on the heterostructure. For the steady-state waveform, we record the peak electric field $\hat{E}_2$ and for the pump-induced change, we monitor the induced peak electric field $\Delta\hat{E}_{1/2}$ at $t_{\text{pump}} = 1\,\text{ps}$ (Figure 5.14c). The tip-sample separation is slowly increased, while the tip is oscillating above the surface with a constant tap-ping amplitude. Since the commonly accepted method of using the decay length of the signal as a measure for the spatial resolution or the vertical spatial con-finement of the electric field is an unjustified approximation for such a complex measurement consisting of several convoluted effects [Moo20], the retraction scans are used here to identify background contributions to the near-field signal. For ex-ample, signals originating from the tip shaft or cantilever will decrease very slowly or not at all during the retraction scan. The steady-state peak electric field $\hat{E}_2$ (blue
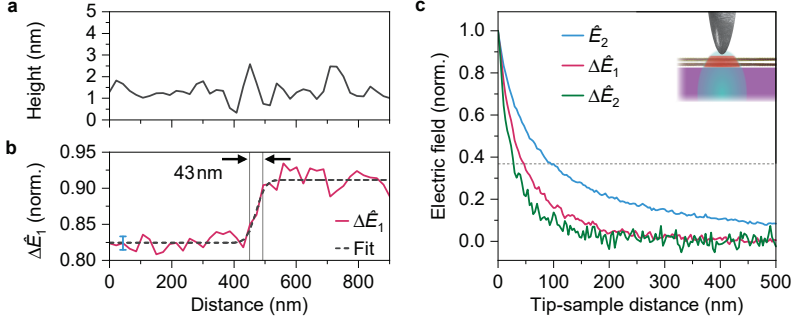
Figure 5.14 | Determining the spatial resolution of the experimental setup.
a, Topography of the line cut marked in Figure 5.13b showing slight variations on
the few-nm scale. **b,** Pump-induced signal $\Delta\hat{E}_1$ (red) for $t_{\mathrm{pump}} = 30\,\mathrm{ps}$, featuring
a clear step edge. The dashed line represents the fit with a step function featuring
a characteristic step width of 43 nm defined by the distance from 20 % to 80 % of
the step height (vertical lines) and is commonly used as a measure for the spatial
resolution. The error bar at $\sim 50\,\mathrm{nm}$ (left, blue) shows the standard deviation of
$\Delta\hat{E}_1$ of the flat part before the step edge. **c,** Retraction scans on the $\mathrm{WSe}_2/\mathrm{WS}_2$
heterostructure monitoring the peak electric field in the steady-state $\hat{E}_2$ and for
the pump-induced case $\Delta\hat{E}_1$ and $\Delta\hat{E}_2$ after $t_{\mathrm{pump}} = 1\,\mathrm{ps}$ for a tapping amplitude
of 80 nm. The inset shows a schematic of the expected probing volume of the
steady-state signal (cyan ellipse) and the pump-induced response (red area), which
is confined to the heterostructure.

line) and the corresponding pump-induced change $\Delta\hat{E}_1$ (red line) and $\Delta\hat{E}_2$ (green
line) decrease exponentially, however, they exhibit quite different decay lengths.
Typically, a higher demodulation order features a stronger field confinement (Section 3.1.). Nonetheless, we find $\Delta\hat{E}_1$ decaying twice as fast as $\hat{E}_2$, reaching its $1/e$
value (dashed horizontal line) at 46 nm. As expected, $\Delta\hat{E}_2$ decays even faster. This
especially short decay length for the lower demodulation order $\Delta\hat{E}_1$ compared to
$\hat{E}_2$ that seemingly contradicts the commonly accepted knowledge of stronger field
confinement for higher demodulation orders [Kno00, Moo20], is attributed to two
factors: First, the relatively small spot size of the pump beam ($\sim 1\,\mathrm{\mu m}$) only photogenerates carriers in the vicinity of the tip apex, preventing contributions to the
scattered signal which originate from regions far away ($\sim 100\,\mathrm{\mu m}$) from the apex

such as radiation scattered off the tip shaft or cantilever that are typically present in the steady-state case $\hat{E}_{1/2}$ [Mas17]. This is observed in the nonzero signal of $\hat{E}_2$ at the tip-sample distance of 500 nm. Furthermore, in the case of the monolayer and heterostructure, the probing depth is limited to ~ 1 nm for all pump-probe signals $\Delta\hat{E}_{1/2}$ (see inset in Figure 5.14c, red area), in contrast to the total scattered THz fields $\hat{E}_2$, which probe into the SiO$_2$ substrate below the heterostructure (cyan ellipse) [Moo20].

Altogether, the near-field experiment is able to investigate the full life cycle of inter-layer electron-hole pairs, formation and recombination, with true nanoscale resolution below 50 nm, while providing sufficient signal-to-noise ratio to enable practical contact-free nanoscopy of the ultrafast interlayer dynamics.

5.3.2. Interlayer formation and recombination dynamics on the nanoscale

In Figure 5.13, we already found significant differences in the scattered signal, that may be caused by differences in the local formation or recombination dynamics. In this part, we investigate this behavior systematically by recording snapshots of a large area of our heterostructure sample for delay times t_{pump} up to 180 ps. In Figure 5.15a, the height profile of the sample region is shown. The center of the false-color plot features a large heterostructure area (HS2), containing many flat areas separated by folds and inclusions. Above (ML2) and in the top right (ML3), WSe$_2$ monolayer regions can be identified using the AFM scan and the optical images recorded during fabrication. The top left corner consists of a smaller WSe$_2$ monolayer (ML1), heterostructure (HS1) and a WS$_2$ monolayer covered by a WSe$_2$ bilayer forming a trilayer heterostructure (TL-HS). The bottom left shows a flat area with an increased density of inclusions and would be typically identified as a heterostructure (HS3), however, does not feature the typical behavior as discussed below. Most likely, this area was damaged or contaminated in between the layers during the transfer or annealing process.

Using steady-state THz nanoscopy to trace the peak electric field $\hat{E}_1$, we can check for any unwanted doping and corroborate a homogeneous response of the investigated
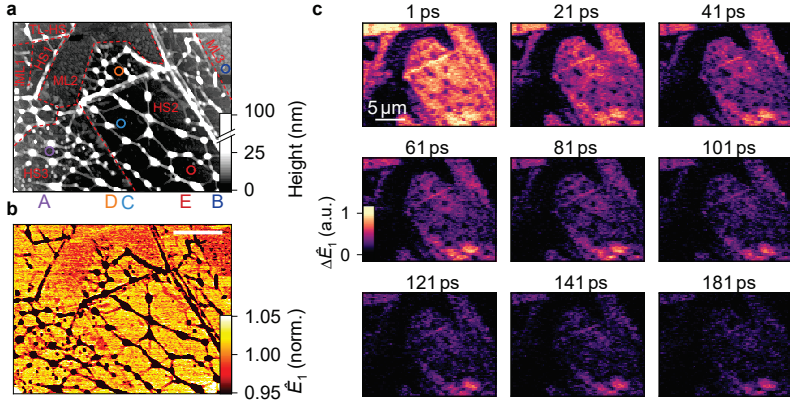
Figure 5.15 | Snapshots of a heterostructure area. a, AFM image of a large area of the heterostructure featuring regions with different characteristics indicated by the dashed red lines. The center features a large heterostructure (HS2) with the characteristic flat areas separated by folds and inclusions. To its left and right, WSe$_2$ monolayer (ML2, ML3) regions can be identified. In the bottom left corner is a heterostructure featuring an increased density of inclusions (HS3), which does not feature the typical heterostructure behavior (see **c**). The top left corner consists of smaller regions of monolayer (ML1), heterostructure (HS1) and a WSe$_2$ bilayer as constituent of a trilayer heterostructure (TL-HS). The circles mark the positions of fits A to E in Figure 5.16a. Scalebar, 5 µm. **b,** Steady-state THz map tracking the peak electric field $\hat{E}_1$ and resolving small differences between monolayer and heterostructure areas, while showing a drastic difference at folds and inclusions. Scalebar, 5 µm. **c,** Snapshots of the pump-induced signal $\Delta\hat{E}_1$ of the area from **a** and **b** for delay times t_{pump} up to 180 ps.

area (Figure 5.15b). A strong reduction in the scattered signal is observed at the inclusions. Otherwise, all areas show a very similar scattering response which is slightly reduced at monolayer regions in the top center and top right corner. A slight increase in the scattered electric field is observed in the bottom right corner.

Next, we analyze the pump-induced response of the area. Using the new experimental setup, subsequent snapshots after photoexcitation are recorded. An overview is shown in Figure 5.15c, where the delay time increases from top left to bottom right. Using the first two images ($t_{\text{pump}} = 1$ ps and $t_{\text{pump}} = 21$ ps), we corroborate the

identification of the areas seen in Figure 5.15a. Heterostructure areas feature large signals, which decay on timescales on the order of $100\,\mathrm{ps}$ and are visible in all snapshots, but exhibit clear differences in signal strength and decay time. In contrast, monolayer areas show a relatively weak signal, which is not present in the second image at $t_{\mathrm{pump}} = 21\,\mathrm{ps}$ in agreement with the few-ps decay observed in Figure 5.4a. The area in the bottom left corner (HS3) shows no pump induced-change at all. We attribute the absence of any signal to a deficient transfer process or contamination during fabrication, leading to an exceptionally high density of adsorbates between the layers and preventing proper contact of the monolayers. Furthermore, one or both monolayers may have disintegrated during the annealing process. The top left trilayer heterostructure shows a slightly increased signal and similar decay dynamics, however this will not be discussed in detail since the coupling of two WSe$_2$ layers and one WS$_2$ layer leads to convoluted effects including an emerging indirect bandgap in the type-II band alignment and hybridization of intra- and interlayer excitons in the homobilayer [Mer20]. Most importantly, we find a small area in the bottom right corner featuring a drastically increased signal strength and lifetime.

We summarize the whole nanomovie by fitting the signal trace at each pixel of the snapshots with a monoexponential decay $\Delta E_1^{\mathrm{max}} \times \mathrm{e}^{-t/\tau}$ and extracting the signal amplitude $\Delta E_1^{\mathrm{max}}$ and decay time τ. Thereby, $\Delta E_1^{\mathrm{max}}$ is a measure of the tunneling efficiency between the layers, while τ reflects the lifetime of the interlayer electron-hole pairs. The fitting procedure for representative regions in Figure 5.15a (colored circles) is shown in Figure 5.16a, reproducing the recorded signal traces very well. The symbols represent the data from the snapshots and the line shows the respective monoexponential fit. Obviously, areas with no pump-induced change (HS3, A) and monolayer regions (ML3, B) can be identified easily. The traces on the heterostructure (HS2, C, D, E) show a substantially increased signal strength and a drastically increased lifetime, while featuring significant variations in their decay dynamics.

The resulting maps of tunneling efficiency $\Delta E_1^{\mathrm{max}}$ and lifetime τ are shown in Figure 5.16b and c, respectively. $\Delta E_1^{\mathrm{max}}$ shows clear contrast on inclusions and between monolayer and heterostructure areas, but features only slight variations in signal strength between individual heterostructure areas. In order to visualize the decay
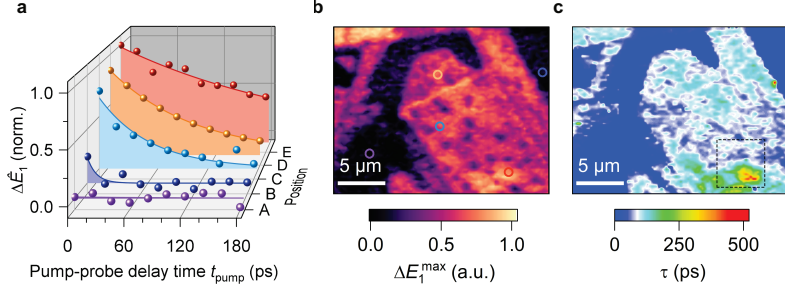
Figure 5.16 | Extracting tunneling efficiency and lifetime of the interlayer electron-hole pair formation and recombination. a, Data (spheres) and fits (lines, areas) of various positions marked in **b** and in Figure 5.15a. Traces with no pump-induced change are found on the inclusion rich area (A) and fast dynamics are observed on the monolayer (B). Even within the heterostructure, significant differences in the pump-induced change are observed (C, D, E). **b** and **c,** Amplitude $\Delta E_1^{\max}$ and lifetime τ extracted by fitting a monoexponential decay ($\Delta E_1^{\max} \times e^{-t/\tau}$) to the temporal evolution of $\Delta \hat{E}_1$ at each pixel. The black dashed frame in **c** indicates the investigated area in Figure 5.17.

times, the extracted lifetime is additionally filtered before being plotted in Figure 5.16c. Thereby, for points in space showing a signal amplitude $\Delta E_1^{\max}$ smaller than 20 % of the maximum signal, the τ values are set to zero (dark blue), since the fitting of the decay time gets unreliable or even meaningless in the absence of a pump-induced signal (compare Figure 5.16a, A). Additionally, this allows us to focus on the differences for heterostructure areas only. The extracted lifetimes of the interlayer electron-hole pairs on the heterostructure show substantial differences typically ranging from 100 to 250 ps.

Strikingly, there is an area in the bottom right corner that exhibits a dramatically increased lifetime τ up to 500 ps, exceeding the typical heterostructure behavior by far. We zoom into this area (Figure 5.16c, dashed frame) and color-code $\Delta E_1^{\max}$ and τ on top of the topography of the region, which is simultaneously acquired by AFM (Figure 5.17). Thereby, the surface and contour lines, which are spaced by 12 nm, represent the height profile. The tunneling efficiency $\Delta E_1^{\max}$ is significantly reduced at the topographic features, which we attribute to spatial separation of
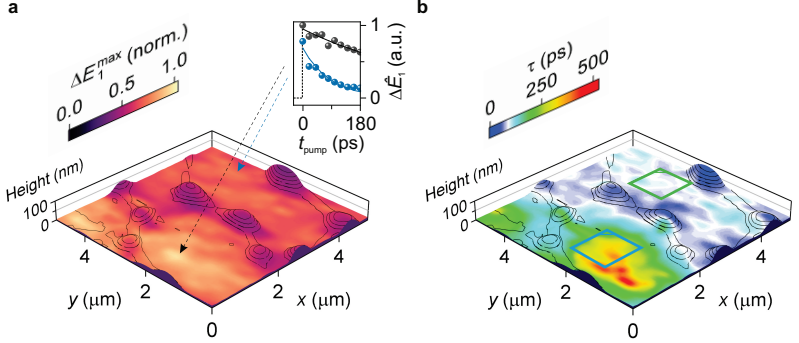
Figure 5.17 | Resolving nanoscale inhomogeneities of tunneling efficiency and electron-hole pair lifetimes by ultrafast contact-free nanoscopy. **a,** Magnitude of the pump-induced changes in scattered electric field ΔE_1^{max} color-coded onto the topography. The inset shows the experimental data (symbols) and fits (solid lines) for two representative flat areas. **b,** Characteristic lifetime τ of the photogenerated carriers color-coded onto the topography. The colored frames indicate the area investigated in Figure 5.18.

the heterostructure into its constituent monolayers. Even on the topographically flat areas, subtle variations in ΔE_1^{max} are observed indicating that the formation of interlayer electron-hole pairs may be modulated by previously undetected nanoscale differences in charge transfer efficiency. The lifetime τ of the spatially separated electron-hole pairs varies by as much as a factor of three within the investigated area. Local regions of extended lifetimes seem to correlate with high photo-induced pair densities. Remarkably, we observe significant differences in electron-hole pair lifetimes between topographically similar flat regions (inset in Figure 5.17a and Figure 5.17b). The areas with extended electron-hole pair lifetime may be free of any imperfections and defects, which would open additional recombination channels [Lee14].

Close-up images of the flat regions (blue and green frame in Figure 5.17b, corner for orientation) are recorded for three respective delay times and are shown in Figure 5.18 with their respective AFM scan. Both topographies show similar few-nm-high features. While the decay dynamics are significantly different for the flat areas
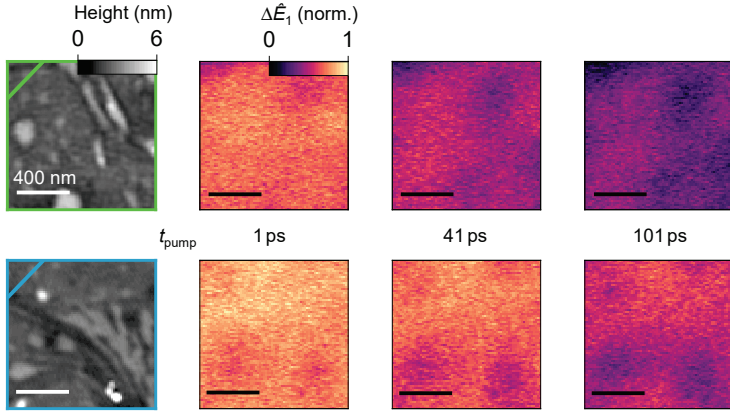
Figure 5.18 | High-resolution images of flat areas of the heterostructure.
AFM maps of the flat areas (see colored frames in Figure 5.17, corner for orientation, gray scale) and corresponding signal $\Delta \hat{E}_1$ (color scale) for different delay times. The characteristic length scale of the modulation in $\Delta \hat{E}_1$ (~ 400 nm) is significantly larger than both the spatial resolution of our s-SNOM setup (~ 50 nm) and the topographic features in the left panels.

that are a few micrometers apart and substantially influenced by strong topographic features on the order of 100 nm such as inclusions or folds, the scattering response seems relatively homogeneous within the flat areas. The signal amplitude varies only slowly on these regions on length scales ~ 400 nm, significantly larger than our spatial resolution smaller than ~ 50 nm, and appears immune to few-nanometer-tall topographic folds. Therefore, the heterostructure seems to remain intact on the nanoscale, with the interlayer exciton likely robust to the subtle changes of the local dielectric environment. Hence, we propose that the larger area of extended lifetime shown in Figure 5.17 (blue square) could arise from an advantageous local atomic registry, through twist angle [Mer19] or strain [Zol19b, Bai20].

In summary, contact-free subcycle nanoscopy allows us to monitor the local polarizability of electron-hole pairs in atomically thin van der Waals heterostructures accessing the interlayer tunneling dynamics during the formation of spatially sep-

arated electron-hole pairs in a non-invasive manner and without driving external currents. Therefore, the new technique should readily lend itself to the observation of tunneling in insulating, conducting or superconducting systems on subcycle timescales and with nanoscale precision. Moreover, the new concept can explore the recombination dynamics of these indirect, optically dark interlayer species [Mer19] and therefore provides a novel tool to investigate interlayer excitons during their full life cycle. By exploiting the subcycle temporal and nanoscale spatial resolution of our new nanoscopy experiment, we can already identify significant variations in the formation efficiency and lifetime in a representative heterobilayer. Furthermore, we found that the interlayer exciton formation is robust to few-nanometer-tall impurities and its formation and recombination dynamics vary on length scales of 400 nm most likely caused by the local twist angle or strain. In the future, the new technique can be used to investigate two-dimensional materials and devices on the relevant nanoscale length- and ultrashort timescales to understand the role of interlayer tunneling in phase transitions or energy harvesting and light emitting processes. Looking forward, the new concept may even facilitate the visualization of photo-carrier trapping in moiré potentials in future experiments under low temperatures and ultra high vacuum including even higher quality samples, which our research group is working on right now.

As an outlook to ongoing experiments, in the following the interlayer dynamics of the WSe_2/WS_2 heterostructure are investigated for different photo-induced carrier densities.

5.4. Saturation of the type-II band alignment

In excitonic systems, the density of charge carriers is of particular interest and crucially influences whether electron-hole pairs are present in their bound exciton form or in an ionized electron-hole plasma. Sufficiently high carrier densities lead to efficient screening of the strong Coulomb interaction and prevent the formation of bound electron-hole pairs, which is called Mott transition [Che15, Ste17a]. In systems like the WSe_2/WS_2 heterostructure, featuring a staggered type-II band alignment with a band offset of hundreds of meV [Kan13, Gon13, Hil16, Zha16], the density of tunneled carriers has additional effects, applying a reverse field that counteracts the type-II band offset. A sufficient reversed field will even prevent further carriers to tunnel like observed in the saturation effects in THz emission experiments [Ma19], critically limiting the yield in light harvesting devices. However, insights on interlayer formation and recombination dynamics in this limiting case have still been elusive.

Therefore, we perform preliminary experiments monitoring the formation and recombination dynamics in our WSe_2/WS_2 system for different pump fluences at a center wavelength of 515 nm, i.e. photogenerated charge carrier densities. The pump-induced peak electric field $\Delta \hat{E}_1$ is measured for delay times t_{pump} up to 170 ps while varying the fluence from 5 to $60\,\mu\mathrm{J\,cm^{-2}}$. The result is plotted in Figure 5.19a, where each curve is the average of three consecutive scans and a running average over three data points is applied. For the measurement with $60\,\mu\mathrm{J\,cm^{-2}}$ only one trace was recorded, since the pump fluence is above the damage threshold, where the heterostructure degrades over time and hence a quick acquisition time was essential causing a decreased signal-to-noise ratio.

As a result, we find very similar pump-induced signal traces as seen before in Figure 5.4a. As expected, higher pump fluences, hence higher carrier densities, lead to an increased signal (Figure 5.19a), however, the maximum peak electric field does not increase proportionally to the pump fluence. When looking at the trace with the lowest $(5\,\mu\mathrm{J\,cm^{-2}})$ and highest fluence $(60\,\mu\mathrm{J\,cm^{-2}})$, the photoexcitation is twelve times stronger, while not even a factor four is found between the respective peak electric fields $\Delta \hat{E}_1$. We quantify this behavior by extracting the peak signal at 1.5 ps

after photoexcitation for each fluence (dashed line in the inset of Figure 5.19a) resulting in the graph in Figure 5.19b. Despite having difficulties to determine the exact average power of the pump beam for the low fluence values (see first two data points) due to the low optical power on the order of $150 - 300\,\mu\text{W}$, a clear linear behavior for pump fluences up to $22\,\mu\text{J}\,\text{cm}^{-2}$ is found. For higher fluences the signal shows a significant deviation from the linear scaling, indicating the saturation effect that was observed before in far-field experiments [Ma19]. The carriers tunneling into the adjacent layer lead to a reverse electric field, that counteracts the type-II band alignment and thereby prevents further efficient tunneling.

Moreover, we find an obvious difference in the recombination dynamics. For low pump fluences, a pure monoexponential decay is observed, while an additional fast decay emerges for fluences higher than $15\,\mu\text{J}\,\text{cm}^{-2}$ (light blue curve in Figure 5.19a). To systematically investigate the additional decay, the data is fitted with a biexponential decay $A_1 e^{-t/\tau_1} + A_2 e^{-t/\tau_2}$ with the amplitudes $A_{1/2}$ and the decay times $\tau_{1/2}$. Thereby, we analyze only the decay starting from the dashed line in the inset of Figure 5.19a on the modified time axis $t_{\text{p,mod}} = t_{\text{pump}} - 1.5\,\text{ps}$. Additionally, the fitting was constraint to extract a slow ($\tau_1 > 100\,\text{ps}$) and a fast decay constant ($\tau_2 < 100\,\text{ps}$). In Figure 5.19c, the signal from three different pump fluences and their respective fits are shown. For low fluences (gray), there is only a monoexponential decay ($A_2 = 0$) while the blue and yellow curve feature an additional fast decay ($A_2 > 0$). Thereby, the dashed lines indicate the slow decay ($A_1 e^{-t/\tau_1}$), while the solid lines show the full biexponential fit.

The amplitudes $A_{1/2}$ and decay times $\tau_{1/2}$ are extracted, and plotted separately in Figure 5.19d and e. For the slow decay (blue symbols and line), there is an overall similar decay rate represented by the average value of $168\,\text{ps}$ (dashed line in Figure 5.19d), not changing significantly with increased pump power. For fluences higher than $10\,\mu\text{J}\,\text{cm}^{-2}$, the fast decay sets in with decay times below $40\,\text{ps}$ decreasing even more for higher fluences. The extracted amplitude A_1 of the slow decay shows a quick saturation for values higher than $20\,\mu\text{J}\,\text{cm}^{-2}$ (Figure 5.19e). Accounting for the upper limit of the absorption of the heterostructure of $30\,\%$, this corresponds to a photogenerated carrier density of $3.1 \times 10^{13}\,\text{cm}^{-2}$ in the heterobilayer,
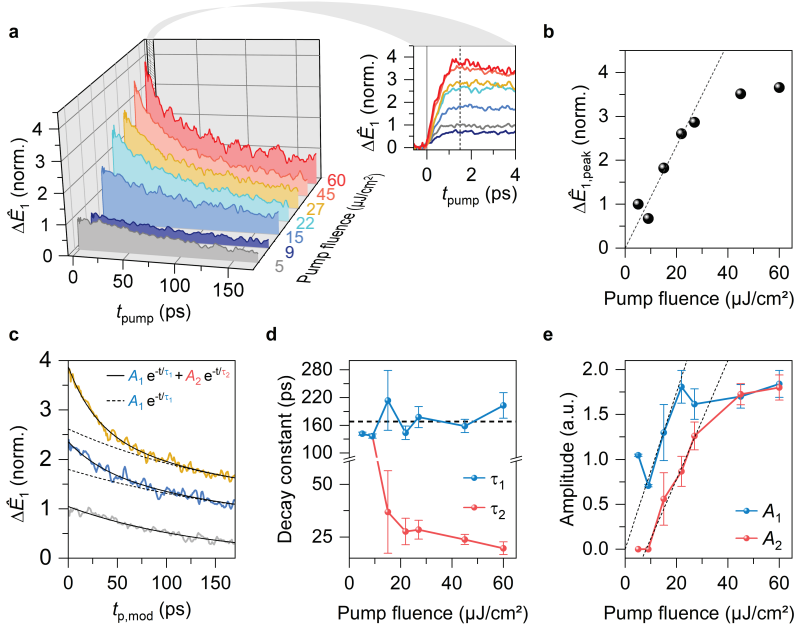
Figure 5.19 | Saturation of the interlayer charge transfer. a, Pump-induced change $\Delta\hat{E}_1$ for several pump fluences as a function of the pump-probe delay time t_{pump}. Inset: Onset of the pump induced signal $\Delta\hat{E}_1$. **b,** Maximum of $\Delta\hat{E}_1$ extracted from the vertical dashed line in the inset in **a**, showing a saturation behavior for pump fluences larger than $22\,\mu\text{J}\,\text{cm}^{-2}$. **c,** Three representative pump-probe traces measured with different pump fluences. Biexponential fit function (black line) and slow decay component (black dashed line) are shown. Note that $t_{p,mod}$ is zero at the vertical dashed line in the inset in **a** ($t_{p,mod} = t_{pump} - 1.5\,\text{ps}$) to isolate the decay dynamics. **d,** Decay constants τ_1 and τ_2 from the fitting procedure. τ_1 exhibits similar values for all fluences with an average value of 168 ps (dashed line). In contrast, τ_2 emerges with a value of 37 ps at $15\,\mu\text{J}\,\text{cm}^{-2}$ and reduces further for increasing fluences. **e,** Extracted amplitudes A_1 and A_2. A_1 increases linearly with increasing pump fluence until saturating for values larger than $22\,\mu\text{J}\,\text{cm}^{-2}$. The amplitude A_2 of the faster decaying term only contributes for pump fluences larger than $15\,\mu\text{J}\,\text{cm}^{-2}$ and increases linearly with increasing pump power. Both amplitudes A_1 and A_2 show saturation behavior for pump fluences higher than $20\,\mu\text{J}\,\text{cm}^{-2}$ and $30\,\mu\text{J}\,\text{cm}^{-2}$, respectively. The error bars in **d** and **e** represent the 95% confidence interval of the fitting procedure.

comparable to the value $1.9 \times 10^{13}\,cm^{-2}$ observed before on similar heterostructures[1] [Ma19]. In contrast, the amplitude A_2 of the fast decay only contributes for pump fluences higher than $10\,\mu J\,cm^{-2}$ and increases roughly linearly up to almost $30\,\mu J\,cm^{-2}$ (dashed line as guide to the eye) before starting to saturate.

We attribute the more complex decay dynamics to the reverse field of the transferred charge carriers competing with the type-II band alignment. When a sufficient density of carriers has transferred, they prevent additional highly polarizable interlayer electron-hole pairs to form. The absence of charge separation and hence higher spatial overlap of electron and hole wavefunctions leads to a fast decay within tens of picoseconds, which is still slower than the decay of pure intralayer population indicating a remaining significant effect of the neighboring monolayer. Possibly, electron tunneling is hindered more quickly in the conduction bands due to the smaller band offset [Kan13, Zha16] causing only a partial charge separation, and more intralayer like electron-hole pairs. After an initial fast decay, the slow monoexponential decay attributed to interlayer electron-hole pairs remains.

The preliminary data set already reveals fascinating behavior. However, a more controlled experiment and systematic analysis are needed to provide a quantitative interpretation, since the observed signal could originate from a multitude of convoluted effects. While no pump fluence dependent absorption was observed in similar heterostructures [Ma19], the carrier density in a single monolayer influences its carrier decay time due to Auger recombination [Poe15] and a reduced exciton lifetime due to the increased confinement of electron and hole within the same layer of a WSe_2 homobilayer was observed [Mer20]. The additional Auger recombination or fluence dependence of the pump light absorption may also explain the saturation of the amplitude A_2 of the fast decay for the largest fluences.

This complex behavior will be analyzed in more detail in future experiments on heterostructure and homobilayer systems. Moreover, the nanoscale spatial resolution of the new technique cannot only provide fascinating insights on formation and

---

[1]The stated threshold carrier density in Ma *et. al.* [Ma19] is $1.3 \times 10^{13}\,cm^{-2}$, which includes a transfer efficiency between the layers of 70 %. The transfer efficiency is removed to compare only the photoexcited carriers leading to the value $1.9 \times 10^{13}\,cm^{-2}$ in the text above.

recombination of interlayer electron-hole pairs, but may be used to find local differences in these high-pump-fluence dynamics to further the understanding of the relevant decay channels or even resolve nanoscopic inhomogeneities in the type-II band alignment.

Chapter 6

High-power mid-infrared sources for next generation subcycle near-field microscopy

In the last chapter, subcycle THz near-field nanoscopy has proven itself a valuable tool to nonresonantly investigate the local polarizability of electron-hole pairs in van der Waals heterostructures revealing significant differences in the formation and recombination dynamics of interlayer excitons on the nanoscale. However, many fascinating phenomena in condensed matter physics can be addressed selectively using their resonance energies of 10 to 100 THz in the mid-infrared spectral range. These low-energy excitations include internal transitions of excitons in van der Waals Systems [Poe15, Ste17b, Ste18, Mer19, Mer20, Mer21], collective oscillations of charge carriers, called plasmons [Hub01, Tal19], as well as vibrations of the crystal lattice, called phonons [Gun00]. In particular, ultrafast field-resolved mid-infrared spectroscopy provides direct access to the spectral amplitude and absolute phase response of the sample system allowing for the retrieval of the dielectric function with extreme temporal precision down to 10 fs [Hub01, Poe15, Ste17b, Ste18, Mer19, Mer20, Mer21].

In near-field microscopy, mid-infrared radiation is already widely employed with numerous applications in physics, chemistry and biology [Che19b]. In particular, the linear [Bao15, Par18, Zha18a] and nonlinear [Jia19] optical response of van der Waals systems has been explored and even moiré superlattices have been visual-

ized [Sun18, Sun20]. Strongly confined mid-infrared radiation has resolved phase transitions with high spatial resolution [Qaz07, Liu13b, Hub16, McL17, Pos18] and investigated magnetic domain switching [Jan20]. Additionally, the nanoscale dielectric functions of liquids [Lu19b] and layered materials have been accessed [Gov14, Moo18]. Moreover, surface polaritons, describing the coupling of light to elementary excitations of matter interfaces allow for control and confinement of light on the nanoscale forming for example low-loss, hyperbolic phonon polaritons in hexagonal boron nitride [Dai14]. These polaritons are promising candidates for future information technology, due to the ability of controlling and tuning their opto-electronic properties, like in highly-tunable surface plasmon polaritons on graphene [Fei12] or fully switchable interface polaritons in black phosphorus silicon dioxide heterostructures [Hub17].

However, so far most near-field experiments have relied on intensity-resolved detection or Fourier transform spectroscopy schemes, therefore limiting the temporal resolution to a single oscillation cycle of the mid-infrared probe radiation. In order to achieve even better temporal resolution and get the full benefit out of the detected scattered light, the waveform originating from the near-field tip needs to be resolved in the time domain analogous to the field-resolved detection used in the previous chapters. As a result, access to the spectral amplitude and absolute phase are possible. In a proof of concept, the ultrafast response of indium arsenide nanowires has been explored employing field-resolved detection allowing for simultaneous temporal resolution of 10 fs and spatial resolution of 10 nm [Eis14]. Nevertheless, due to the extremely small probing volume in the near-field and the relatively low-power mid-infrared sources used in previous field-resolving near-field experiments, only about 50 photons per probe pulse contributed to the recorded signal [Eis14] limiting the applicability of the technique.

To achieve practical ultrafast field-resolved near-field microscopy, high-average power mid-infrared sources featuring high-repetition rates sufficient for near-field microscopy are required. Typically, ultrashort mid-infrared pulses are generated by nonlinear frequency mixing of broadband near-infrared or visible pulses. Nonlinear mixing and broadening schemes need high pulse energies to be efficient and in combination with the necessary repetition rates for s-SNOM experiments, this leads to

high-average powers, that are incompatible with conventional broadening schemes and can cause catastrophic damage in bulk crystals or fibers. We want to tackle this problem aiming for a high-power mid-infrared source using our thin-disk oscillator in combination with state-of-the-art high-power broadening schemes and intra-pulse difference frequency generation. In collaboration with Prof. Dr. Oleg Pronin from the Helmut-Schmidt-Universität in Hamburg, we implement a bulk crystal broadening scheme based on self-defocusing $\chi^{(2)}$-nonlinearities before generating tunable high-power mid-infrared pulses. By collaborating with Dr. Francesco Tani from the Max Planck Institute for the Science of Light in Erlangen, photonic crystal fibers are employed to push the broadening even further increasing bandwidth and pulse energy of the mid-infrared probe pulses. In the following, we discuss both approaches to generate high-power few-cycle mid-infrared pulses ideally suited for field-resolved near-field microscopy.

6.1. Mid-infrared generation using pulse compression in self-defocusing bulk media

To generate femtosecond phase-stable mid-infrared pulses, the oscillator output needs to be broadened sufficiently to support frequencies that are separated by more than $20 - 30 \, \text{THz}$. Spectral broadening is often achieved by self-phase modulation, which is a consequence of the optical Kerr effect [Boy08]. Thereby, the time dependent intensity $I(t)$ leads to an additional contribution to the refractive index:

$$n = n_0 + n_2 I(t) \tag{6.1}$$

where n_0 is the usual weak-field refractive index and n_2 the second-order index of refraction [Boy08].

An electromagnetic pulse can be described by a frequency dependent amplitude $\tilde{E}(\omega)$ and corresponding phase $\tilde{\varphi}(\omega)$ in the frequency domain or by using the intensity envelope $I(t) = E(t)^2$ and the instantaneous phase $\varphi(t)$ in the time domain . More intuitively, we consider the instantaneous frequency $\omega_{\text{inst}} = \frac{d}{dt}\varphi(t)$, which describes which oscillation frequency arrives at each point in time. For a compressed pulse, originating for example from a laser oscillator, it is constant and reflects the center frequency ω_0 of the pulse. The intensity dependent refractive index leads to:

$$\omega_{\text{inst}} = \omega_0 - \frac{\omega_0}{c} n_2 L \frac{\partial I(t)}{\partial t} \tag{6.2}$$

where L is the length of the nonlinear medium and c is the speed of light [Boy08]. Therefore, the modified instantaneous frequency ω_{inst} features new frequencies at the rising and falling edge of the intensity envelope of the pulse leading to a broadening of the frequency spectrum [Boy08].

We collaborate with Prof. Dr. Oleg Pronin, Dr. Marcus Seidel[1] and Dr. Jonathan Brons[1] to implement a highly efficient bulk crystal broadening scheme for mid-infrared generation. When employing conventional self-phase modulation, the intensity dependent refractive index also gives rise to self-focusing in the crystal lead-

---

[1]Max Planck Institute for Quantum Optics in Munich

ing to an additional reduction of the beam size causing large losses in the material, promoting the excitation of higher order spatial modes, which leads to lower efficiencies [Sei17] or even damaging the crystal. The key difference in the compression scheme set up by Seidel *et. al.* [Sei17] is using the nonlinear refractive index, caused by cascaded phase-mismatched $\chi^{(2)}$-nonlinearities in BBO crystals, to counteract the self-focusing of the Kerr effect allowing for thicker crystals and longer strongly confined propagation, and thus providing efficient broadening [Sei17]. As a result, the oscillator output with an average power of 90 W and a pulse duration of 200 fs is compressed to 30-fs-long pulses at an average power of 70 W by employing three consecutive broadening and compression stages. The details of the setup can be found in Reference [Sei17].

The experimental setup to generate mid-infrared radiation is shown in Figure 6.1a. The oscillator output is broadened and compressed [Sei17] before most of the power is routed into the generation arm, whereas a small part of the compressed pulse (~ 100 mW) is split off to be used as the gate pulse for electro-optic detection. The corresponding spectrum is shown in Figure 6.1b. The dashed line displays the fundamental spectrum of the oscillator output, while the colored line indicates the spectral intensity after the compression. To ensure efficient mid-infrared generation by intra-pulse difference frequency mixing (see also Section 3.2.2.), the frequency components need to be broadened accordingly by $20 - 30$ THz. Therefore, only small contributions are expected from the central peak of the spectrum. To optimize the generation process, we implement a modified prism compressor allowing for frequency filtering and fine tuning of the spectral phase of the generation pulse. Two D-shaped mirrors in the Fourier plane of the prism compressor reflect the low and high frequencies selectively (blue areas in Figure 6.1b), while maintaining a shared beam path of both frequency wings leading to a high phase stability in the mixing process. Additionally, the polarization of the low frequencies is rotated by 90° using two passes through a quarter-wave plate ($\lambda/4$). Therefore, the low and high frequency spectral wings are perpendicularly polarized to meet the polarization requirements for critical phase matching [Boy08] and optimize the efficiency of the mixing process. By reducing the overall power of the generation beam (~ 70 W) to only the frequencies that contribute most to the mixing process (~ 5 W), the focus
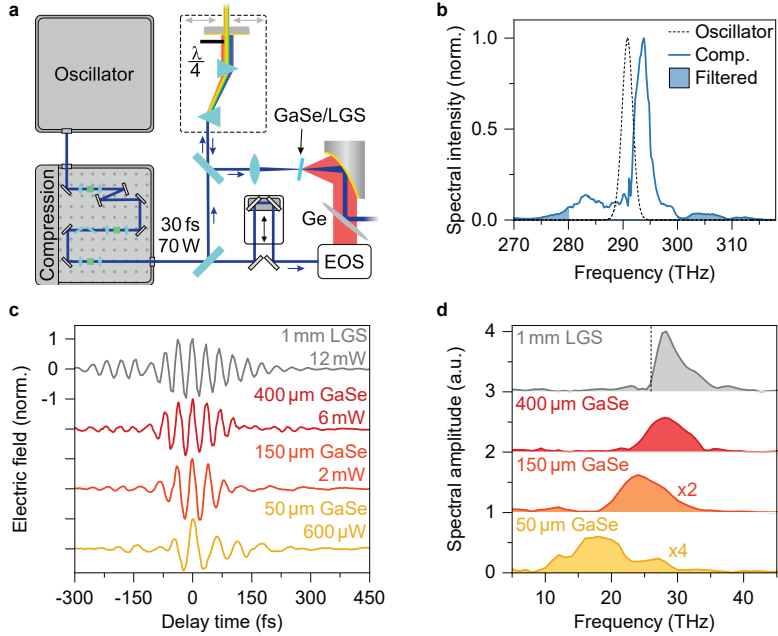
Figure 6.1 | Mid-infrared generation using bulk crystal broadening. a, In the experiment, the output of the oscillator is broadened and compressed, before being split into the generation and detection arm. The spectrum of the generation pulse is filtered (see blue areas in **b**) using a modified prism compressor with D-shaped end mirrors to choose the contributing frequency components. Additionally, the polarization of the low frequency wing is rotated by 90° using two passes through a quarter-wave plate ($\lambda/4$). The generation light is focused into a nonlinear crystal (GaSe/LGS) and the resulting mid-infrared radiation is collimated and overlapped with the detection gate pulse to be recorded by EOS after passing through a germanium wafer. **b,** Intensity spectrum of the oscillator (dashed black line) as well as the broadened and compressed pulse (blue). The blue shaded areas indicate the filtered frequencies to optimize the mid-infrared generation using the modified prism compressor (here shown for a frequency separation of 20 THz). **c,** Recorded mid-infrared waveforms for $LiGaS_2$ (LGS, gray) and gallium selenide (GaSe, red orange and yellow) with different crystal thicknesses. **d,** Corresponding amplitude spectra. The dashed line represents the phonons below 26 THz within the LGS crystal, limiting the bandwidth of the generated spectrum.

spot size can be chosen significantly smaller without damaging the crystal, increasing the peak intensity and hence mixing efficiency of the relevant frequency components. After the prism compressor, the generation beam is focused into a nonlinear crystal and the generated radiation is collimated with a parabolic mirror. At last, EOS is used to analyze the mid-infrared pulses after passing through a germanium wafer to remove the residual generation light. In our experiments, we employ $LiGaS_2$ (LGS) and gallium selenide (GaSe) for generation, due to their large nonlinear coefficients, broadband infrared transparency and strong birefringence that allows for tunable phase matching [Kno17]. A 60-µm-long GaSe crystal is used for EOS in combination with the detection arm providing gate pulses with a pulse duration of 30 fs.

We first optimize the system for highest average power and use $\sim 3\,\text{W}$ in each frequency wing. The LGS crystal with a thickness of 1 mm is chosen due to its higher damage threshold and favorable phase matching around 30 THz compared to GaSe [Kno17]. We generate and record a mid-infrared waveform (Figure 6.1c, gray) and record an average power of up to 12 mW, which is more than 20 times the power that was used before for field-resolved near-field microscopy. The transient seems to have a small pre-pulse and features many oscillation cycles. This is attributed to the strong cutoff due to phonons in LGS below 26 THz (specified by the supplier ASCUT) indicated in the corresponding spectrum by the black dashed line in Figure 6.1d.

Using GaSe crystals with different thicknesses, we avoid phonon absorption and can generate lower frequencies. In order to achieve broadband mid-infrared spectra, we employ GaSe crystals with 400 µm (red), 150 µm (orange) and 50 µm (yellow) in thickness. These lead to few-cycle pulses with few mW in power and can even reach a single-cycle waveform. Note that thinner crystals lead to broader spectra (red $\rightarrow$ orange $\rightarrow$ yellow) and lower generated average power, but the center frequency is determined by the phase-matching angle.

Therefore, the thin-disk oscillator in combination with the broadening and compression stage provides high-average power mid-infrared pulse trains for near-field microscopy, which should allow for experiments with subcycle temporal resolution and simultaneous spatial resolution of 10 nm in the mid-infrared spectral range with dramatically increased field amplitudes and signal-to-noise ratio.

6.2. Mid-infrared generation using spectral broadening in photonic crystal fibers

To improve the spectral broadening even more and increase the generation efficiency, we collaborate with Dr. Francesco Tani, Dr. Felix Köttig and Daniel Schade from the group of Prof. Dr. Philip Russell at the Max Planck Institute for Science of Light in Erlangen, who are experts in photonic crystal fibers. Together, we successfully implemented a yet more impressive mid-infrared generation source. In contrast to conventional fibers, which rely on total internal reflection in the solid fiber core, photonic crystal fibers are employed [Erm19, Köt20a, Köt20b]. Particularly, we employ a gas-filled single-ring hollow-core photonic crystal fiber (HCPCF) [Köt20a], where the photonic bandgap effect [Rus03] confines the light in the gas-filled center of the fiber leading to its extremely high damage threshold.

Broadening and compression

Similarly to before, we use self-phase modulation inside the HCPCF. Fibers in general allow for strongly confined light, similar to the focus of a beam, but over large distances. The pressurized gas inside the fiber acts as the nonlinear medium exhibiting a relatively low nonlinearity compared to bulk crystals [Leh85, Boy08], but features field confinement and broadening along the full length of the fiber, and an extremely high damage threshold. Since gases are inversion symmetric and therefore have no second-order nonlinear susceptibility [Boy08], the third-order optical Kerr effect is the dominant nonlinearity leading to self-phase modulation. The resulting broadening depends on the pulse energy, the nonlinearity and pressure of the gas, and the length and core diameter of the photonic crystal fiber.

In our experiment, we employ a 3.2-m-long single-ring HCPCF with 12-thin-walled capillaries filled with krypton gas at a moderate pressure of 15 bar and a relatively large core diameter of 86 µm to reduce the peak intensities and increase stability allowing for efficient broadening even at high repetition rates in the MHz range [Köt20a]. First, we study the spectral broadening as a function of the average input power (Figure 6.2a). The output of the oscillator is coupled into the fiber and the resulting spectra are recorded. For small powers up to 2 W the original spectrum
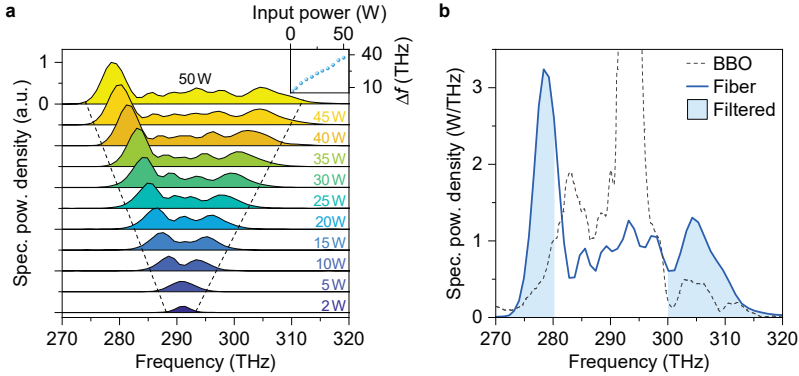
Figure 6.2 | Spectral broadening in a gas-filled photonic crystal fiber. a, Intensity spectra after transmission through a single-ring hollow core photonic crystal fiber (HCPCF) filled with krypton gas for input powers up to 50 W. The spectral broadening depends linearly on the input power indicated by the dashed lines and the inset, showing the full width at 10 % of the maximum bandwidth Δf for increasing input powers. **b,** Comparison of the fully broadened spectrum after the bulk crystal compression (black dashed line) and after the HCPCF (blue). The intensity spectrum of the HCPCF features a lot more spectral power in the outer spectral wings indicated by the blue areas that are spaced 20 THz apart.

of the oscillator remains (dark blue). Starting at 5 W of input power, there is a significant broadening of the spectrum. The typical broadening caused by self-phase modulation in HCPCF features the characteristic symmetric splitting of the spectral peak starting at 10 W. Further increasing the power leads to a linear increase in bandwidth (see inset), which is indicated by the black dashed lines as guide to the eye for the bandwidth at 10 % of the maximum spectral peak[2]. While more central peaks emerge, the lowest and highest frequency peaks remain the dominant spectral features with an increased broadening efficiency for the low frequencies. When reaching an input power of 50 W, corresponding to a pulse energy of 2.1 μJ, a dramatically broadened spectrum spanning almost 40 THz is recorded , with clearly visible spectral maxima at 278 THz and 304 THz. For even higher powers, the

---

[2]Here, the unconventional bandwidth defined by the full width at a tenth of the maximum spectral intensity is used due to the complex shape of the broadened near-infrared spectrum.

broadening gets unstable due to high intensities at the fiber incoupling facet [Köt20a] and overall high-average power, heating fiber and gas. An average power of 42 W of the broadened radiation is measured after the fiber corresponding to a broadening efficiency of 85 % including losses at windows and lenses. The spectrum is shown in Figure 6.2b, where the blue filled areas indicate a clear increase of the power in the spectral wings compared to the bulk crystal compression scheme before (black dashed line).

During the broadening process, dispersion caused by transmission through the gas-filled fiber as well as self-phase modulation lead to a relative delay between constituent frequencies of the pulse, so called chirp, which stretches the pulse in time. To analyze the fiber output, we employ the well-established technique of frequency-resolved optical gating (FROG), which is typically used to characterize ultrashort laser pulses [Tre97]. Thereby, the pulse is split into two identical copies and non-collinearly overlapped in a thin BBO crystal to generate the sum frequency, which is analyzed by a spectrometer. By varying the delay time between the two pulses, a two-dimensional map of the sum-frequency spectrum for different delay times is recorded. Using a numerical algorithm, the spectral amplitude and relative phase[3] are iteratively reconstructed [Kan99].

In the top panels of Figure 6.3, the two dimensional FROG measurement (a), its corresponding reconstructed intensity spectrum and phase (b) and the intensity envelope in time (c) are shown. In general, small differences in FROG traces are difficult to interpret directly, however general trends are rather obvious. In Figure 6.3a, the sum-frequency (SF) signal is stretched out for more than 1 ps, while in the compressed case (d) the SF intensity vanishes within 200 fs, indicating a much shorter pulse. The reconstructed spectrum (Figure 6.3b, blue line and area) shows a similar spectrum as seen in Figure 6.2b. The phase (red) exhibits a dominating parabolic shape indicating the aforementioned chirp caused by dispersion within the fiber. The characteristic measure for the chirp of the pulse is the group delay dispersion (GDD), which is defined by the curvature of the phase at a certain frequency. Small GDD values represent a flat spectral phase corresponding to com-

---

[3]The sign of the spectral phase cannot be determined directly from the measurement, due to the symmetry in the mixing process, and is conventionally determined by adding a medium with known dispersion into the beam path to calibrate the measurement.
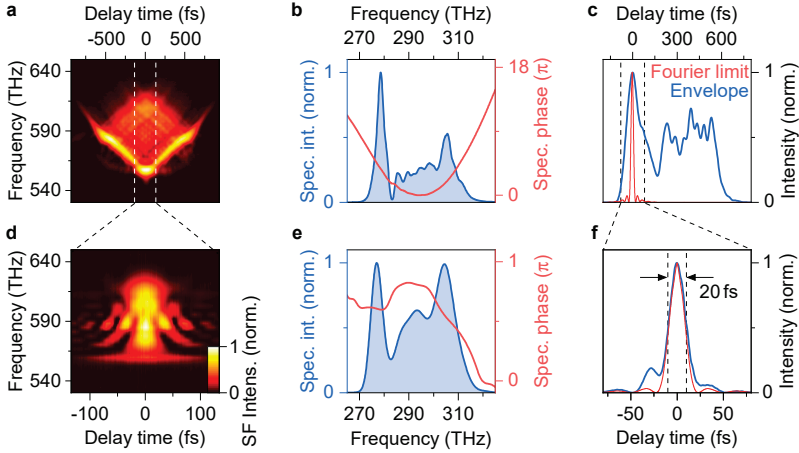
Figure 6.3 | Compression of the broadband spectrum after the photonic crystal fiber. a, Frequency-resolved gating (FROG) map recording the intensity of the sum-frequency signal (SF Intens.) of two identical copies of the fiber output in a thin BBO crystal for different delay times. Strong intensities are observed within a window of more than 1 ps indicating a dramatically stretched pulse. **b,** Reconstructed intensity spectrum (blue line and area) and phase (red line) of the fiber output. The phase shows a dominant parabolic feature caused by dispersion and self-phase modulation. **c,** Reconstructed time-domain intensity envelop directly after the HCPCF. The pulse is stretched out over more than 600 fs (blue), while the Fourier limited pulse duration is 19 fs (red line). The dashed lines indicate the window size after compression. **d,** FROG map of the compressed pulse. **e,** Reconstructed intensity spectrum (blue line and area) and phase (red line) after the compression. **f,** Reconstructed time-domain intensity envelope after the compression stage. The retrieved pulse shape (blue) features a pulse duration of 20 fs, which is very close to the Fourier limited case of 19 fs (red).

pressed pulses, while large GDD values describe pulses that are stretched in time [Sal91]. We extract the GDD by fitting the spectral phase with a polynomial function and average the second order parameter between the two outer spectral peaks resulting in GDD values from 2700 to 2850 fs^2 depending on the degree of the polynomial. In Figure 6.3c, the intensity envelope of the fiber output (blue) is shown in the time domain. The long travel within the gas-filled fiber and the large extracted GDD value are reflected by the substantial difference in its pulse duration (~ 600 fs) compared to the Fourier limited pulse (red), which describes the shortest pulse that the intensity spectrum can support with a flat phase.

To compress the pulse, we implement dispersion compensation using a pair of chirped mirrors with a total GDD of -2800 fs^2. These mirrors achieve frequency dependent contributions to the spectral phase using precise dielectric coatings to control the penetration depths, and thus the length of the beam path of each wavelength. The FROG data after compressing the pulse is shown in Figure 6.3d, e and f. The dashed lines indicate the dramatically decreased time window (Figure 6.3d and f). We find a relatively flat spectral phase (Figure 6.3e, red), which features mostly residual higher order chirp that should not significantly stretch the pulse. The GDD is strongly reduced to average values between -35 and -80 fs^2 when fitting with polynomials of higher degree and can be easily removed by adding a few mm of a transmissive medium into the beam path. The resulting pulse duration of the compressed near-infrared pulse (Figure 6.3f, blue) is 20 fs, which is defined by the full width at half maximum (FWHM) of the intensity envelope and is only slightly longer than the Fourier limit (red, pulse duration: 19 fs). Note that the intensity spectrum of uncompressed (Figure 6.3b) and compressed pulse (e) differ, which is caused by a slightly different phase-matching angle of the BBO crystal during the FROG measurement or inaccuracies of the reconstruction algorithm. To improve the retrieval of the original spectrum without the influence of the BBO phase matching, the FROG setup can be calibrated by comparing the FROG results to the intensity spectrum recorded by the spectrometer. In our case, the effect is negligible, since the Fourier-limited pulse durations of both spectra are the same.
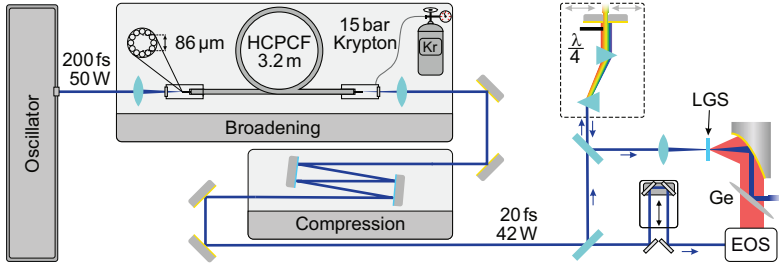
Figure 6.4 | Schematic of the mid-infrared generation setup using the photonic crystal fiber. An average power of 50 W of the oscillator output (pulse duration: 200 fs) is focused into the 3.2-m-long single-ring HCPCF with 12 thin-walled capillaries around the core (diameter: 86 μm), which is filled with krypton gas at a pressure of 15 bar. The fiber output is collimated and compressed by a pair of chirped mirrors with a total GDD of $-2800 \, \text{fs}^2$ resulting in near-infrared pulses with a pulse duration of 20 fs and an average power of 42 W. The beam is split into a generation arm and a low-power gate pulse train for detection. The generation light is frequency filtered in a modified prism compressor to cut out the central part of the spectrum and focused into a 1-mm-long LGS crystal. The resulting mid-infrared radiation is transmitted through a germanium (Ge) wafer to filter the generation light before being detected by EOS.

High-power mid-infrared generation

The experimental setup to generate the high-power mid-infrared pulses is shown in Figure 6.4. The oscillator output of 200-fs-long pulses at an average power of 50 W is broadened in the HCPCF and compressed to a pulse train with a pulse duration of 20 fs and an average of 42 W. Similarly to before, we split the beam using most of the power for the generation. The modified prism compressor is used to filter the spectrum and rotate the polarization of the lower frequency spectral wing to increase the efficiency of the mixing process. This time, we only employ a 1-mm-long LGS crystal, since the broadened frequency wings allow for high spectral power separated by more than 26 THz (compare Figure 6.2b). The generated mid-infrared radiation is transmitted through a germanium window to remove the near-infrared light and recorded by EOS using a contacted GaSe flake with a thickness of less than 10 μm [Kno18] allowing for an ultrabroadband detection bandwidth.

First, we aim for pulses with maximum bandwidth. Therefore, we employ $\sim 3\,\mathrm{W}$ of each frequency wing and mix them in the LGS crystal. As a result, a few-cycle mid-infrared pulse is detected (Figure 6.5a, orange) featuring a pulse duration of 80 fs, defined by the FWHM of the intensity envelope (gray area). The spectrum features components from 30 to almost 45 THz and a FWHM of the spectral amplitude of 8.9 THz centered at 35.5 THz (Figure 6.5b, orange line and area) with a flat spectral phase (black dashed line). An average power of 20 mW is measured after the germanium wafer ready to be coupled into the s-SNOM experiment. An estimate of the expected field strengths is calculated by assuming the diffraction limited spot size in the near-field experiment of 10 μm FWHM. Thus, the high bandwidth pulses reach peak electric fields of up to $2.5\,\mathrm{MV\,cm^{-1}}$ (Figure 6.5a, orange). Next, we increased the generation power to $\sim 5\,\mathrm{W}$ in each frequency wing to maximize the mid-infrared power. The generated pulse (red) features a slightly longer pulse duration of 89 fs (gray area) and a spectral red shift towards 31.5 THz and a bandwidth of 8.5 THz FWHM due to the decreased separation of the frequency wings. At the same time, the average power reaches up to 80 mW, which corresponds to peak fields of up to $4.5\,\mathrm{MV\,cm^{-1}}$ in the experiment.

By using spectral broadening inside a photonic crystal fiber, we are therefore able to generate few-cycle mid-infrared pulses that reach peak electric fields of several $\mathrm{MV\,cm^{-1}}$. In the near-field experiment, tip enhancement is expected to increase the electric fields by at least a factor of 5 for free-standing tips [Krü11, Her12]. When the tip is close to a sample surface, enhancement factors far higher than 15 are reached depending on tip geometry and tip-sample distance [Boh01, Nee18]. Thus, the new source reaches field strengths that compete with atomic potential gradients in solids providing access to nonlinear phenomena. Therefore, future experiments may explore novel regimes of nonlinear nanooptics [Jia19]. Moreover, previously elusive strong field physics leading to high harmonic generation by driving Bloch oscillations [Sch14] or quasi-particle collisions [Lan16] can be probed with nanoscale precision. In addition, the strong fields may be employed to influence the band alignment in van der Waals materials such as driving ultrafast currents in homobilayers or even dramatically reshape the band alignment in heterostructures on subcycle timescales.
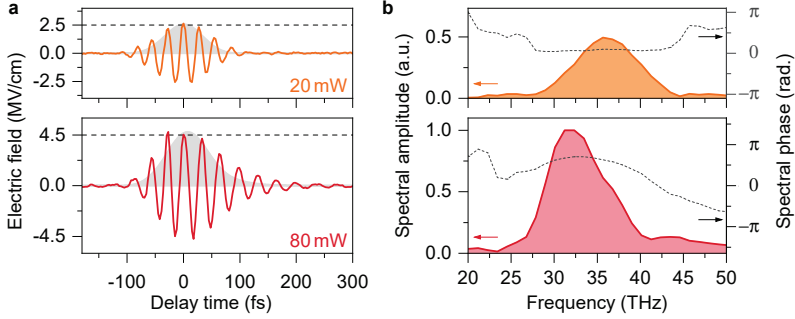
Figure 6.5 | High-power ultrashort mid-infrared pulse generation and field-resolved detection. a, Field-resolved waveform optimized for bandwidth (orange) and average power (red). The peak electric field is calibrated to a diffraction limited spot size of 10 μm accounting for the specifications of the near-field microscope. The gray areas indicate the intensity envelope with a pulse duration of 80 fs (orange, top) and 89 fs (red, bottom) **b,** Corresponding spectral amplitude (colored lines and areas) and phase (black dashed line). The respective axis are indicated by the arrows.

In this chapter, promising exploratory steps were made towards a high-power mid-infrared source for ultrafast near-field microscopy with subcycle temporal resolution. Combining the thin-disk oscillator with state-of-the-art high-power broadening and compression schemes, ultrashort mid-infrared pulses were generated ranging from broadband single-cycle waveforms, which may be applicable for light-wave driven scanning tunneling microscopy [Coc13, Coc16, Yos16, Jel17, Yos18, Gar20, Yos19, Mül20, Pel20, Pel21], to extremely strong few-cycle pulses protruding into the strong-field limit, reducing the acquisition time of field-resolved data manyfold and pushing near-field microscopy to the next level. The many opportunities to apply the nanoscale spatial and subcycle temporal resolution in the mid-infrared spectral range such as studies of linear and nonlinear ultrafast interlayer dynamics [Mer19, Mer20] and excitonic transitions in van der Waals materials as well as pushing conventionally linear systems to their nonlinear limit [Sch14], foreshadow fascinating future experiments.

Chapter 7

Conclusion and outlook

In this thesis, a novel concept has been introduced to investigate the interlayer tunneling in atomically thin van der Waals heterostructures on subcycle timescales with nanoscale precision in a contact-free manner that even works on insulators. For this purpose, we have exploited the transient polarizability of electron-hole pairs for non-invasive THz nanoscopy of the ultrafast interlayer tunneling and recombination dynamics in WSe_2/WS_2 heterostructures. Our experiments have not only made use of the versatile portfolio of near-field microscopy, including laser THz emission nanoscopy and scattering-type scanning near-field optical microscopy, but also conceptually bridge the gap to lightwave-driven scanning tunneling microscopy.

A novel experimental setup has been designed and implemented pioneering an ultrafast high-power thin-disk oscillator in combination with a scattering-type near-field microscope to perform ultrafast field-resolved THz nanoscopy. Using the thin-disk oscillator, phase-stable THz pulses with spectral components ranging from 0.5 to 3 THz and average powers of 100 µW have been generated and coupled to the near-field microscope. Field-resolved detection has been implemented to access the THz waveform in the time domain with subcycle temporal resolution. As a result, our experiment can access the local conductivity in the THz spectral range, as well as ultrafast charge transfer processes using THz emission nanoscopy. Moreover, the ultrafast evolution of the local polarizability after photoexcitation can be monitored using ultrafast visible pump/THz probe time-domain spectroscopy.

As representative samples, WSe_2/WS_2 and $WSe_2/MoSe_2$ heterostructures have been fabricated with lateral dimensions of tens of micrometers and pre-characterized using optical microscopy. By employing THz nanoscopy it has been possible to investigate the local optical THz response of these TMDC heterostructures that are smaller than the THz diffraction limit at full sample size. Thereby, we have even resolved local nanoscale inhomogeneities of the optical conductivity caused by trapped particles and potential variations of the background doping. These pre-characterizations have already shown that our setup will be a promising tool for future studies of van der Waals heterostructures as well as novel semiconductor and topological insulator nanostructures in the THz spectral range.

Moving towards the main goal of this thesis, observing the interlayer dynamics of van der Waals heterostructures, we have successfully confirmed interlayer tunneling within the fabricated WSe_2/WS_2 heterostructures using THz emission nanoscopy. Due to the type-II band alignment, photo-induced charge carriers favor one or the other layer and tunnel accordingly. We have been able to resolve the emitted THz waveform originating from this interlayer tunneling process between two atomically thin TMDC layers over a distance of less than 1 nm. This corresponds to an emission volume, which is 12 orders of magnitude smaller than the diffraction limit. Additionally, local differences in the emission signal and the boundaries of the heterostructure have been observed. No emission signal has been found on the substrate or monolayer. In an inverted WS_2/WSe_2 heterostructure an emission waveform with reversed polarity has been recorded, unambiguously verifying the interlayer charge transfer as the origin of the emitted transients. Employing numerical finite-element simulations to accurately predict the influence of the experimental probe geometry and tip dimensions on the near-field interaction has allowed us to extract a characteristic tunneling time of 200 fs for our sample. We have generally found excellent agreement of the theoretically expected and experimentally observed THz emission waveforms even reproducing the reflection at the end of the cantilever.

Despite these intriguing results, the signal amplitudes of the emission experiment are still extremely low and the emission process is insensitive to the decay dynamics following the tunneling process. Therefore, we have employed visible pump/THz probe time-domain spectroscopy to access the full life cycle of photo-induced electron-hole pairs including ultrafast interlayer tunneling and recombination dynamics. Dramat-

ically different behaviors on the TMDC monolayer and heterostructure areas have been observed. The monolayer signal shows a relatively small photo-induced increase in scattering response within 500 fs as unbound electron-hole pairs are generated and intralayer excitons are expected to form. The monolayer scattering response decays within a few picoseconds similar to findings in far-field measurements. In contrast, we have found substantially different dynamics on the heterostructure. Firstly, the heterobilayer signal exhibits a significant delay compared to the monolayer response reaching the maximum pump-induced signal after 1 ps. Secondly, the signal strength drastically exceeds the response of its individual constituent monolayers by up to a factor of 8 and features lifetimes of hundreds of picoseconds indicating the formation of long-lived spatially separated interlayer excitons. We have identified the delayed onset of the heterostructure signal as the time the interlayer tunneling needs for full charge separation almost perfectly agreeing with the tunneling time extracted from THz emission nanoscopy. The differences in signal strength are attributed to the dramatically different polarizabilities of electron-hole pairs confined to a mono-layer or spatially separated over the heterostructure. To verify this hypothesis, we have first determined the polarization sensitivity of the near-field experiment by performing finite-element simulations including again the full tip geometry. A dom-inantly out-of-plane orientation of the electric fields by more than two orders of magnitude in the near-field experiment has been found. Therefore, our measure-ment most likely probes the out-of plane polarizabilty. We have used the results of *ab intio* density functional theory calculations conducted by Dr. Paulo Faria Junior, Dr. Martin Gmitra and Prof. Dr. Jaroslav Fabian to predict the out-of-plane po-larizabilities of intralayer and interlayer electron-hole pairs. The simulations verify the strong increase in polarizability of interlayer electron-hole pairs in the experi-ment reaching up to a factor of 12 for the lowest energy transition when including atomic relaxation. However, for the sake of completeness, it is also known, that the in-plane polarizability of van der Waals materials can exceed typical values of the out-of-plane polarizability by one or two orders of magnitude, and could therefore at least partially compensate for the out-of-plane selectivity of the near-field ex-periment. Therefore, we have investigated the in-plane polarizability of intra- and interlayer excitons by theoretically modeling the exciton with a two-dimensional hy-drogen model and corroborated the prediction by directly extracting the in-plane

polarizability from measurements of their mid-infrared dielectric function in literature. There is a similar substantial increase of more than one order of magnitude in the in-plane polarizability of the interlayer excitons compared to their intralayer counterpart. So in conclusion, the in-plane and out-of-plane polarizability of the interlayer electron-hole pairs is greatly increased compared to the intralayer species. Hence, these results validate our polarization nanoscopy as an ultrafast contact-free probe of tunneling electron-hole pairs that works by monitoring the population of the interlayer species.

Extending the measurement from a single point in space to imaging a whole area, we have performed contact-free nanovideography, investigating the behavior of photo-induced interlayer electron-hole pairs with a spatial resolution better than 50 nm. Doing so, we have resolved substantial differences in formation and recombination dynamics within flat areas of the heterostructure. Variations in interlayer electron-hole pair lifetimes typically ranging from 100 to 250 ps have been observed and an area reaching even lifetimes up to 500 ps has been identified. Close-up images of flat regions of the heterostructure have revealed that even though there are large scale variations between areas of around 400 nm, the interlayer electron-hole pair dynamics are fairly immune to few-nanometer-high local topographic impurities. Therefore, the heterostructure seems to remain intact on the nanoscale with the interlayer formation process likely robust to the subtle changes to the local dielectric environment. We attribute areas of extended lifetime to an advantageous local atomic registry through twist angle or strain. Such hitherto inaccessible local information is essential for the optimization of van der Waals heterostructures and foreshadows the power of using ultrafast terahertz nanoscopy as a contact-free probe of tunneling.

To gain even more insights into the formation dynamics, we have also investigated the interlayer formation and recombination depending on the photo-induced carrier density. Thereby, a saturation behavior and an emerging fast decay channel of the interlayer species have been found for pump fluences higher than $10\,\mu\mathrm{J\,cm^{-2}}$, a possible indication for the reversed field, which is caused by the tunneled carriers, competing with the type-II band alignment of the heterostructure resulting in reduced charge separation. In combination with the nanoscale spatial resolution, this behavior in the high carrier-density limit can be used to reveal local inhomogeneities in the band alignment for different material combinations or stacking angles.

In summary, our approach offers spatiotemporal access to tunneling processes on the relevant length- and timescales without driving external currents – a concept that should readily lend itself to the observation of tunneling in insulating, conducting, or superconducting systems on subcycle timescales. We have demonstrated that the interlayer tunneling processes that govern phase transitions, energy harvesting and light emission in atomically thin heterostructures are now accessible *in situ* on the relevant length- and timescales. Looking forward, this new concept should allow one to investigate and visualize nanoscopic processes in van der Waals heterostructures and help to improve the performance of future atomically thin optoelectronic applications.

While our current configuration in the low THz range is perfectly suited to investigate density-dependent and low-frequency dynamics, shifting the frequency higher into the mid-infrared allows for resonant probing of plasmons and phonons as well as excitonic transitions in van der Waals heterostructures. Therefore, first steps have been taken towards the development of high-power sources for field-resolved mid-infrared nanoscopy. Collaborating with Prof. Dr. Oleg Pronin, a high average-power mid-infrared source has been implemented to generate ultrashort pulses ranging from broadband single-cycle waveforms, which may be applicable for light-wave driven scanning tunneling microscopy to few-cycle pulses with average powers up to 12 mW at a center frequency of 28 THz, which are 20 times more powerful than the probing power used in previous mid-infrared field-resolved near-field studies and should reduce the acquisition time of future experiments manyfold. In collaboration with Dr. Francesco Tani, a novel high-power broadening scheme has been designed employing photonic crystal fibers and allowing for improved spectral broadening for mid-infrared generation. As a result, we have generated few-cycle pulses with average powers of up to 80 mW and pulse durations below 90 fs at a center frequency of 31 to 35 THz that correspond to peak electric fields of several MV/cm in the near-field experiment without including the field enhancement at the tip apex. These pulses allow us to push near-field microscopy to the next level and access nonlinear phenomena [Sch14, Lan16, Sch21]. In addition, the new source could be employed to resonantly probe the dynamics of intra- and interlayer excitons via their $1s$-$2p$-transition on the nanoscale and explore the influence of strong mid-infrared electric fields on the interlayer dynamics, on subcycle timescales.

In the future, a new cryogenic ultra-high vacuum scattering-type near-field micro-scope that is currently being set up will allow for precise control of the experimental conditions down to pressures of 10^{-11} mbar and temperatures of $5\,\text{K}$ combined with excellent optical access for THz and mid-infrared illumination. The absolute control over all experimental parameters and custom-tailored near-field probing tips in combination with high-power mid-infrared and THz radiation will lead to even higher spatial resolution pushing for the single nanometer range. The results of this work alongside the constant improvement of our van der Waals sample quality are the first steps towards exploring the ultrafast interlayer exciton dynamics on het-erostructures with small stacking angles [Tra19, McG20], where the emerging moiré patterns shape the potential energy landscape on single nanometer lengthscales.

Simulation details of the DFT calculation

For the DFT simulations, the electronic structures of the WS_2 and WSe_2 monolayers, and their heterostructure were obtained via the full-potential linearized augmented plane-wave method as implemented in the Wien2k package [Bla20]. The Perdew-Burke-Ernzerhof [Per96] exchange-correlation functional was employed and the D3 correction was used to account for van der Waals interactions in the heterostructure [Gri10]. The wavefunctions are expanded in atomic spheres with orbital quantum numbers up to 10 and the plane-wave cut-off multiplied with the smallest atomic radii is set to 8. For core electrons, spin-orbit coupling was included fully relativistically, while valence electrons were treated within a second-variational procedure with the scalar-relativistic wavefunctions calculated in an energy window up to $5\,Ry$. A Monkhorst-Pack k-grid of 15x15x1 with convergence criteria of $10^{-6}\,e$ for the charge and $10^{-6}\,Ry$ for the energy was used to achieve self-consistency. By adding a zig-zag potential to the exchange-correlation functional [Sta01] with 40 Fourier coefficients, the out-of-plane electric field was included. For the atomic relaxation, the same convergence parameters as discussed before were used combined with a force convergence threshold of $0.1\,mRy/Bohr$.

In-plane and out-of-plane polarizability of TMDC monolayers in literature

A list of current experimentally determined and theoretically predicted values of in- and out-of-plane polarizabilities $\alpha_{\parallel}/\alpha_{\perp}$ in TMDC monolayers is provided in Table B.1. Thereby, the polarizability α is defined by the quadratic energetic shift $\Delta E \propto \frac{1}{2}\alpha F^2$ due to the external electric field F. We include MoS_2 and WSe_2 monolayers, while limiting the polarizabilities to examples with a dielectric environment of $\epsilon \leq 5$ and exciton binding energies of the intralayer excitons larger than $200\,\mathrm{meV}$ to reflect the experimental conditions. Additionally, we compute and list the in-plane polarizability of WSe_2 from [Mer19] (Section 5.2.3.).

While the in-plane polarizabilities (left) show good overall agreement and are in line with the experimental values, the experimentally determined values for the out-of-plane polarizability span across three orders of magnitude. The small intrinsic polarizability of the monolayer and the critical dependence on the dielectric environment as well as the challenging experimental conditions [Roc18, Ver19] are known reasons for the sensitive nature of the experiments. The results of Verzhbitskiy *et al.* [Ver19] are stated as upper limit of the intrinsic polarizability of an isolated monolayer WSe_2, providing values that are comparable to our DFT simulations modeling a WSe_2 monolayer in vacuum for the lowest energy transition and the A-exciton ($0.11\,\mathrm{meV\,nm^2V^{-2}}$ and $0.07\,\mathrm{meV\,nm^2V^{-2}}$, respectively). Accounting for the

atomic relaxation, these values become $0.25\,\mathrm{meV\,nm^2V^{-2}}$ and $0.35\,\mathrm{meV\,nm^2V^{-2}}$, respectively. This large sensitivity of the polarizability to slight changes in the lattice order is in line with the overall extreme susceptibility of the optoelectronic properties of TMDC monolayers to their dielectric environment [Raj19]. Fabrication of a practical monolayer or heterostructure sample on any substrate should increase the polarizability even more [Roc18, Cha19, Kle16] (see Table B.1, right).

Assuming moderate values for in- and out-of-plane polarizability, the dominant out-of-plane sensitivity of near-field microscopy (see Section 5.2.1.) will lead to a contribution of both in- and out-of-plane polarizability to the measured signal. Nevertheless, the drastic increase of the polarizability during the interlayer tunneling is the key feature observed in our experiment and allows for ultrafast contact-free probing of tunneling electron-hole pairs that works by monitoring the population of the interlayer species.

In-plane polarizability		Out-of-plane polarizability	
References	$\alpha_{\parallel}\left(\frac{\mathrm{meVnm^2}}{\mathrm{V^2}}\right)$	References	$\alpha_{\perp}\left(\frac{\mathrm{meVnm^2}}{\mathrm{V^2}}\right)$
[Sch16b], MoS_2, **T**	$8-23\cdot 10^3$	[Kle16], MoS_2, **E**	$2.4\cdot 10^2$
[Ped16], MoS_2, **T**	$6-21\cdot 10^3$	[Cha19], WSe_2, **E**	72
[Ped16], WSe_2, **T**	$5-14\cdot 10^3$	[Roc18], MoS_2, **E**	30
[Mer19], WSe_2, **E**	$3.2\cdot 10^3$	[Ver19], WSe_2, **E**	0.42

Table B.1: Theoretically predicted (T) and experimentally measured (E) values for in- and out-of-plane polarizability of excitons in MoS_2 and WSe_2. For the theoretical predictions the lower and upper limits correspond to smaller and larger dielectric constant of the monolayer environment implemented for example by hBN encapsulation.

Appendix C

Publications

Publications in peer-reviewed journals

- <u>M. Plankl</u>, P. E. Faria Junior, F. Mooshammer, T. Siday, M. Zizlsperger, F. Sandner, F. Schiegl, S. Maier, M. A. Huber, M. Gmitra, J. Fabian, J. L. Boland, T. L. Cocker, and R. Huber
  Subcycle contact-free nanoscopy of ultrafast interlayer transport in atomically thin heterostructures
  Nature Photonics **15**, 594–600 (2021)

- F. Mooshammer, <u>M. Plankl</u>, T. Siday, M. Zizlsperger, F. Sandner, R. Vitalone, R. Jing, M. A. Huber, D. N. Basov, and R. Huber
  Quantitative terahertz emission nanoscopy with multi-resonant near-field probes
  Accepted in Optics Letters **46**, 3572–3575 (2021)

- F. Mooshammer*, M. A. Huber*, F. Sandner, <u>M. Plankl</u>, M. Zizlsperger, and R. Huber (*: these authors contributed equally)
  Quantifying nanoscale electromagnetic fields in near-field microscopy by Fourier demodulation analysis
  ACS Photonics **7**, 344–351 (2020)

- F. Mooshammer, F. Sandner, M. A. Huber, M. Zizlsperger, H. Weigand, <u>M. Plankl</u>, C. Weyrich, M. Lanius, J. Kampmeier, G. Mussler, D. Grützmacher, J. L. Boland, T. L. Cocker, and R. Huber
  Nanoscale near-field tomography of surface states on $(Bi_{0.5}Sb_{0.5})_2Te_3$
  Nano Letters **18**, 7515–7523 (2018)

- M. A. Huber, F. Mooshammer, <u>M. Plankl</u>, L. Viti, F. Sandner, L. Z. Kastner, T. Frank, J. Fabian, M. S. Vitiello, T. L. Cocker, and R. Huber
  Femtosecond photo-switching of interface polaritons in black phosphorus heterostructures
  Nature Nanotechnology **12**, 207–211 (2017)

  This work has been featured in a News and Views article:
  D. N. Basov and M. M. Fogler
  Quantum materials: The quest for ultrafast plasmonics
  Nature Nanotechnology **12**, 187–188 (2017)

- M. A. Huber, <u>M. Plankl</u>, M. Eisele, R. E. Marvel, F. Sandner, T. Korn, C. Schüller, R. F. Haglund, Jr., R. Huber, and T. L. Cocker
  Ultrafast mid-infrared nanoscopy of strained vanadium dioxide nanobeams
  Nano Letters **16**, 1421–1427 (2016)

- M. Eisele, T. L. Cocker, M. A. Huber, <u>M. Plankl</u>, L. Viti, D. Ercolani, L. Sorba, M. S. Vitiello, and R. Huber
  Ultrafast multi-terahertz nano-spectroscopy with sub-cycle temporal resolution
  Nature Photonics **8**, 841–845 (2014)

Publications in international conference proceedings

- M. Zizlsperger, <u>M. Plankl</u>, P. E. Faria Junior, F. Mooshammer, T. Siday, F. Sandner, F. Schiegl, S. Maier, M. A. Huber, M. Gmitra, J. Fabian1, J. L. Boland, T. L. Cocker, and R. Huber
  Femtosecond nano-videography of interlayer charge transfer in van der Waals heterostructures
  CLEO: QELS Fundamental Science 2021, Paper FTu4I.2 (not yet available)

- <u>M. Plankl</u>, M. Zizlsperger, F. Mooshammer, F. Schiegl, F. Sandner, T. Siday, M. A. Huber, J. L. Boland, T. L. Cocker, and R. Huber
  Nanoscopy of ultrafast charge transfer in van der Waals heterostructures
  45th International Conference on Infrared, Millimeter, and Terahertz Waves (IRMMW-THz 2020)
  DOI: 10.1109/IRMMW-THz46771.2020.9370645

- F. Sandner, F. Mooshammer, M. A. Huber, <u>M. Plankl</u>, M. Zizlsperger, and R. Huber
  Quantifying nanoscale electromagnetic fields in multi-THz nanoscopy
  45th International Conference on Infrared, Millimeter, and Terahertz Waves (IRMMW-THz 2020)
  DOI: 10.1109/IRMMW-THz46771.2020.9370598

- M. A. Huber, F. Mooshammer, F. Sandner, <u>M. Plankl</u>, M. Zizlsperger, and R. Huber
  Quantitative Fourier Demodulation Analysis of Nanoscale Electromagnetic Fields in Near-field Microscopy
  CLEO: QELS Fundamental Science 2020, Paper FM3Q.5

- H. Weigand, F. Mooshammer, F. Sandner, M. A. Huber, M. Zizlsperger, <u>M. Plankl</u>, C. Weyrich, M. Lanius, J. Kampmeier, G. Mussler, D. Grützmacher, J. L. Boland, T. L. Cocker, and R. Huber

Nanoscale Spectroscopy of Surface States on a Three-Dimensional Topological
Insulator Frontiers in Optics (FiO), Paper JW3A.121
DOI: 10.1364/FIO.2019.JW3A.121

- F. Mooshammer, F. Sandner, M. A. Huber, M. Zizlsperger, H. Weigand, <u>M. Plankl</u>, C. Weyrich, M. Lanius, J. Kampmeier, G. Mussler, D. Grützmacher, J. L. Boland, T. L. Cocker, and R. Huber
  Mid-infrared nano-tomography of topological insulator surfaces
  44th International Conference on Infrared, Millimeter, and Terahertz Waves (IRMMW-THz 2019)
  DOI: 10.1109/IRMMW-THz.2019.8874358

- F. Mooshammer, F. Sandner, M. A. Huber, M. Zizlsperger, H. Weigand, <u>M. Plankl</u>, C. Weyrich, M. Lanius, J. Kampmeier, G. Mussler, D. Grützmacher, J. L. Boland, T. L. Cocker, and R. Huber
  Nanoscale mid-infrared near-field tomography of topological insulator surfaces
  Conference on Lasers and Electro-Optics (CLEO) Europe, Paper eg-3.4

- F. Sandner, F. Mooshammer, M. A. Huber, M. Zizlsperger, H. Weigand, <u>M. Plankl</u>, C. Weyrich, M. Lanius, J. Kampmeier, G. Mussler, D. Grützmacher, J. L. Boland, T. L. Cocker, and R. Huber
  Near-field tomography and spectroscopy of surface states on a three-dimensional topological insulator CLEO: QELS Fundamental Science 2019, Paper FTh4C.3
  DOI: 10.1364/CLEO_QELS.2019.FTh4C.3

- T. L. Cocker, D. Peller, M. A. Huber, F. Mooshammer, <u>M. Plankl</u>, F. Sandner, L. Viti, M. S. Vitiello, J. Repp, and R. Huber
  Terahertz Microscopy Down To The Atomic Scale (plenary talk)
  43rd International Conference on Infrared, Millimeter, and Terahertz Waves (IRMMW-THz 2018)
  DOI: 10.1109/IRMMW-THz.2018.8509936

- M. A. Huber, F. Mooshammer, <u>M. Plankl</u>, L. Viti, F. Sandner, L. Z. Kastner, T. Frank, J. Fabian, M. S. Vitiello, T. L. Cocker, and R. Huber
  Femtosecond switch-on of hybrid polaritons in black phosphorus heterostructures
  42nd International Conference on Infrared, Millimeter, and Terahertz Waves (IRMMW-THz 2017)
  DOI: 10.1109/IRMMW-THz.2017.8066876

- R. Huber, F. Langer, S. Baierl, U. Huttner, S. W. Koch, M. Kira, M. A. Huber, F. Mooshammer, <u>M. Plankl</u>, D. Peller, T. L. Cocker, and J. Repp
  Terahertz subcycle control: from high-harmonic generation to molecular snapshots
  Nonlinear Optics: Materials, Fundamentals and Applications, Paper NW2A.5
  DOI: 10.1364/NLO.2017.NW2A.5

- F. Mooshammer, M. A. Huber, <u>M. Plankl</u>, L. Viti, F. Sandner, L. Z. Kastner, T. Frank, J. Fabian, M. S. Vitiello, T. L. Cocker, and R. Huber
  Ultrafast photo-activation of interface polaritons in black phosphorus heterostructures
  CLEO/Europe-EQEC, Paper EH_1_2
  DOI: 10.1109/CLEOE-EQEC.2017.8087633

- M. A. Huber, F. Mooshammer, <u>M. Plankl</u>, L. Viti, F. Sandner, L. Z. Kastner, T. Frank, J. Fabian, M. S. Vitiello, T. L. Cocker, and R. Huber
  Ultrafast Photo-activation of Surface Polaritons in Black Phosphorus Heterostructures
  CLEO: QELS Fundamental Science, Paper FF2F.3
  DOI: 10.1364/CLEO_QELS.2017.FF2F.3

- T. L. Cocker, M. A. Huber, M. Eisele, <u>M. Plankl</u>, L. Viti, R. E. Marvel, F. Sandner, F. Mooshammer, T. Korn, C. Schüller, D. Ercolani, L. Sorba, R. F. Haglund, M. S. Vitiello, and R. Huber
  Taking sub-cycle THz nanoscopy to the limits
  CLEO: Science and Innovations, Paper SW1L.4
  DOI: 10.1364/CLEO_SI.2016.SW1L.4

Contributions at international conferences as presenting author:

- <u>M. Plankl</u>, M. Zizlsperger, F. Mooshammer, F. Schiegl, F. Sandner, T. Siday, M. A. Huber, J. L. Boland, T. L. Cocker, and R. Huber
  Nanoscopy of ultrafast charge transfer in van der Waals heterostructures
  45th International Conference on Infrared, Millimeter, and Terahertz Waves (IRMMW-THz 2020)
  November 2020
  This contribution was selected as the third place in the "Outstanding Student Paper"-award competition among more than 200 applications

- <u>M. Plankl</u>, M. Zizlsperger, F. Mooshammer, F. Schiegl, F. Sandner, M. A. Huber, T. Siday, J. L. Boland, T. L. Cocker and R. Huber
  Mapping nanoscale charge carrier dynamics in van der Waals heterostructures by ultrafast terahertz nanoscopy Winter School on Ultrafast Processes in Condensed Matter (WUPCOM) 2020
  March 2020

- <u>M. Plankl</u>, M. Zizlsperger, F. Schiegl, F. Mooshammer, F. Sandner, M. A. Huber, J. L. Boland, T. L. Cocker and R. Huber
  Tracing Light-Matter Coupling on the Nanometer Length and the Femtosecond Timescale
  9th Ninth Week of the Young Researcher, Quantum Science: Light-Matter Interaction

Bibliography

[Abb73] E. Abbe, *Beiträge zur Theorie des Mikroskops und der mikroskopischen Wahrnehmung*, Archiv für mikroskopische Anatomie **9**, 413–468 (1873).

[Abb08] D. Abbott, P. C. W. Davies, A. K. Pati, and S. R. Penrose, *Quantum Aspects of Life*, Imperial College Press, 2008.

[AG17] P. Alonso-González, A. Y. Nikitin, Y. Gao, A. Woessner, M. B. Lundeberg, A. Principi, N. Forcellini, W. Yan, S. Vélez, A. J. Huber, K. Watanabe, T. Taniguchi, F. Casanova, L. E. Hueso, M. Polini, J. Hone, F. H. Koppens, and R. Hillenbrand, *Acoustic terahertz graphene plasmons revealed by photocurrent nanoscopy*, Nature Nanotechnology **12**, 31–35 (2017).

[Ahm17] S. Ahmed and J. Yi, *Two-Dimensional Transition Metal Dichalcogenides and Their Charge Carrier Mobilities in Field-Effect Transistors*, Nano-Micro Letters **9**, 50 (2017).

[Aiz08] J. Aizpurua, T. Taubner, F. J. García de Abajo, M. Brehm, and R. Hillenbrand, *Substrate-enhanced infrared near-field spectroscopy*, Optics Express **16**, 1529 (2008).

[Ans18] N. Ansari and F. Ghorbani, *Light absorption optimization in two-dimensional transition metal dichalcogenide van der Waals heterostructures*, Journal of the Optical Society of America B **35**, 1179 (2018).

[Ash72] E. A. Ash and G. Nicholls, *Super-resolution Aperture Scanning Microscope*, Nature **237**, 510–512 (1972).

[Aus00] J. Aus der Au, G. J. Spühler, T. Südmeyer, R. Paschotta, R. Hövel, M. Moser, S. Erhard, M. Karszewski, A. Giesen, and U. Keller, *16.2-W average power from a diode-pumped femtosecond Yb:YAG thin disk laser*, Optics Letters **25**, 859 (2000).

[Bab17] V. E. Babicheva, S. Gamage, M. I. Stockman, and Y. Abate, *Near-field edge fringes at sharp material boundaries*, Optics Express **25**, 23935 (2017).

[Bac09] G. Bacciagaluppi and A. Valentini, *Quantum Theory at the Crossroads*, vol. 63, Cambridge University Press, Cambridge, 2009.

[Bai16] S. Baierl, M. Hohenleutner, T. Kampfrath, A. K. Zvezdin, A. V. Kimel, R. Huber, and R. V. Mikhaylovskiy, *Nonlinear spin control by terahertz-driven anisotropy fields*, Nature Photonics **10**, 715–718 (2016).

[Bai20] Y. Bai, L. Zhou, J. Wang, W. Wu, L. J. McGilly, D. Halbertal, C. F. B. Lo, F. Liu, J. Ardelean, P. Rivera, N. R. Finney, X. C. Yang, D. N. Basov, W. Yao, X. Xu, J. Hone, A. N. Pasupathy, and X. Y. Zhu, *Excitons in strain-induced one-dimensional moiré potentials at transition metal dichalcogenide heterojunctions*, Nature Materials **19**, 1068–1073 (2020).

[Bao15] W. Bao, N. J. Borys, C. Ko, J. Suh, W. Fan, A. Thron, Y. Zhang, A. Buyanin, J. Zhang, S. Cabrini, P. D. Ashby, A. Weber-Bargioni, S. Tongay, S. Aloni, D. F. Ogletree, J. Wu, M. B. Salmeron, and P. J. Schuck, *Visualizing nanoscale excitonic relaxation properties of disordered edges and grain boundaries in monolayer molybdenum disulfide*, Nature Communications **6**, 7993 (2015).

[Bar68] A. S. Barker, *Dielectric dispersion and phonon line shape in gallium phosphide*, Physical Review **165**, 917–922 (1968).

[Bar17] M. Baranowski, A. Surrente, L. Klopotowski, J. M. Urban, N. Zhang, D. K. Maude, K. Wiwatowski, S. Mackowski, Y. C. Kung, D. Dumcenco, A. Kis, and P. Plochocka, *Probing the Interlayer Exciton Physics in a*

$MoS_2/MoSe_2/MoS_2$ *van der Waals Heterostructure*, Nano Letters **17**, 6360–6365 (2017).

[Bau13] B. W. H. Baugher, H. O. H. Churchill, Y. Yang, and P. Jarillo-Herrero, *Intrinsic Electronic Transport Properties of High-Quality Monolayer and Bilayer MoS_2*, Nano Letters **13**, 4212–4216 (2013).

[Bel80] R. P. Bell, *The Tunnel Effect in Chemistry*, Springer US, Boston, MA, 1980.

[Bet86] E. Betzig, A. Lewis, A. Harootunian, M. Isaacson, and E. Kratschmer, *Near Field Scanning Optical Microscopy (NSOM)*, Biophysical Journal **49**, 269–279 (1986).

[Bin82] G. Binnig, H. Rohrer, C. Gerber, and E. Weibel, *Tunneling through a controllable vacuum gap*, Applied Physics Letters **40**, 178–180 (1982).

[Bin83] G. Binnig, H. Rohrer, C. Gerber, and E. Weibel, *7×7 Reconstruction on Si(111) Resolved in Real Space*, Physical Review Letters **50**, 120–123 (1983).

[Bin85] G. Binnig and H. Rohrer, *Scanning tunneling microscopy*, Surface Science **152-153**, 17–26 (1985).

[Bla20] P. Blaha, K. Schwarz, F. Tran, R. Laskowski, G. K. H. Madsen, and L. D. Marks, *WIEN2k: An APW+lo program for calculating the properties of solids*, The Journal of Chemical Physics **152**, 074101 (2020).

[Boh01] J. L. Bohn, D. J. Nesbitt, and A. Gallagher, *Field enhancement in apertureless near-field scanning optical microscopy*, Journal of the Optical Society of America A **18**, 2998 (2001).

[Boy08] R. W. Boyd, *Nonlinear Optics, Third Edition*, 3rd ed., Academic Press, Inc., USA, 2008.

[Bre08] M. Brehm, A. Schliesser, F. Cajko, I. Tsukerman, and F. Keilmann, *Antenna-mediated back-scattering efficiency in infrared near-field microscopy*, Optics Express **16**, 11203 (2008).

[Bro72] R. A. Bromley, R. B. Murray, and A. D. Yoffe, *The band structures of some transition metal dichalcogenides. III. Group VIA: trigonal prism materials*, Journal of Physics C: Solid State Physics **5**, 759–778 (1972).

[Bro17] J. C. Brookes, *Quantum effects in biology: golden rule in enzymes, olfaction, photosynthesis and magnetodetection*, Proceedings of the Royal Society A: Mathematical, Physical and Engineering Sciences **473**, 20160822 (2017).

[Cao18a] Y. Cao, V. Fatemi, A. Demir, S. Fang, S. L. Tomarken, J. Y. Luo, J. D. Sanchez-Yamagishi, K. Watanabe, T. Taniguchi, E. Kaxiras, R. C. Ashoori, and P. Jarillo-Herrero, *Correlated insulator behaviour at half-filling in magic-angle graphene superlattices*, Nature **556**, 80–84 (2018).

[Cao18b] Y. Cao, V. Fatemi, S. Fang, K. Watanabe, T. Taniguchi, E. Kaxiras, and P. Jarillo-Herrero, *Unconventional superconductivity in magic-angle graphene superlattices*, Nature **556**, 43–50 (2018).

[Ceb14] F. Ceballos, M. Z. Bellus, H. Y. Chiu, and H. Zhao, *Ultrafast charge separation and indirect exciton formation in a MoS_2-$MoSe_2$ van der Waals heterostructure*, ACS Nano **8**, 12717–12724 (2014).

[CG14] A. Castellanos-Gomez, M. Buscema, R. Molenaar, V. Singh, L. Janssen, H. S. J. van der Zant, and G. A. Steele, *Deterministic transfer of two-dimensional materials by all-dry viscoelastic stamping*, 2D Materials **1**, 011002 (2014).

[Cha19] C. Chakraborty, A. Mukherjee, L. Qiu, and A. N. Vamivakas, *Electrically tunable valley polarization and valley coherence in monolayer WSe_2 embedded in a van der Waals heterostructure*, Optical Materials Express **9**, 1479 (2019).

[Che03] H.-T. Chen, R. Kersting, and G. C. Cho, *Terahertz imaging with nanometer resolution*, Applied Physics Letters **83**, 3009–3011 (2003).

[Che04] H.-T. Chen, S. Kraatz, G. C. Cho, and R. Kersting, *Identification of a Resonant Imaging Process in Apertureless Near-Field Microscopy*, Physical Review Letters **93**, 267401 (2004).

[Che12] T. Cheiwchanchamnangij and W. R. L. Lambrecht, *Quasiparticle band structure calculation of monolayer, bilayer, and bulk MoS$_2$*, Physical Review B **85**, 205302 (2012).

[Che14a] R. Cheng, D. Li, H. Zhou, C. Wang, A. Yin, S. Jiang, Y. Liu, Y. Chen, Y. Huang, and X. Duan, *Electroluminescence and photocurrent generation from atomically sharp WSe$_2$/MoS$_2$ heterojunction p-n diodes*, Nano Letters **14**, 5590–5597 (2014).

[Che14b] A. Chernikov, T. C. Berkelbach, H. M. Hill, A. Rigosi, Y. Li, O. B. Aslan, D. R. Reichman, M. S. Hybertsen, and T. F. Heinz, *Exciton binding energy and nonhydrogenic Rydberg series in monolayer WS$_2$*, Physical Review Letters **113**, 076802 (2014).

[Che15] A. Chernikov, C. Ruppert, H. M. Hill, A. F. Rigosi, and T. F. Heinz, *Population inversion and giant bandgap renormalization in atomically thin WS$_2$ layers*, Nature Photonics **9**, 466–470 (2015).

[Che19a] G. Chen, A. L. Sharpe, P. Gallagher, I. T. Rosen, E. J. Fox, L. Jiang, B. Lyu, H. Li, K. Watanabe, T. Taniguchi, J. Jung, Z. Shi, D. Goldhaber-Gordon, Y. Zhang, and F. Wang, *Signatures of tunable superconductivity in a trilayer graphene moiré superlattice*, Nature **572**, 215–219 (2019).

[Che19b] X. Chen, D. Hu, R. Mescall, G. You, D. N. Basov, Q. Dai, and M. Liu, *Modern Scattering-Type Scanning Near-Field Optical Microscopy for Advanced Material Research*, Advanced Materials **31**, 1804774 (2019).

[Coc13] T. L. Cocker, V. Jelic, M. Gupta, S. J. Molesky, J. A. J. Burgess, G. D. L. Reyes, L. V. Titova, Y. Y. Tsui, M. R. Freeman, and F. A. Hegmann, *An ultrafast terahertz scanning tunnelling microscope*, Nature Photonics **7**, 620–625 (2013).

[Coc16] T. L. Cocker, D. Peller, P. Yu, J. Repp, and R. Huber, *Tracking the ultrafast motion of a single molecule by femtosecond orbital imaging*, Nature **539**, 263–267 (2016).

[Cro04] W. J. Croft, *Under the microscpe: A brief history of microscopy*, World Scientific Publishing Co. Pte. Ltd, 2004.

[Cvi07] A. Cvitkovic, N. Ocelic, and R. Hillenbrand, *Analytical model for quantitative prediction of material contrasts in scattering-type near-field optical microscopy*, Optics Express **15**, 8550 (2007).

[Dai14] S. Dai, Z. Fei, Q. Ma, A. S. Rodin, M. Wagner, A. S. McLeod, M. K. Liu, W. Gannett, W. Regan, K. Watanabe, T. Taniguchi, M. Thiemens, G. Dominguez, A. H. C. Neto, A. Zettl, F. Keilmann, P. Jarillo-Herrero, M. M. Fogler, and D. N. Basov, *Tunable Phonon Polaritons in Atomically Thin van der Waals Crystals of Boron Nitride*, Science **343**, 1125–1129 (2014).

[Dhi17] S. S. Dhillon, M. S. Vitiello, E. H. Linfield, A. G. Davies, M. C. Hoffmann, J. Booske, C. Paoloni, M. Gensch, P. Weightman, G. P. Williams, E. Castro-Camus, D. R. S. Cumming, F. Simoens, I. Escorcia-Carranza, J. Grant, S. Lucyszyn, M. Kuwata-Gonokami, K. Konishi, M. Koch, C. A. Schmuttenmaer, T. L. Cocker, R. Huber, A. G. Markelz, Z. D. Taylor, V. P. Wallace, J. Axel Zeitler, J. Sibik, T. M. Korter, B. Ellison, S. Rea, P. Goldsmith, K. B. Cooper, R. Appleby, D. Pardo, P. G. Huggard, V. Krozer, H. Shams, M. Fice, C. Renaud, A. Seeds, A. Stöhr, M. Naftaly, N. Ridler, R. Clarke, J. E. Cunningham, and M. B. Johnston, *The 2017 terahertz science and technology roadmap*, Journal of Physics D: Applied Physics **50**, 043001 (2017).

[Dic23] R. G. Dickinson and L. Pauling, *The crystal structure of molybdenite*, Journal of the American Chemical Society **45**, 1466–1471 (1923).

[Dür86] U. Dürig, D. W. Pohl, and F. Rohner, *Near-field optical-scanning microscopy*, Journal of Applied Physics **59**, 3318–3327 (1986).

[Eis14] M. Eisele, T. L. Cocker, M. A. Huber, M. Plankl, L. Viti, D. Ercolani, L. Sorba, M. S. Vitiello, and R. Huber, *Ultrafast multi-terahertz nano-spectroscopy with sub-cycle temporal resolution*, Nature Photonics **8**, 841–845 (2014).

[Erm19] A. Ermolov, C. Heide, P. Dienstbier, F. Köttig, F. Tani, P. Hommelhoff, and P. S. Russell, *Carrier-envelope-phase-stable soliton-based pulse compression to 44 fs and ultraviolet generation at the 800 kHz repetition rate*, Optics Letters **44**, 5005 (2019).

[Esa73] L. Esaki, *Long Journey into Tunneling*, Nobel Lecture (1973).

[Est07] R. Esteban, R. Vogelgesang, and K. Kern, *Tip-substrate interaction in optical near-field microscopy*, Physical Review B **75**, 195410 (2007).

[Far19] P. E. Faria Junior, M. Kurpas, M. Gmitra, and J. Fabian, *k · p theory for phosphorene: Effective g-factors, Landau levels, and excitons*, arXiv **100**, 115203 (2019).

[Fei12] Z. Fei, A. S. Rodin, G. O. Andreev, W. Bao, A. S. McLeod, M. Wagner, L. M. Zhang, Z. Zhao, M. Thiemens, G. Dominguez, M. M. Fogler, A. H. C. Neto, C. N. Lau, F. Keilmann, and D. N. Basov, *Gate-tuning of graphene plasmons revealed by infrared nano-imaging*, Nature **487**, 82–85 (2012).

[Fio14] G. Fiori, F. Bonaccorso, G. Iannaccone, T. Palacios, D. Neumaier, A. Seabaugh, S. K. Banerjee, and L. Colombo, *Electronics based on two-dimensional materials*, Nature Nanotechnology **9**, 768–779 (2014).

[Fog14] M. M. Fogler, L. V. Butov, and K. S. Novoselov, *High-temperature superfluidity with indirect excitons in van der Waals heterostructures*, Nature Communications **5**, 4555 (2014).

[Fre31] J. Frenkel, *On the Transformation of Light into Heat in Solids. II*, Physical Review **37**, 1276–1294 (1931).

[Fur14] M. M. Furchi, A. Pospischil, F. Libisch, J. Burgdörfer, and T. Mueller, *Photovoltaic effect in an electrically tunable Van der Waals heterojunction*, Nano Letters **14**, 4785–4791 (2014).

[Gal99] G. Gallot and D. Grischkowsky, *Electro-optic detection of terahertz radiation*, Journal of the Optical Society of America B **16**, 1204 (1999).

[Gam28] G. Gamow, *Zur Quantentheorie des Atomkernes*, Zeitschrift für Physik **51**, 204–212 (1928).

[Gar20] M. Garg and K. Kern, *Attosecond coherent manipulation of electrons in tunneling microscopy*, Science **367**, 411–415 (2020).

[Gie94] A. Giesen, H. Hügel, A. Voss, K. Wittig, U. Brauch, and H. Opower, *Scalable concept for diode-pumped high-power solid-state lasers*, Applied Physics B **58**, 365–372 (1994).

[Gmi09] M. Gmitra, S. Konschuh, C. Ertler, C. Ambrosch-Draxl, and J. Fabian, *Band-structure topologies of graphene: Spin-orbit coupling effects from first principles*, Physical Review B **80**, 235431 (2009).

[Gmi13] M. Gmitra, D. Kochan, and J. Fabian, *Spin-Orbit Coupling in Hydrogenated Graphene*, Physical Review Letters **110**, 246602 (2013).

[Gmi15] M. Gmitra and J. Fabian, *Graphene on transition-metal dichalcogenides: A platform for proximity spin-orbit physics and optospintronics*, Physical Review B **92**, 155403 (2015).

[Gmi17] M. Gmitra and J. Fabian, *Proximity Effects in Bilayer Graphene on Monolayer WSe_2: Field-Effect Spin Valley Locking, Spin-Orbit Valve, and Spin Transistor*, Physical Review Letters **119**, 146401 (2017).

[Gon13] C. Gong, H. Zhang, W. Wang, L. Colombo, R. M. Wallace, and K. Cho, *Band alignment of two-dimensional transition metal dichalcogenides: Application in tunnel field effect transistors*, Applied Physics Letters **103**, 053513 (2013).

[Gon17] C. Gong, L. Li, Z. Li, H. Ji, A. Stern, Y. Xia, T. Cao, W. Bao, C. Wang, Y. Wang, Z. Q. Qiu, R. J. Cava, S. G. Louie, J. Xia, and X. Zhang, *Discovery of intrinsic ferromagnetism in two-dimensional van der Waals crystals*, Nature **546**, 265–269 (2017).

[Got12] T. Gottwald, C. Stolzenburg, D. Bauer, J. Kleinbauer, V. Kuhn, T. Metzger, S. Schad, D. Sutter, and A. Killi, *Recent disk laser development at Trumpf*, High-Power Lasers 2012: Technology and Systems (H. Ackermann and W. L. Bohn, eds.), nov 2012, p. 85470C.

[Gov13] A. A. Govyadinov, I. Amenabar, F. Huth, P. S. Carney, and R. Hillenbrand, *Quantitative Measurement of Local Infrared Absorption and Dielectric Function with Tip-Enhanced Near-Field Microscopy*, The Journal of Physical Chemistry Letters **4**, 1526–1531 (2013).

[Gov14] A. A. Govyadinov, S. Mastel, F. Golmar, A. Chuvilin, P. S. Carney, and R. Hillenbrand, *Recovery of permittivity and depth from near-field data as a step toward infrared nanotomography*, ACS Nano **8**, 6911–6921 (2014).

[Gra19] I. J. Graumann, F. Saltarelli, L. Lang, V. J. Wittwer, T. Südmeyer, C. R. Phillips, and U. Keller, *Power-scaling of nonlinear-mirror modelocked thin-disk lasers*, Optics Express **27**, 37349 (2019).

[Gri10] S. Grimme, J. Antony, S. Ehrlich, and H. Krieg, *A consistent and accurate ab initio parametrization of density functional dispersion correction (DFT-D) for the 94 elements H-Pu*, Journal of Chemical Physics **132**, 154104 (2010).

[Gri18] D. J. Griffiths and D. F. Schroeter, *Introduction to Quantum Mechanics*, Cambridge University Press, 2018.

[Gun00] M. K. Gunde, *Vibrational modes in amorphous silicon dioxide*, Physica B: Condensed Matter **292**, 286–295 (2000).

[Hal20] M. Halbhuber, J. Mornhinweg, V. Zeller, C. Ciuti, D. Bougeard, R. Huber, and C. Lange, *Non-adiabatic stripping of a cavity field from electrons in the deep-strong coupling regime*, Nature Photonics **14**, 675–679 (2020).

[Hau12] B. Hauer, A. P. Engelhardt, and T. Taubner, *Quasi-analytical model for scattering infrared near-field microscopy on layered systems*, Optics Express **20**, 13173 (2012).

[He14] K. He, N. Kumar, L. Zhao, Z. Wang, K. F. Mak, H. Zhao, and J. Shan, *Tightly bound excitons in monolayer WSe$_2$*, Physical Review Letters **113**, 026803 (2014).

[Hec00] B. Hecht, B. Sick, U. P. Wild, V. Deckert, R. Zenobi, O. J. F. Martin, and D. W. Pohl, *Scanning near-field optical microscopy with aperture probes: Fundamentals and applications*, The Journal of Chemical Physics **112**, 7761–7774 (2000).

[Hei69] W. Heisenberg, *Der Teil und das Ganze : Gespräche im Umkreis d. Atomphysik. Werner Heisenberg*, Piper Verlag Gmbh, 1969.

[Hei71] W. Heisenberg, *Physics and Beyond*, George Allen & Unwin Ltd., 1971.

[Her12] G. Herink, D. R. Solli, M. Gulde, and C. Ropers, *Field-driven photoemission from nanostructures quenches the quiver motion*, Nature **483**, 190–193 (2012).

[Hil00] R. Hillenbrand and F. Keilmann, *Complex optical constants on a subwavelength scale*, Physical Review Letters **85**, 3029–3032 (2000).

[Hil02] R. Hillenbrand, T. Taubner, and F. Keilmann, *Phonon-enhanced light-matter interaction at the nanometre scale*, Nature **418**, 159–162 (2002).

[Hil16] H. M. Hill, A. F. Rigosi, K. T. Rim, G. W. Flynn, and T. F. Heinz, *Band Alignment in MoS$_2$/WS$_2$ Transition Metal Dichalcogenide Heterostructures Probed by Scanning Tunneling Microscopy and Spectroscopy*, Nano Letters **16**, 4831–4837 (2016).

[Hir20] A. Hirohata, K. Yamada, Y. Nakatani, I.-L. Prejbeanu, B. Diény, P. Pirro, and B. Hillebrands, *Review on spintronics: Principles and device applications*, Journal of Magnetism and Magnetic Materials **509**, 166711 (2020).

[Hon14] X. Hong, J. Kim, S.-F. Shi, Y. Zhang, C. Jin, Y. Sun, S. Tongay, J. Wu, Y. Zhang, and F. Wang, *Ultrafast charge transfer in atomically thin MoS$_2$/WS$_2$ heterostructures*, Nature Nanotechnology **9**, 682–686 (2014).

154

[Hua17] B. Huang, G. Clark, E. Navarro-Moratalla, D. R. Klein, R. Cheng, K. L. Seyler, D. Zhong, E. Schmidgall, M. A. McGuire, D. H. Cobden, W. Yao, D. Xiao, P. Jarillo-Herrero, and X. Xu, *Layer-dependent ferromagnetism in a van der Waals crystal down to the monolayer limit*, Nature **546**, 270–273 (2017).

[Hub00] R. Huber, *Femtosekunden-lmpulse im Mittelinfrarot: Abstimmbare Erzeugung, feldaufgelöste Detektion und erste Anwendungen*, Diploma Thesis, 2000 (Available on private request via markus.plankl@ur.de).

[Hub01] R. Huber, F. Tauser, A. Brodschelm, M. Bichler, G. Abstreiter, and A. Leitenstorfer, *How many-particle interactions develop after ultrafast excitation of an electron-hole plasma*, Nature **414**, 286–289 (2001).

[Hub06] A. Huber, N. Ocelic, T. Taubner, and R. Hillenbrand, *Nanoscale resolved infrared probing of crystal structure and of plasmon-phonon coupling*, Nano Letters **6**, 774–778 (2006).

[Hub08] A. J. Huber, F. Keilmann, J. Wittborn, J. Aizpurua, and R. Hillenbrand, *Terahertz near-field nanoscopy of mobile carriers in single semiconductor nanodevices*, Nano Letters **8**, 3766–3770 (2008).

[Hub16] M. A. Huber, M. Plankl, M. Eisele, R. E. Marvel, F. Sandner, T. Korn, C. Schüller, R. F. Haglund, R. Huber, and T. L. Cocker, *Ultrafast Mid-Infrared Nanoscopy of Strained Vanadium Dioxide Nanobeams*, Nano Letters **16**, 1421–1427 (2016).

[Hub17] M. A. Huber, F. Mooshammer, M. Plankl, L. Viti, F. Sandner, L. Z. Kastner, T. Frank, J. Fabian, M. S. Vitiello, T. L. Cocker, and R. Huber, *Femtosecond photo-switching of interface polaritons in black phosphorus heterostructures*, Nature Nanotechnology **12**, 207–211 (2017).

[Hun27] F. Hund, *Zur Deutung der Molekelspektren. I*, Zeitschrift für Physik **40**, 742–764 (1927).

[Hun09] S. Hunklinger, *Festkörperphysik*, Oldenbourg Verlag München, 2009.

[Irm15] S. Irmer, T. Frank, S. Putz, M. Gmitra, D. Kochan, and J. Fabian, *Spin-orbit coupling in fluorinated graphene*, Physical Review B **91**, 115141 (2015).

[Jan20] T. Janda, J. Godinho, T. Ostatnicky, E. Pfitzner, G. Ulrich, A. Hoehl, S. Reimers, Z. Šobáň, T. Metzger, H. Reichlová, V. Novák, R. P. Campion, J. Heberle, P. Wadley, K. W. Edmonds, O. J. Amin, J. S. Chauhan, S. S. Dhesi, F. Maccherozzi, R. M. Otxoa, P. E. Roy, K. Olejník, P. Němec, T. Jungwirth, B. Kaestner, and J. Wunderlich, *Magneto-Seebeck microscopy of domain switching in collinear antiferromagnet CuMnAs*, Physical Review Materials **4**, 094413 (2020).

[Jar14] D. Jariwala, V. K. Sangwan, L. J. Lauhon, T. J. Marks, and M. C. Hersam, *Emerging Device Applications for Semiconducting Two-Dimensional Transition Metal Dichalcogenides*, ACS Nano **8**, 1102–1120 (2014).

[Jau19] L. A. Jauregui, A. Y. Joe, K. Pistunova, D. S. Wild, A. A. High, Y. Zhou, G. Scuri, K. De Greve, A. Sushko, C.-H. Yu, T. Taniguchi, K. Watanabe, D. J. Needleman, M. D. Lukin, H. Park, and P. Kim, *Electrical control of interlayer exciton dynamics in atomically thin heterostructures*, Science **366**, 870–875 (2019).

[Jel17] V. Jelic, K. Iwaszczuk, P. H. Nguyen, C. Rathje, G. J. Hornig, H. M. Sharum, J. R. Hoffman, M. R. Freeman, and F. A. Hegmann, *Ultrafast terahertz control of extreme tunnel currents through single atoms on a silicon surface*, Nature Physics **13**, 591–598 (2017).

[Jia19] T. Jiang, V. Kravtsov, M. Tokman, A. Belyanin, and M. B. Raschke, *Ultrafast coherent nonlinear nanooptics and nanoimaging of graphene*, Nature Nanotechnology **14**, 838–843 (2019).

[Jia21] X. Jiang, C. Shi, Z. Li, S. Wang, Y. Wang, S. Yang, S. G. Louie, and X. Zhang, *Direct observation of Klein tunneling in phononic crystals*, Science **370**, 1447–1450 (2021).

[Jin18] C. Jin, J. Kim, M. Iqbal Bakti Utama, E. C. Regan, H. Kleemann, H. Cai, Y. Shen, M. J. Shinner, A. Sengupta, K. Watanabe, T. Taniguchi, S. Tongay, A. Zettl, and F. Wang, *Imaging of pure spin-valley diffusion current in WS_2-WSe_2 heterostructures*, Science **360**, 893–896 (2018).

[Joh02] M. B. Johnston, D. M. Whittaker, A. Corchia, A. G. Davies, and E. H. Linfield, *Simulation of terahertz generation at semiconductor surfaces*, Physical Review B **65**, 165301 (2002).

[Jun16] T. Jungwirth, X. Marti, P. Wadley, and J. Wunderlich, *Antiferromagnetic spintronics*, Nature Nanotechnology **11**, 231–241 (2016).

[Kah67] D. Kahng and S. M. Sze, *A Floating Gate and Its Application to Memory Devices*, Bell System Technical Journal **46**, 1288–1295 (1967).

[Kam07] T. Kampfrath, J. Nötzold, and M. Wolf, *Sampling of broadband terahertz pulses with thick electro-optic crystals*, Applied Physics Letters **90**, 1–4 (2007).

[Kan99] D. J. Kane, *Recent progress toward real-time measurement of ultrashort laser pulses*, IEEE Journal of Quantum Electronics **35**, 421–431 (1999).

[Kan13] J. Kang, S. Tongay, J. Zhou, J. Li, and J. Wu, *Band offsets and heterostructures of two-dimensional semiconductors*, Applied Physics Letters **102**, 012111 (2013).

[Kel03] U. Keller, *Recent developments in compact ultrafast lasers*, Nature **424**, 831–838 (2003).

[Ken21] D. M. Kennes, M. Claassen, L. Xian, A. Georges, A. J. Millis, J. Hone, C. R. Dean, D. N. Basov, A. N. Pasupathy, and A. Rubio, *Moiré heterostructures as a condensed-matter quantum simulator*, Nature Physics **17**, 155–163 (2021).

[Kim12] D.-S. Kim and Z. H. Kim, *Role of in-plane polarizability of the tip in scattering near-field microscopy of a plasmonic nanoparticle*, Optics Express **20**, 8689 (2012).

[Kla17] P. Klarskov, H. Kim, V. L. Colvin, and D. M. Mittleman, *Nanoscale Laser Terahertz Emission Microscopy*, ACS Photonics **4**, 2676–2680 (2017).

[Kle16] J. Klein, J. Wierzbowski, A. Regler, J. Becker, F. Heimbach, K. Müller, M. Kaniber, and J. J. Finley, *Stark Effect Spectroscopy of Mono- and Few-Layer MoS_2*, Nano Letters **16**, 1554–1559 (2016).

[Kle18] D. R. Klein, D. MacNeill, J. L. Lado, D. Soriano, E. Navarro-Moratalla, K. Watanabe, T. Taniguchi, S. Manni, P. Canfield, J. Fernández-Rossier, and P. Jarillo-Herrero, *Probing magnetism in 2D van der Waals crystalline insulators via electron tunneling*, Science **360**, 1218–1222 (2018).

[Kli07] C. F. Klingshirn, *Semiconductor Optics*, 3 ed., Springer, 2007.

[Kno32] M. Knoll and E. Ruska, *Das Elektronenmikroskop*, Zeitschrift für Physik **78**, 318–339 (1932).

[Kno99] B. Knoll and F. Keilmann, *Near-field probing of vibrational absorption for chemical microscopy*, Nature **399**, 134–137 (1999).

[Kno00] B. Knoll and F. Keilmann, *Enhanced dielectric contrast in scattering-type scanning near-field optical microscopy*, Optics Communications **182**, 321–328 (2000).

[Kno17] M. Knorr, J. Raab, M. Tauer, P. Merkl, D. Peller, E. Wittmann, E. Riedle, C. Lange, and R. Huber, *Phase-locked multi-terahertz electric fields exceeding 13 MV/cm at a 190 kHz repetition rate*, Optics Letters **42**, 4367 (2017).

[Kno18] M. Knorr, P. Steinleitner, J. Raab, I. Gronwald, P. Merkl, C. Lange, and R. Huber, *Ultrabroadband etalon-free detection of infrared transients by van-der-Waals contacted sub-10-µm GaSe detectors*, Optics Express **26**, 19059 (2018).

[Koe06] W. Koechner and M. Bass, *Solid-State Laser Engineering*, Springer Series in Optical Sciences, vol. 1, Springer New York, New York, 2006.

[Kor14] A. Kormányos, G. Burkard, M. Gmitra, J. Fabian, V. Zólyomi, N. D. Drummond, and V. Fal'ko, *k.p theory for two-dimensional transition metal dichalcogenide semiconductors*, 2D Materials **2**, 049501 (2014).

[Kor15] A. Kormányos, G. Burkard, M. Gmitra, J. Fabian, V. Zólyomi, N. D. Drummond, and V. Fal'ko, *k.p theory for two-dimensional transition metal dichalcogenide semiconductors*, 2D Materials **2**, 049501 (2015).

[Köt20a] F. Köttig, D. Schade, J. R. Koehler, P. S. J. Russell, and F. Tani, *Efficient single-cycle pulse compression of an ytterbium fiber laser at 10 MHz repetition rate*, Optics Express **28**, 9099 (2020).

[Köt20b] F. Köttig, F. Tani, and P. S. Russell, *Modulational-instability-free pulse compression in anti-resonant hollow-core photonic crystal fiber*, Optics Letters **45**, 4044 (2020).

[Kre18] R. V. Krems, *Unit Conversion Factors*, Molecules in Electromagnetic Fields, John Wiley & Sons, Inc., Hoboken, USA, 2018, pp. 297–298.

[Krü11] M. Krüger, M. Schenk, and P. Hommelhoff, *Attosecond control of electrons emitted from a nanoscale metal tip*, Nature **475**, 78–81 (2011).

[Küb04] C. Kübler, R. Huber, S. Tübel, and A. Leitenstorfer, *Ultrabroadband detection of multi-terahertz field transients with GaSe electro-optic sensors: Approaching the near infrared*, Applied Physics Letters **85**, 3360–3362 (2004).

[Kuc11] A. Kuc, N. Zibouche, and T. Heine, *Influence of quantum confinement on the electronic structure of the transition metal sulfide TS_2*, Physical Review B **83**, 245213 (2011).

[Kum12] A. Kumar and P. K. Ahluwalia, *Electronic structure of transition metal dichalcogenides monolayers 1H-MX2 (M = Mo, W; X = S, Se, Te) from ab-initio theory: new direct band gap semiconductors*, The European Physical Journal B **85**, 186 (2012).

[Kun18] J. Kunstmann, F. Mooshammer, P. Nagler, A. Chaves, F. Stein, N. Paradiso, G. Plechinger, C. Strunk, C. Schüller, G. Seifert, D. R. Reichman,

and T. Korn, *Momentum-space indirect interlayer excitons in transition-metal dichalcogenide van der Waals heterostructures*, Nature Physics **14**, 801–805 (2018).

[Kus16] F. Kuschewski, H. G. Von Ribbeck, J. Döring, S. Winnerl, L. M. Eng, and S. C. Kehr, *Narrow-band near-field nanoscopy in the spectral range from 1.3 to 8.5 THz*, Applied Physics Letters **108**, 113102 (2016).

[Lah96] A. Lahrech, R. Bachelot, P. Gleyzes, and A. C. Boccara, *Infrared-reflection-mode near-field microscopy using an apertureless probe with a resolution of λ/600*, Optics Letters **21**, 1315 (1996).

[Lan16] F. Langer, M. Hohenleutner, C. P. Schmid, C. Poellmann, P. Nagler, T. Korn, C. Schüller, M. S. Sherwin, U. Huttner, J. T. Steiner, S. W. Koch, M. Kira, and R. Huber, *Lightwave-driven quasiparticle collisions on a subcycle timescale*, Nature **533**, 225–229 (2016).

[Lan18] F. Langer, C. P. Schmid, S. Schlauderer, M. Gmitra, J. Fabian, P. Nagler, C. Schüller, T. Korn, P. G. Hawkins, J. T. Steiner, U. Huttner, S. W. Koch, M. Kira, and R. Huber, *Lightwave valleytronics in a monolayer of tungsten diselenide*, Nature **557**, 76–80 (2018).

[Leb09] S. Lebègue and O. Eriksson, *Electronic structure of two-dimensional crystals from ab initio theory*, Physical Review B **79**, 115409 (2009).

[Lee14] C.-H. H. Lee, G.-H. H. Lee, A. M. van der Zande, W. Chen, Y. Li, M. Han, X. Cui, G. Arefe, C. Nuckolls, T. F. Heinz, J. Guo, J. Hone, and P. Kim, *Atomically thin p-n junctions with van der Waals heterointerfaces.*, Nature Nanotechnology **9**, 676–681 (2014).

[Leh85] H. J. Lehmeier, W. Leupacher, and A. Penzkofer, *Nonresonant third order hyperpolarizability of rare gases and N₂ determined by third harmonic generation*, Optics Communications **56**, 67–72 (1985).

[Ley12] D. Ley, D. Gerbig, and P. R. Schreiner, *Tunnelling control of chemical reactions - The organic chemist's perspective*, Organic and Biomolecular Chemistry **10**, 3781–3790 (2012).

[Li14] Y. Li, A. Chernikov, X. Zhang, A. Rigosi, H. M. Hill, A. M. van der Zande, D. A. Chenet, E.-M. Shih, J. Hone, and T. F. Heinz, *Measurement of the optical dielectric function of monolayer transition-metal dichalcogenides: MoS$_2$, MoSe$_2$, WS$_2$, and WSe$_2$*, Physical Review B **90**, 205422 (2014).

[Li17] J. I. A. Li, T. Taniguchi, K. Watanabe, J. Hone, and C. R. Dean, *Excitonic superfluid phase in double bilayer graphene*, Nature Physics **13**, 751–755 (2017).

[Li21] W. Li, X. Qian, and J. Li, *Phase transitions in 2D materials*, Nature Reviews Materials (2021).

[Lia19] W. Liao, Y. Huang, H. Wang, and H. Zhang, *Van der Waals heterostructures for optoelectronics: Progress and prospects*, Applied Materials Today **16**, 435–455 (2019).

[Liu13a] G.-B. Liu, W.-Y. Shan, Y. Yao, W. Yao, and D. Xiao, *Three-band tight-binding model for monolayers of group-VIB transition metal dichalcogenides*, Physical Review B **88**, 085433 (2013).

[Liu13b] M. K. Liu, M. Wagner, E. Abreu, S. Kittiwatanakul, A. McLeod, Z. Fei, M. Goldflam, S. Dai, M. M. Fogler, J. Lu, S. A. Wolf, R. D. Averitt, and D. N. Basov, *Anisotropic electronic state via spontaneous phase separation in strained vanadium dioxide films*, Physical Review Letters **111**, 096602 (2013).

[Liu19] Y. Liu, Y. Huang, and X. Duan, *Van der Waals integration before and beyond two-dimensional materials*, Nature **567**, 323–333 (2019).

[Lor20] E. Lorchat, L. E. P. López, C. Robert, D. Lagarde, G. Froehlicher, T. Taniguchi, K. Watanabe, X. Marie, and S. Berciaud, *Filtering the photoluminescence spectra of atomically thin semiconductors with graphene*, Nature Nanotechnology **15**, 283–288 (2020).

[Low17] T. Low, A. Chaves, J. D. Caldwell, A. Kumar, N. X. Fang, P. Avouris, T. F. Heinz, F. Guinea, L. Martin-Moreno, and F. Koppens, *Polaritons in layered two-dimensional materials*, Nature Materials **16**, 182–194 (2017).

[LS13] O. Lopez-Sanchez, D. Lembke, M. Kayci, A. Radenovic, and A. Kis, *Ultrasensitive photodetectors based on monolayer MoS$_2$*, Nature Nanotechnology **8**, 497–501 (2013).

[Lu19a] X. Lu, P. Stepanov, W. Yang, M. Xie, M. A. Aamir, I. Das, C. Urgell, K. Watanabe, T. Taniguchi, G. Zhang, A. Bachtold, A. H. MacDonald, and D. K. Efetov, *Superconductors, orbital magnets and correlated states in magic-angle bilayer graphene*, Nature **574**, 653–657 (2019).

[Lu19b] Y. H. Lu, J. M. Larson, A. Baskin, X. Zhao, P. D. Ashby, D. Prendergast, H. A. Bechtel, R. Kostecki, and M. Salmeron, *Infrared Nanospectroscopy at the Graphene-Electrolyte Interface*, Nano Letters **19**, 5388–5393 (2019).

[Ma16] Q. Ma, T. I. Andersen, N. L. Nair, N. M. Gabor, M. Massicotte, C. H. Lui, A. F. Young, W. Fang, K. Watanabe, T. Taniguchi, J. Kong, N. Gedik, F. H. L. Koppens, and P. Jarillo-Herrero, *Tuning ultrafast electron thermalization pathways in a van der Waals heterostructure*, Nature Physics, 1–14 (2016).

[Ma19] E. Y. Ma, B. Guzelturk, G. Li, L. Cao, Z.-X. Shen, A. M. Lindenberg, and T. F. Heinz, *Recording interfacial currents on the subnanometer length and femtosecond time scale by terahertz emission*, Science Advances **5**, eaau0073 (2019).

[Mak10] K. F. Mak, C. Lee, J. Hone, J. Shan, and T. F. Heinz, *Atomically thin MoS$_2$: A new direct-gap semiconductor*, Physical Review Letters **105**, 136805 (2010).

[Mak18] K. F. Mak, D. Xiao, and J. Shan, *Light-valley interactions in 2D semiconductors*, Nature Photonics **12**, 451–460 (2018).

[Mar18] A. Marais, B. Adams, A. K. Ringsmuth, M. Ferretti, J. M. Gruber, R. Hendrikx, M. Schuld, S. L. Smith, I. Sinayskiy, T. P. J. Krüger, F. Petruccione, and R. van Grondelle, *The future of quantum biology*, Journal of The Royal Society Interface **15**, 20180640 (2018).

[Mas16] M. Massicotte, P. Schmidt, F. Vialla, K. G. Schädler, A. Reserbat-Plantey, K. Watanabe, T. Taniguchi, K. J. Tielrooij, and F. H. L. Koppens, *Picosecond photoresponse in van der Waals heterostructures*, Nature Nanotechnology **11**, 42–46 (2016).

[Mas17] S. Mastel, M. B. Lundeberg, P. Alonso-González, Y. Gao, K. Watanabe, T. Taniguchi, J. Hone, F. H. L. Koppens, A. Y. Nikitin, and R. Hillenbrand, *Terahertz Nanofocusing with Cantilevered Terahertz-Resonant Antenna Tips*, Nano Letters **17**, 6526–6533 (2017).

[Mat73] L. F. Mattheiss, *Band Structures of Transition-Metal-Dichalcogenide Layer Compounds*, Physical Review B **8**, 3719–3740 (1973).

[McD14] S. McDonnell, R. Addou, C. Buie, R. M. Wallace, and C. L. Hinkle, *Defect-Dominated Doping and Contact Resistance in MoS_2*, ACS Nano **8**, 2880–2888 (2014).

[McG20] L. J. McGilly, A. Kerelsky, N. R. Finney, K. Shapovalov, E.-M. Shih, A. Ghiotto, Y. Zeng, S. L. Moore, W. Wu, Y. Bai, K. Watanabe, T. Taniguchi, M. Stengel, L. Zhou, J. Hone, X. Zhu, D. N. Basov, C. Dean, C. E. Dreyer, and A. N. Pasupathy, *Visualization of moiré superlattices*, Nature Nanotechnology **15**, 580–584 (2020).

[McL14] A. S. McLeod, P. Kelly, M. D. Goldflam, Z. Gainsforth, A. J. Westphal, G. Dominguez, M. H. Thiemens, M. M. Fogler, and D. N. Basov, *Model for quantitative tip-enhanced spectroscopy and the extraction of nanoscale-resolved optical constants*, Physical Review B **90**, 085136 (2014).

[McL17] A. S. McLeod, E. van Heumen, J. G. Ramirez, S. Wang, T. Saerbeck, S. Guenon, M. Goldflam, L. Anderegg, P. Kelly, A. Mueller, M. K. Liu, I. K. Schuller, and D. N. Basov, *Nanotextured phase coexistence in the correlated insulator V_2O_3*, Nature Physics **13**, 80–86 (2017).

[Mer19] P. Merkl, F. Mooshammer, P. Steinleitner, A. Girnghuber, K.-Q. Lin, P. Nagler, J. Holler, C. Schüller, J. M. Lupton, T. Korn, S. Ovesen, S. Brem, E. Malic, and R. Huber, *Ultrafast transition between exciton phases in van der Waals heterostructures*, Nature Materials **18**, 691–696 (2019).

[Mer20] P. Merkl, F. Mooshammer, S. Brem, A. Girnghuber, K. Q. Lin, L. Weigl, M. Liebich, C. K. Yong, R. Gillen, J. Maultzsch, J. M. Lupton, E. Malic, and R. Huber, *Twist-tailoring Coulomb correlations in van der Waals homobilayers*, Nature Communications **11**, 2167 (2020).

[Mer21] P. Merkl, C. K. Yong, M. Liebich, I. Hofmeister, G. Berghäuser, E. Malic, and R. Huber, *Proximity control of interlayer exciton-phonon hybridization in van der Waals heterostructures*, Nature Communications **12**, 1719 (2021).

[Mey18] F. Meyer, N. Hekmat, S. Mansourzadeh, F. Fobbe, F. Aslani, M. Hoffmann, and C. J. Saraceno, *Optical rectification of a 100 W average power mode-locked thin-disk oscillator*, Optics Letters **43**, 5909 (2018).

[Mey20] F. Meyer, T. Vogel, S. Ahmed, and C. J. Saraceno, *Single-cycle, MHz repetition rate THz source with 66 mW of average power*, Optics Letters **45**, 2494 (2020).

[Mit03] D. M. Mittleman, *Sensing with Terahertz Radiation*, Springer Series in Optical Sciences, vol. 85, Springer Berlin Heidelberg, Berlin, Heidelberg, 2003.

[Moo15] K. Moon, H. Park, J. Kim, Y. Do, S. Lee, G. Lee, H. Kang, and H. Han, *Subsurface nanoimaging by broadband terahertz pulse near-field microscopy*, Nano Letters **15**, 549–552 (2015).

[Moo16] G. Moody, J. Schaibley, and X. Xu, *Exciton Dynamics in Monolayer Transition Metal Dichalcogenides*, Journal of the Optical Society of America B **33**, C39 (2016).

[Moo18] F. Mooshammer, F. Sandner, M. A. Huber, M. Zizlsperger, H. Weigand, M. Plankl, C. Weyrich, M. Lanius, J. Kampmeier, G. Mussler, D. Grützmacher, J. L. Boland, T. L. Cocker, and R. Huber, *Nanoscale Near-Field Tomography of Surface States on $(Bi_{0.5}Sb_{0.5})_2Te_3$*, Nano Letters **18**, 7515–7523 (2018).

[Moo20] F. Mooshammer, M. A. Huber, F. Sandner, M. Plankl, M. Zizlsperger, and R. Huber, *Quantifying Nanoscale Electromagnetic Fields in Near-Field Microscopy by Fourier Demodulation Analysis*, ACS Photonics **7**, 344–351 (2020).

[Moo21] F. Mooshammer, M. Plankl, T. Siday, M. Zizlsperger, F. Sandner, R. Vitalone, R. Jing, M. A. Huber, D. N. Basov, and R. Huber, *Quantitative terahertz emission nanoscopy with multi-resonant near-field probes*, Accepted - Optics Letters (2021).

[MS13] A. Molina-Sánchez, D. Sangalli, K. Hummer, A. Marini, and L. Wirtz, *Effect of spin-orbit interaction on the optical spectra of single-layer, double-layer, and bulk MoS$_2$*, Physical Review B **88**, 045412 (2013).

[Mül04] D. Müller, A. Giesen, R. Paschotta, and U. Keller, *Ultrashort Pulse Thin-Disk Lasers and Amplifiers*, Femtosecond Technology for Technical and Medical Applications, Springer, Berlin, Heidelberg, sep 2004, pp. 55–73.

[Mül20] M. Müller, N. Martín Sabanés, T. Kampfrath, and M. Wolf, *Phase-Resolved Detection of Ultrabroadband THz Pulses inside a Scanning Tunneling Microscope Junction*, ACS Photonics **7**, 2046–2055 (2020).

[Nag17] P. Nagler, G. Plechinger, M. V. Ballottin, A. Mitioglu, S. Meier, N. Paradiso, C. Strunk, A. Chernikov, P. C. M. Christianen, C. Schüller, and T. Korn, *Interlayer exciton dynamics in a dichalcogenide monolayer heterostructure*, 2D Materials **4**, 025112 (2017).

[Nam76] S. B. Nam, D. C. Reynolds, C. W. Litton, R. J. Almassy, T. C. Collins, and C. M. Wolfe, *Free-exciton energy spectrum in GaAs*, Physical Review B **13**, 761–767 (1976).

[Nee18] A. Neef, *Simulating Ultrashort Light Pulses in STM Tunnel Junctions*, Master Thesis, 2018 (Available on private request via markus.plankl@ur.de).

[Neg11] J.-P. Negel, R. Hegenbarth, A. Steinmann, B. Metzger, F. Hoos, and H. Giessen, *Compact and cost-effective scheme for THz generation via op-*

tical rectification in GaP and GaAs using novel fs laser oscillators, Applied Physics B **103**, 45–50 (2011).

[Ngô14] C. Ngô and M. Van de Voorde, *Nanotechnology in a Nutshell*, Atlantis Press, Paris, 2014.

[Ni15] G. X. Ni, H. Wang, J. S. Wu, Z. Fei, M. D. Goldflam, F. Keilmann, B. Özyilmaz, A. H. Castro Neto, X. M. Xie, M. M. Fogler, and D. N. Basov, *Plasmons in graphene moiré superlattices*, Nature Materials **14**, 1217–1222 (2015).

[Nov04] K. S. Novoselov, *Electric Field Effect in Atomically Thin Carbon Films*, Science **306**, 666–669 (2004).

[Nov16] K. S. Novoselov, A. Mishchenko, A. Carvalho, and A. H. Castro Neto, *2D materials and van der Waals heterostructures*, Science **353**, aac9439 (2016).

[Oce04] N. Ocelic and R. Hillenbrand, *Subwavelength-scale tailoring of surface phonon polaritons by focused ion-beam implantation*, Nature Materials **3**, 606–609 (2004).

[Ols16] T. Olsen, S. Latini, F. Rasmussen, and K. S. Thygesen, *Simple Screened Hydrogen Model of Excitons in Two-Dimensional Materials*, Physical Review Letters **116**, 056401 (2016).

[Par18] K.-D. Park, T. Jiang, G. Clark, X. Xu, and M. B. Raschke, *Radiative control of dark excitons at room temperature by nano-optical antenna-tip Purcell effect*, Nature Nanotechnology **13**, 59–64 (2018).

[Pas09] R. Paschotta, *Encyclopedia of Laser Physics and Technology*, 1 ed., Wiley-VCH, Berlin, 2009.

[Pas13] A. Pashkin, A. Sell, T. Kampfrath, and R. Huber, *Electric and magnetic terahertz nonlinearities resolved on the sub-cycle scale*, New Journal of Physics **15**, 065003 (2013).

[Ped16] T. G. Pedersen, *Exciton Stark shift and electroabsorption in monolayer transition-metal dichalcogenides*, Physical Review B **94**, 1–6 (2016).

[Pel20] D. Peller, L. Z. Kastner, T. Buchner, C. Roelcke, F. Albrecht, N. Moll, R. Huber, and J. Repp, *Sub-cycle atomic-scale forces coherently control a single-molecule switch*, Nature **585**, 58–62 (2020).

[Pel21] D. Peller, C. Roelcke, L. Z. Kastner, T. Buchner, A. Neef, J. Hayes, F. Bonafé, D. Sidler, M. Ruggenthaler, A. Rubio, R. Huber, and J. Repp, *Quantitative sampling of atomic-scale electromagnetic waveforms*, Nature Photonics **15**, 143–147 (2021).

[Pen16] B. Peng, G. Yu, X. Liu, B. Liu, X. Liang, L. Bi, L. Deng, T. C. Sum, and K. P. Loh, *Ultrafast charge transfer in MoS_2/WSe_2 p-n Heterojunction*, 2D Materials **3**, 025020 (2016).

[Per96] J. P. Perdew, K. Burke, and M. Ernzerhof, *Generalized gradient approximation made simple*, Physical Review Letters **77**, 3865–3868 (1996).

[Pfi18] E. Pfitzner, X. Hu, H. W. Schumacher, A. Hoehl, D. Venkateshvaran, M. Cubukcu, J.-W. Liao, S. Auffret, J. Heberle, J. Wunderlich, and B. Kästner, *Near-field magneto-caloritronic nanoscopy on ferromagnetic nanostructures*, AIP Advances **8**, 125329 (2018).

[Phi14] S. P. Philipps and A. W. Bett, *CHAPTER 4. III-V Multi-junction Solar Cells*, Advanced Concepts in Photovoltaics, The Royal Society of Chemistry, 2014, pp. 87–117.

[Piz20] A. Pizzuto, D. M. Mittleman, and P. Klarskov, *Laser THz emission nanoscopy and THz nanoscopy*, Optics Express **28**, 18778 (2020).

[Pla21] M. Plankl, P. E. Faria Junior, F. Mooshammer, T. Siday, M. Zizlsperger, F. Sandner, F. Schiegl, S. Maier, M. A. Huber, M. Gmitra, J. Fabian, J. L. Boland, T. L. Cocker, and R. Huber, *Subcycle contact-free nanoscopy of ultrafast interlayer transport in atomically thin heterostructures*, Nature Photonics (2021).

[Ple16] G. Plechinger, P. Nagler, A. Arora, R. Schmidt, A. Chernikov, A. G. Del Águila, P. C. Christianen, R. Bratschitsch, C. Schüller, and T. Korn,

Trion fine structure and coupled spin-valley dynamics in monolayer tungsten disulfide, Nature Communications **7**, 1–9 (2016).

[Ple17] G. Plechinger, P. Nagler, A. Arora, R. Schmidt, A. Chernikov, J. Lupton, R. Bratschitsch, C. Schüller, and T. Korn, *Valley Dynamics of Excitons in Monolayer Dichalcogenides*, physica status solidi (RRL) - Rapid Research Letters **11**, 1700131 (2017).

[Poe15] C. Poellmann, P. Steinleitner, U. Leierseder, P. Nagler, G. Plechinger, M. Porer, R. Bratschitsch, C. Schüller, T. Korn, and R. Huber, *Resonant internal quantum transitions and femtosecond radiative decay of excitons in monolayer WSe_2*, Nature Materials **14**, 889–893 (2015).

[Poh84] D. W. Pohl, W. Denk, and M. Lanz, *Optical stethoscopy: Image recording with resolution $\lambda/20$*, Applied Physics Letters **44**, 651–653 (1984).

[Por03] J. A. Porto, P. Johansson, S. P. Apell, and T. López-Ríos, *Resonance shift effects in apertureless scanning near-field optical microscopy*, Physical Review B **67**, 085409 (2003).

[Pos18] K. W. Post, A. S. McLeod, M. Hepting, M. Bluschke, Y. Wang, G. Cristiani, G. Logvenov, A. Charnukha, G. X. Ni, P. Radhakrishnan, M. Minola, A. Pasupathy, A. V. Boris, E. Benckiser, K. A. Dahmen, E. W. Carlson, B. Keimer, and D. N. Basov, *Coexisting first- and second-order electronic phase transitions in a correlated oxide*, Nature Physics **14**, 1056–1061 (2018).

[Pro11] O. Pronin, J. Brons, C. Grasse, V. Pervak, G. Boehm, M.-C. Amann, V. L. Kalashnikov, A. Apolonski, and F. Krausz, *High-power 200 fs Kerr-lens mode-locked Yb:YAG thin-disk oscillator*, Optics Letters **36**, 4746 (2011).

[Pup15] I. Pupeza, D. Sanchez, J. Zhang, N. Lilienfein, M. Seidel, N. Karpowicz, T. Paasch-Colberg, I. Znakovskaya, M. Pescher, W. Schweinberger, V. Pervak, E. Fill, O. Pronin, Z. Wei, F. Krausz, A. Apolonski, and J. Biegert, *High-power sub-two-cycle mid-infrared pulses at 100 MHz repetition rate*, Nature Photonics **9**, 721–724 (2015).

[Qaz07] M. M. Qazilbash, M. Brehm, B.-G. Chae, P.-C. Ho, G. O. Andreev, B.-J. Kim, S. J. Yun, A. V. Balatsky, M. B. Maple, F. Keilmann, H.-T. Kim, and D. N. Basov, *Mott Transition in VO$_2$ Revealed by Infrared Spectroscopy and Nano-Imaging*, Science **318**, 1750–1753 (2007).

[Qin15] H. J. Qin, K. Zakeri, A. Ernst, L. M. Sandratskii, P. Buczek, A. Marmodoro, T. H. Chuang, Y. Zhang, and J. Kirschner, *Long-living terahertz magnons in ultrathin metallic ferromagnets*, Nature Communications **6**, 6126 (2015).

[Qiu13] D. Y. Qiu, F. H. Da Jornada, and S. G. Louie, *Optical spectrum of MoS$_2$: Many-body effects and diversity of exciton states*, Physical Review Letters **111**, 216805 (2013).

[Raj19] A. Raja, L. Waldecker, J. Zipfel, Y. Cho, S. Brem, J. D. Ziegler, M. Kulig, T. Taniguchi, K. Watanabe, E. Malic, T. F. Heinz, T. C. Berkelbach, and A. Chernikov, *Dielectric disorder in two-dimensional materials*, Nature Nanotechnology **14**, 832–837 (2019).

[Rak98] A. D. Rakić, A. B. Djurišić, J. M. Elazar, and M. L. Majewski, *Optical properties of metallic films for vertical-cavity optoelectronic devices*, Applied Optics **37**, 5271 (1998).

[Ram20] R. Ramos, D. Spierings, I. Racicot, and A. M. Steinberg, *Measurement of the time spent by a tunnelling atom within the barrier region*, Nature **583**, 529–532 (2020).

[Ras03] M. B. Raschke and C. Lienau, *Apertureless near-field optical microscopy: Tip-sample coupling in elastic light scattering*, Applied Physics Letters **83**, 5089–5091 (2003).

[Reg20] E. C. Regan, D. Wang, C. Jin, M. I. Bakti Utama, B. Gao, X. Wei, S. Zhao, W. Zhao, Z. Zhang, K. Yumigeta, M. Blei, J. D. Carlström, K. Watanabe, T. Taniguchi, S. Tongay, M. Crommie, A. Zettl, and F. Wang, *Mott and generalized Wigner crystal states in WSe$_2$/WS$_2$ moiré superlattices*, Nature **579**, 359–363 (2020).

[Riv15] P. Rivera, J. R. Schaibley, A. M. Jones, J. S. Ross, S. Wu, G. Aivazian, P. Klement, K. Seyler, G. Clark, N. J. Ghimire, J. Yan, D. G. Mandrus, W. Yao, and X. Xu, *Observation of long-lived interlayer excitons in monolayer MoSe₂-WSe₂ heterostructures*, Nature Communications **6**, 6242 (2015).

[Riv16] P. Rivera, K. L. Seyler, H. Yu, J. R. Schaibley, J. Yan, D. G. Mandrus, W. Yao, and X. Xu, *Valley-polarized exciton dynamics in a 2D semiconductor heterostructure*, Science **351**, 688–691 (2016).

[Roc18] J. G. Roch, N. Leisgang, G. Froehlicher, P. Makk, K. Watanabe, T. Taniguchi, C. Schönenberger, and R. J. Warburton, *Quantum-Confined Stark Effect in a MoS₂ Monolayer van der Waals Heterostructure*, Nano Letters **18**, 1070–1074 (2018).

[Rud18] A. M. Rudolf Gross, *Festkörperphysik*, de Gruyter, 2018.

[Rus03] P. Russell, *Photonic Crystal Fibers*, Science **299**, 358–362 (2003).

[Sal91] B. E. A. Saleh and M. C. Teich, *Fundamentals of Photonics*, Wiley Series in Pure and Applied Optics, John Wiley & Sons, Inc., New York, USA, 1991.

[Sal19] F. Saltarelli, I. J. Graumann, L. Lang, D. Bauer, C. R. Phillips, and U. Keller, *Power scaling of ultrafast oscillators: 350-W average-power sub-picosecond thin-disk laser*, Optics Express **27**, 31465 (2019).

[Sar12] C. J. Saraceno, F. Emaury, O. H. Heckl, C. R. E. Baer, M. Hoffmann, C. Schriber, M. Golling, T. Südmeyer, and U. Keller, *275 W average output power from a femtosecond thin disk oscillator operated in a vacuum environment*, Optics Express **20**, 23535 (2012).

[Sar19] C. J. Saraceno, D. Sutter, T. Metzger, and M. Abdou Ahmed, *The amazing progress of high-power ultrafast thin-disk lasers*, Journal of the European Optical Society-Rapid Publications **15**, 15 (2019).

[Sch92] E. Schrödinger and R. Penrose, *What is Life?*, Cambridge University Press, 1992.

[Sch05] S. C. Schneider, S. Grafström, and L. M. Eng, *Scattering near-field optical microscopy of optically anisotropic systems*, Physical Review B **71**, 115418 (2005).

[Sch14] O. Schubert, M. Hohenleutner, F. Langer, B. Urbanek, C. Lange, U. Huttner, D. Golde, T. Meier, M. Kira, S. W. Koch, and R. Huber, *Sub-cycle control of terahertz high-harmonic generation by dynamical Bloch oscillations*, Nature Photonics **8**, 119–123 (2014).

[Sch16a] J. R. Schaibley, H. Yu, G. Clark, P. Rivera, J. S. Ross, K. L. Seyler, W. Yao, and X. Xu, *Valleytronics in 2D materials*, Nature Reviews Materials **1**, 16055 (2016).

[Sch16b] B. Scharf, T. Frank, M. Gmitra, J. Fabian, I. Žutić, and V. Perebeinos, *Excitonic Stark effect in MoS_2 monolayers*, Physical Review B **94**, 245434 (2016).

[Sch17] P. R. Schreiner, *Tunneling Control of Chemical Reactions: The Third Reactivity Paradigm*, Journal of the American Chemical Society **139**, 15276–15283 (2017).

[Sch19] S. Schlauderer, C. Lange, S. Baierl, T. Ebnet, C. P. Schmid, D. C. Valovcin, A. K. Zvezdin, A. V. Kimel, R. V. Mikhaylovskiy, and R. Huber, *Temporal and spectral fingerprints of ultrafast all-coherent spin switching*, Nature **569**, 383–387 (2019).

[Sch21] C. P. Schmid, L. Weigl, P. Grössing, V. Junk, C. Gorini, S. Schlauderer, S. Ito, M. Meierhofer, N. Hofmann, D. Afanasiev, J. Crewse, K. A. Kokh, O. E. Tereshchenko, J. Güdde, F. Evers, J. Wilhelm, K. Richter, U. Höfer, and R. Huber, *Tunable non-integer high-harmonic generation in a topological insulator*, Nature **593**, 385–390 (2021).

[Sea13] A. Seabaugh, *The tunneling transistor*, IEEE Spectrum **50**, 35–62 (2013).

[Sei17] M. Seidel, J. Brons, G. Arisholm, K. Fritsch, V. Pervak, and O. Pronin, *Efficient High-Power Ultrashort Pulse Compression in Self-Defocusing Bulk Media*, Scientific Reports **7**, 1410 (2017).

[Sei18] M. Seidel, X. Xiao, S. A. Hussain, G. Arisholm, A. Hartung, K. T. Zawilski, P. G. Schunemann, F. Habel, M. Trubetskov, V. Pervak, O. Pronin, and F. Krausz, *Multi-watt, multi-octave, mid-infrared femtosecond source*, Science Advances **4**, eaaq1526 (2018).

[Sey19] K. L. Seyler, P. Rivera, H. Yu, N. P. Wilson, E. L. Ray, D. G. Mandrus, J. Yan, W. Yao, and X. Xu, *Signatures of moiré-trapped valley excitons in $MoSe_2/WSe_2$ heterobilayers*, Nature **567**, 66–70 (2019).

[Sha04] J. Shan and T. F. Heinz, *Terahertz Radiation from Semiconductors*, Scientist, vol. 16, Springer, Berlin, Heidelberg, jan 2004, pp. 1–56.

[Sho09] D. S. Sholl and J. A. Steckel, *Density Functional Theory: A Practical Introduction*, John Wiley & Sons, Inc., Hoboken, USA, 2009.

[Sid17] T. Siday, M. Natrella, J. Wu, H. Liu, and O. Mitrofanov, *Resonant terahertz probes for near-field scattering microscopy*, Optics Express **25**, 27874 (2017).

[Sid20] T. Siday, L. L. Hale, R. I. Hermans, and O. Mitrofanov, *Resonance-Enhanced Terahertz Nanoscopy Probes*, ACS Photonics **7**, 596–601 (2020).

[Son18] T. Song, X. Cai, M. W.-Y. Tu, X. Zhang, B. Huang, N. P. Wilson, K. L. Seyler, L. Zhu, T. Taniguchi, K. Watanabe, M. A. McGuire, D. H. Cobden, D. Xiao, W. Yao, and X. Xu, *Giant tunneling magnetoresistance in spin-filter van der Waals heterostructures*, Science **360**, 1214–1218 (2018).

[Spl10] A. Splendiani, L. Sun, Y. Zhang, T. Li, J. Kim, C.-Y. Chim, G. Galli, and F. Wang, *Emerging Photoluminescence in Monolayer MoS_2*, Nano Letters **10**, 1271–1275 (2010).

[Sta01] J. Stahn, U. Pietsch, P. Blaha, and K. Schwarz, *Electric-field-induced charge-density variations in covalently bonded binary compounds*, Physical Review B **63**, 165205 (2001).

[Ste03] L. Stebounova, B. B. Akhremitchev, and G. C. Walker, *Enhancement of the weak scattered signal in apertureless near-field scanning infrared microscopy*, Review of Scientific Instruments **74**, 3670–3674 (2003).

[Ste17a] A. Steinhoff, M. Florian, M. Rösner, G. Schönhoff, T. O. Wehling, and F. Jahnke, *Exciton fission in monolayer transition metal dichalcogenide semiconductors*, Nature Communications **8**, 1166 (2017).

[Ste17b] P. Steinleitner, P. Merkl, P. Nagler, J. Mornhinweg, C. Schüller, T. Korn, A. Chernikov, and R. Huber, *Direct Observation of Ultrafast Exciton Formation in a Monolayer of WSe$_2$*, Nano Letters **17**, 1455–1460 (2017).

[Ste18] P. Steinleitner, P. Merkl, A. Graf, P. Nagler, K. Watanabe, T. Taniguchi, J. Zipfel, C. Schüller, T. Korn, A. Chernikov, S. Brem, M. Selig, G. Berghäuser, E. Malic, and R. Huber, *Dielectric Engineering of Electronic Correlations in a van der Waals Heterostructure*, Nano Letters **18**, 1402–1409 (2018).

[Sti16] A. V. Stier, K. M. McCreary, B. T. Jonker, J. Kono, and S. A. Crooker, *Exciton diamagnetic shifts and valley Zeeman effects in monolayer WS$_2$ and MoS$_2$ to 65 Tesla*, Nature Communications **7**, 1–8 (2016).

[Sti18a] A. V. Stier, N. P. Wilson, K. A. Velizhanin, J. Kono, X. Xu, and S. A. Crooker, *Magnetooptics of Exciton Rydberg States in a Monolayer Semiconductor*, Physical Review Letters **120**, 057405 (2018).

[Sti18b] H. T. Stinson, A. Sternbach, O. Najera, R. Jing, A. S. Mcleod, T. V. Slusar, A. Mueller, L. Anderegg, H. T. Kim, M. Rozenberg, and D. N. Basov, *Imaging the nanoscale phase separation in vanadium dioxide thin films at terahertz frequencies*, Nature Communications **9**, 3604 (2018).

[Str39] J. A. Stratton and L. J. Chu, *Diffraction Theory of Electromagnetic Waves*, Physical Review **56**, 99–107 (1939).

[Su08] J. J. Su and A. H. MacDonald, *How to make a bilayer exciton condensate flow*, Nature Physics **4**, 799–802 (2008).

[Süd08] T. Südmeyer, S. V. Marchese, S. Hashimoto, C. R. E. Baer, G. Gingras, B. Witzel, and U. Keller, *Femtosecond laser oscillators for high-field science*, Nature Photonics **2**, 599–604 (2008).

[Sun18] S. S. Sunku, G. X. Ni, B. Y. Jiang, H. Yoo, A. Sternbach, A. S. McLeod, T. Stauber, L. Xiong, T. Taniguchi, K. Watanabe, P. Kim, M. M. Fogler, and D. N. Basov, *Photonic crystals for nano-light in moiré graphene superlattices*, Science **362**, 1153–1156 (2018).

[Sun20] S. S. Sunku, A. S. McLeod, T. Stauber, H. Yoo, D. Halbertal, G. Ni, A. Sternbach, B. Y. Jiang, T. Taniguchi, K. Watanabe, P. Kim, M. M. Fogler, and D. N. Basov, *Nano-photocurrent Mapping of Local Electronic Structure in Twisted Bilayer Graphene*, Nano Letters **20**, 2958–2964 (2020).

[Syn28] E. Synge, *XXXVIII. A suggested method for extending microscopic resolution into the ultra-microscopic region*, The London, Edinburgh, and Dublin Philosophical Magazine and Journal of Science **6**, 356–362 (1928).

[Tal19] T. Taliercio and P. Biagioni, *Semiconductor infrared plasmonics*, Nanophotonics **8**, 949–990 (2019).

[Tan20] Y. Tang, L. Li, T. Li, Y. Xu, S. Liu, K. Barmak, K. Watanabe, T. Taniguchi, A. H. MacDonald, J. Shan, and K. F. Mak, *Simulation of Hubbard model physics in WSe_2/WS_2 moiré superlattices*, Nature **579**, 353–358 (2020).

[Ted19] D. Tedeschi, M. De Luca, P. E. Faria Junior, A. Granados Del Águila, Q. Gao, H. H. Tan, B. Scharf, P. C. Christianen, C. Jagadish, J. Fabian, and A. Polimeni, *Unusual spin properties of InP wurtzite nanowires revealed by Zeeman splitting spectroscopy*, Physical Review B **99**, 161204 (2019).

[Tha20] K. Thakar and S. Lodha, *Optoelectronic and photonic devices based on transition metal dichalcogenides*, Materials Research Express **7**, 014002 (2020).

[Tia20] T. Tian, D. Scullion, D. Hughes, L. H. Li, C. J. Shih, J. Coleman, M. Chhowalla, and E. J. Santos, *Electronic Polarizability as the Fundamental Variable in the Dielectric Properties of Two-Dimensional Materials*, Nano Letters **20**, 841–851 (2020).

[Tra19] K. Tran, G. Moody, F. Wu, X. Lu, J. Choi, K. Kim, A. Rai, D. A. Sanchez, J. Quan, A. Singh, J. Embley, A. Zepeda, M. Campbell, T. Autry,

T. Taniguchi, K. Watanabe, N. Lu, S. K. Banerjee, K. L. Silverman, S. Kim, E. Tutuc, L. Yang, A. H. MacDonald, and X. Li, *Evidence for moiré excitons in van der Waals heterostructures*, Nature **567**, 71–75 (2019).

[Tre97] R. Trebino, K. W. DeLong, D. N. Fittinghoff, J. N. Sweetser, M. A. Krumbügel, B. A. Richman, and D. J. Kane, *Measuring ultrashort laser pulses in the time-frequency domain using frequency-resolved optical gating*, Review of Scientific Instruments **68**, 3277–3295 (1997).

[Tru16] M. Trushin, M. O. Goerbig, and W. Belzig, *Optical absorption by Dirac excitons in single-layer transition-metal dichalcogenides*, Physical Review B **94**, 041301 (2016).

[Uge14] M. M. Ugeda, A. J. Bradley, S.-F. Shi, F. H. da Jornada, Y. Zhang, D. Y. Qiu, W. Ruan, S.-K. Mo, Z. Hussain, Z.-X. Shen, F. Wang, S. G. Louie, and M. F. Crommie, *Giant bandgap renormalization and excitonic effects in a monolayer transition metal dichalcogenide semiconductor*, Nature Materials **13**, 1091–1095 (2014).

[Uge16] M. M. Ugeda, A. J. Bradley, Y. Zhang, S. Onishi, Y. Chen, W. Ruan, C. Ojeda-Aristizabal, H. Ryu, M. T. Edmonds, H.-Z. Tsai, A. Riss, S.-K. Mo, D. Lee, A. Zettl, Z. Hussain, Z.-X. Shen, and M. F. Crommie, *Characterization of collective ground states in single-layer NbSe$_2$*, Nature Physics **12**, 92–97 (2016).

[Ulb11] R. Ulbricht, E. Hendry, J. Shan, T. F. Heinz, and M. Bonn, *Carrier dynamics in semiconductors studied with time-resolved terahertz spectroscopy*, Reviews of Modern Physics **83**, 543–586 (2011).

[Unu18] D. Unuchek, A. Ciarrocchi, A. Avsar, K. Watanabe, T. Taniguchi, and A. Kis, *Room-temperature electrical control of exciton flux in a van der Waals heterostructure*, Nature **560**, 340–344 (2018).

[vdV02] N. C. J. van der Valk and P. C. M. Planken, *Electro-optic detection of subwavelength terahertz spot sizes in the near field of a metal tip*, Applied Physics Letters **81**, 1558–1560 (2002).

[Ver19] I. Verzhbitskiy, D. Vella, K. Watanabe, T. Taniguchi, and G. Eda, *Suppressed Out-of-Plane Polarizability of Free Excitons in Monolayer WSe₂*, ACS Nano **13**, 3218–3224 (2019).

[Wag14] M. Wagner, Z. Fei, A. S. McLeod, A. S. Rodin, W. Bao, E. G. Iwinski, Z. Zhao, M. Goldflam, M. Liu, G. Dominguez, M. Thiemens, M. M. Fogler, A. H. Castro Neto, C. N. Lau, S. Amarie, F. Keilmann, and D. N. Basov, *Ultrafast and nanoscale plasmonic phenomena in exfoliated graphene revealed by infrared pump-probe nanoscopy*, Nano Letters **14**, 894–900 (2014).

[Wan37] G. H. Wannier, *The Structure of Electronic Excitation Levels in Insulating Crystals*, Physical Review **52**, 191–197 (1937).

[Wan04] K. Wang, D. M. Mittleman, N. C. J. van der Valk, and P. C. M. Planken, *Antenna effects in terahertz apertureless near-field optical microscopy*, Applied Physics Letters **85**, 2715–2717 (2004).

[Wan06] F. Wang, J. Shan, M. A. Islam, I. P. Herman, M. Bonn, and T. F. Heinz, *Exciton polarizability in semiconductor nanocrystals*, Nature Materials **5**, 861–864 (2006).

[Wan17] H. Wang, X. Huang, J. Lin, J. Cui, Y. Chen, C. Zhu, F. Liu, Q. Zeng, J. Zhou, P. Yu, X. Wang, H. He, S. H. Tsang, W. Gao, K. Suenaga, F. Ma, C. Yang, L. Lu, T. Yu, E. H. T. Teo, G. Liu, and Z. Liu, *High-quality monolayer superconductor NbSe₂ grown by chemical vapour deposition*, Nature Communications **8**, 394 (2017).

[Wan18] G. Wang, A. Chernikov, M. M. Glazov, T. F. Heinz, X. Marie, T. Amand, and B. Urbaszek, *Colloquium : Excitons in atomically thin transition metal dichalcogenides*, Reviews of Modern Physics **90**, 021001 (2018).

[Wan19] X. Wang, P. Yu, Z. Lei, C. Zhu, X. Cao, F. Liu, L. You, Q. Zeng, Y. Deng, C. Zhu, J. Zhou, Q. Fu, J. Wang, Y. Huang, and Z. Liu, *Van der Waals negative capacitance transistors*, Nature Communications **10**, 3037 (2019).

[Wan21] Z. Wang, P. Altmann, C. Gadermaier, Y. Yang, W. Li, L. Ghirardini, C. Trovatello, M. Finazzi, L. Duò, M. Celebrano, R. Long, D. Akinwande,

O. V. Prezhdo, G. Cerullo, and S. Dal Conte, *Phonon-Mediated Interlayer Charge Separation and Recombination in a $MoSe_2/WSe_2$ Heterostructure*, Nano Letters **21**, 2165–2173 (2021).

[Wil69] J. Wilson and A. Yoffe, *The transition metal dichalcogenides discussion and interpretation of the observed optical, electrical and structural properties*, Advances in Physics **18**, 193–335 (1969).

[Woź20] T. Woźniak, P. E. Faria Junior, G. Seifert, A. Chaves, and J. Kunstmann, *Exciton g factors of van der Waals heterostructures from first-principles calculations*, Physical Review B **101**, 235408 (2020).

[Wun17] J. Wunderlich, *Spintronics: Current-switched magnetic insulator*, Nature Materials **16**, 284–285 (2017).

[Wur17] U. Wurstbauer, B. Miller, E. Parzinger, and A. W. Holleitner, *Light-matter interaction in transition metal dichalcogenides and their heterostructures*, Journal of Physics D: Applied Physics **50**, 173001 (2017).

[Xia12] D. Xiao, G. B. Liu, W. Feng, X. Xu, and W. Yao, *Coupled spin and valley physics in monolayers of MoS_2 and other group-VI dichalcogenides*, Physical Review Letters **108**, 196802 (2012).

[Xia14] F. Xia, H. Wang, D. Xiao, M. Dubey, and A. Ramasubramaniam, *Two-dimensional material nanophotonics*, Nature Photonics **8**, 899–907 (2014).

[Xu14] X. Xu, W. Yao, D. Xiao, and T. F. Heinz, *Spin and pseudospins in layered transition metal dichalcogenides*, Nature Physics **10**, 343–350 (2014).

[Xu18] J. Xu, B. Globisch, C. Hofer, N. Lilienfein, T. Butler, N. Karpowicz, and I. Pupeza, *Three-octave terahertz pulses from optical rectification of 20 fs, 1 μm, 78 MHz pulses in GaP*, Journal of Physics B: Atomic, Molecular and Optical Physics **51**, 154002 (2018).

[Yan91] X. L. Yang, S. H. Guo, F. T. Chan, K. W. Wong, and W. Y. Ching, *Analytic solution of a two-dimensional hydrogen atom. I. Nonrelativistic theory*, Physical Review A **43**, 1186–1196 (1991).

[Yao19] Z. Yao, V. Semenenko, J. Zhang, S. Mills, X. Zhao, X. Chen, H. Hu, R. Mescall, T. Ciavatti, S. March, S. R. Bank, T. H. Tao, X. Zhang, V. Perebeinos, Q. Dai, X. Du, and M. Liu, *Photo-induced terahertz near-field dynamics of graphene/InAs heterostructures*, Optics Express **27**, 13611 (2019).

[Ye14] Z. Ye, T. Cao, K. O'Brien, H. Zhu, X. Yin, Y. Wang, S. G. Louie, and X. Zhang, *Probing excitonic dark states in single-layer tungsten disulphide*, Nature **513**, 214–218 (2014).

[Yos16] K. Yoshioka, I. Katayama, Y. Minami, M. Kitajima, S. Yoshida, H. Shigekawa, and J. Takeda, *Real-space coherent manipulation of electrons in a single tunnel junction by single-cycle terahertz electric fields*, Nature Photonics **10**, 762–765 (2016).

[Yos18] K. Yoshioka, I. Katayama, Y. Arashida, A. Ban, Y. Kawada, K. Konishi, H. Takahashi, and J. Takeda, *Tailoring Single-Cycle Near Field in a Tunnel Junction with Carrier-Envelope Phase-Controlled Terahertz Electric Fields*, Nano Letters **18**, 5198–5204 (2018).

[Yos19] S. Yoshida, H. Hirori, T. Tachizaki, K. Yoshioka, Y. Arashida, Z. H. Wang, Y. Sanari, O. Takeuchi, Y. Kanemitsu, and H. Shigekawa, *Subcycle Transient Scanning Tunneling Spectroscopy with Visualization of Enhanced Terahertz Near Field*, ACS Photonics **6**, 1356–1364 (2019).

[Yu13] W. J. Yu, Z. Li, H. Zhou, Y. Chen, Y. Wang, Y. Huang, and X. Duan, *Vertically stacked multi-heterostructures of layered materials for logic transistors and complementary inverters*, Nature Materials **12**, 246–252 (2013).

[Yu15] Y. Yu, S. Hu, L. Su, L. Huang, Y. Liu, Z. Jin, A. A. Purezky, D. B. Geohegan, K. W. Kim, Y. Zhang, and L. Cao, *Equally efficient interlayer exciton relaxation and improved absorption in epitaxial and nonepitaxial MoS_2/WS_2 Heterostructures*, Nano Letters **15**, 486–491 (2015).

[Yua20] L. Yuan, B. Zheng, J. Kunstmann, T. Brumme, A. B. Kuc, C. Ma, S. Deng, D. Blach, A. Pan, and L. Huang, *Twist-angle-dependent interlayer exci-*

ton diffusion in WS$_2$-WSe$_2$ heterobilayers, Nature Materials **19**, 617–623 (2020).

[Zen95] F. Zenhausern, Y. Martin, and H. K. Wickramasinghe, *Scanning Interferometric Apertureless Microscopy: Optical Imaging at 10 Angstrom Resolution*, Science **269**, 1083–1085 (1995).

[Zha12] L. M. Zhang, G. O. Andreev, Z. Fei, A. S. McLeod, G. Dominguez, M. Thiemens, A. H. Castro-Neto, D. N. Basov, and M. M. Fogler, *Near-field spectroscopy of silicon dioxide thin films*, Physical Review B **85**, 075419 (2012).

[Zha13] W. Zhao, Z. Ghorannevis, L. Chu, M. Toh, C. Kloc, P.-H. Tan, and G. Eda, *Evolution of Electronic Structure in Atomically Thin Sheets of WS$_2$ and WSe$_2$*, ACS Nano **7**, 791–797 (2013).

[Zha16] C. Zhang, C. Gong, Y. Nie, K.-A. Min, C. Liang, Y. J. Oh, H. Zhang, W. Wang, S. Hong, L. Colombo, R. M. Wallace, and K. Cho, *Systematic study of electronic structure and band alignment of monolayer transition metal dichalcogenides in Van der Waals heterostructures*, 2D Materials **4**, 015026 (2016).

[Zha18a] J. Zhang, X. Chen, S. Mills, T. Ciavatti, Z. Yao, R. Mescall, H. Hu, V. Semenenko, Z. Fei, H. Li, V. Perebeinos, H. Tao, Q. Dai, X. Du, and M. Liu, *Terahertz Nanoimaging of Graphene*, ACS Photonics **5**, 2645–2651 (2018).

[Zha18b] J. Zhang, K. Fai Mak, N. Nagl, M. Seidel, D. Bauer, D. Sutter, V. Pervak, F. Krausz, and O. Pronin, *Multi-mW, few-cycle mid-infrared continuum spanning from 500 to 2250 cm^{-1}*, Light: Science and Applications **7**, 17180 (2018).

[Zhe21] S. Zheng, M. Zhao, L. Sun, and H. Yang, *Classical and quantum phases in hexagonal boron nitride-combined van der Waals heterostructures*, InfoMat **3**, 252–270 (2021).

[Zim21] J. E. Zimmermann, M. Axt, F. Mooshammer, P. Nagler, C. Schüller, T. Korn, U. Höfer, and G. Mette, *Ultrafast charge-transfer dynamics in twisted MoS$_2$/WSe$_2$ heterostructures*, arXiv (2021).

[Zol19a] K. Zollner, P. E. Faria Junior, and J. Fabian, *Proximity exchange effects in MoSe$_2$ and WSe$_2$ heterostructures with CrI$_3$: Twist angle, layer, and gate dependence*, Physical Review B **100**, 085128 (2019).

[Zol19b] K. Zollner, P. E. Junior, and J. Fabian, *Strain-tunable orbital, spin-orbit, and optical properties of monolayer transition-metal dichalcogenides*, Physical Review B **100**, 195126 (2019).

[Zol20] K. Zollner, P. E. Faria Junior, and J. Fabian, *Giant proximity exchange and valley splitting in transition metal dichalcogenide/hBN/(Co, Ni) heterostructures*, Physical Review B **101**, 085112 (2020).

[Žut04] I. Žutić, J. Fabian, and S. Das Sarma, *Spintronics: Fundamentals and applications*, Reviews of Modern Physics **76**, 323–410 (2004).

Acknowledgments

The last years were shaped by many friends and colleagues making our research journey and this thesis possible. In the following, I want to express my gratitude towards all the people that made my PhD so enjoyable and productive:

- **Prof. Dr. Rupert Huber** for entrusting me with this fascinating project and offering his help and insights anytime along the way. Thank you for your infectious scientific enthusiasm, careful supervision and curiosity in the lab or when discussing results allowing us to overcome any challenge during this journey. I am grateful for such an excited mentor not only teaching me professional scientific skills and concepts, but also providing valuable advice in challenging times.

- **Prof. Dr. Tyler Cocker** for the valuable lessons and explanations at the start of this project and collaborative learning how to handle high-power laser systems. Thank you for cheerful supervision, great advice and friendship as well as the shared beers and more or less intended fires over the years. I am especially grateful for the ongoing help and support even after leaving Regensburg making a great publication and this work possible.

- **Prof. Dr. Jaroslav Fabian** for the great collaboration and fruitful discussions on polarizability of van der Waals heterostructures and being part of the Board of examiners.

- **Prof. Dr. Jörg Wunderlich** for taking the time to asses this thesis and being part of the oral examination.

- **Prof. Dr. Christian Schüller** for being part of the Board of examiners.

- **Dr. Markus A. Huber** for his long-time friendship, scientific explanations and discussions as well as the enjoyable lab time, helpful advice and the Friday-night burgers. Thank you for your cheerful mood, careful supervision since my Bachelor thesis and many helpful insights when proofreading this thesis.

- **Martin Zizlsperger** for his large efforts and support during the experiments and his sharp mind, quickly learning and wrapping his head around novel concepts making him the ideal Master student and a big asset to the near-field team. It is great to see such development from a physics student to a full-fledged scientist within just a few years. Thank you for proofreading this thesis and the many hours we shared with beers or climbing.

- **Dr. Fabian Mooshammer** for the great discussions and help especially during the last part of my thesis and the publication process of the paper. I am grateful for your sheer infinite knowledge about two-dimensional materials as well as the moral support during challenging times.

- **Dr. Tom Siday** for his incredible efforts in the lab and during the publication process of the paper, plenty of advice from the perspective of a more experienced scientist and countless, some fruitful and some fun, discussions about physics and many other topics.

- **Dr. Paulo Faria Junior** for the great collaboration and efforts trying to understand each other and the physics we observed. Thank you for the many scientific discussions, but also for the friendship and moments we shared in our free time.

- **Felix Schiegl** for his cheerful mood and quick wit, which allowed him to be a great help already during his Bachelors. Thank you for your efforts at work and the moments we shared in our free time during climbing and group events. I am especially grateful for proofreading this thesis and taking the brunt of my creative usage of commas in the English language.

- **Fabian Sandner** for brightening up the mood with his perfectly organized group events and in his role as coffee warden, always keeping everybody hydrated at work and during other events. He is the prime example for making our group more than mere colleagues working together and always has an open ear or helping hand to spare.

- **Dr. Jessica L. Boland** for her support and help at the beginning of the THz nanoscopy project.

- **Prof. Dr. Philip Russel, Dr. Francesco Tani, Dr. Felix Köttig** and **Daniel Schade** for setting up custom-tailord HCPCFs in our laboratory making the high-power mid-infrared generation possible. I am especially thankful for Dr. Francesco Tani being available to help at short notice even on Friday evenings.

- **Professor Dr. Oleg Pronin, Dr. Marcus Seidel** and **Dr. Jonathan Brons** for setting up the laser system and broadening stage as well as for all the explanations and help along the way.

- **Ulla Franzke** for being the good heart of the group, despite the everyday challenges always having our back leading us through the jungle of bureaucracy and giving encouraging words when needed.

- **Imke Gronwald, Martin Furthmeier** and **Ignaz Laepple** for the excellent technical support every research group should be envious about. Thank you especially for your patience when we approached you with merely rough ideas, which you transformed into a working sample, mechanical part or electronic device within record time.

- **Simon Maier**, **Carmen Roelcke**, **Dr. Dmytro Afanasiev**, **Christian Meineke** and **Dr. Dominik Peller** for the shared time off work and weekly rock climbing sessions providing a well-deserved distraction and often enjoyable involuntary discussions about physics.

- The whole **Huber Group** for making the university not only a work place, but a supportive environment with friends tackling our individual challenges, but being able to count on each other for any help necessary. Thank you for all the support, experiences and group events bringing us closer together and making the last years so enjoyable.

- **My family**, since without them, my journey in physics and this work would not have been possible.

- **Magdalena** for being there for me – always.